INTELLIGENT CONTROL OF MIXED-CULTURE BIOPROCESSES

D. L. Stoner, E. D. Larsen, K. S. Miller, G. F. Andrews, and J. A. Johnson

Idaho National Engineering Laboratory
Lockheed Idaho Technologies Company, Inc.
P. O. Box 1625, Idaho Falls, ID 83415-2203

ABSTRACT

A hierarchical control system is being developed and applied to a mixed culture bioprocess in a continuous stirred tank reactor. A bioreactor, with its inherent complexity and non-linear behavior was an interesting, yet, difficult application for control theory. The bottom level of the hierarchy was implemented as a number of integrated set point controls and data acquisition modules. Within the second level was a diagnostic system that used expert knowledge to determine the operational status of the sensors, actuators, and control modules. A diagnostic program was successfully implemented for the detection of stirrer malfunctions, and to monitor liquid delivery rates and recalibrate the pumps when deviations from desired flow rates occurred. The highest control level was a supervisory shell that was developed using expert knowledge and the history of the reactor operation to determine the set points required to meet a set of production criteria. At this stage the supervisory shell analyzed the data to determine the state of the system. In future implementations, this shell will determine the set points required to optimize a cost function using expert knowledge and adaptive learning techniques.

INTRODUCTION

Bioprocesses which utilize axenic cultures and sterile feeds predominate in the food, pharmaceutical and specialty chemical industries. However, large scale bioprocessing for the mining industry or waste water treatment utilize mixed populations of microorganisms for two main reasons. First, and most important, is that mixed populations of indigenous microorganisms are more effective and can ever improve the performance through natural selection. Not only do these naturally occurring microorganisms behave as consortia, bacteria which have been added to enhance

activity may not be maintained within the indigenous microbial population. Difficulties and the expense involved with the sterilization of feed stocks required for large scale processing is a second reason that large scale processes must accommodate the presence of mixed microbial populations.

Control of any biologically-based process is complicated by the fact that microbial activity can not be directly manipulated. Microbial activity can be indirectly influenced through the manipulation of the physical and chemical environment. Furthermore, while the microorganisms are controlled by their environment, the microbial culture's environment is being changed by the metabolic activities of the microorganisms. Mixed culture bioprocesses further compound control issues by the additional requirement that the process must be regulated in such a manner as to maintain the desired activities of all consortium members that are necessary for the process. Another important consideration is that the main process variable, the microbial activity, can not be measured on-line in a commercially reliable fashion.

An intelligent control system for mixed culture bioprocesses using acidophilic microorganisms is of increasing importance to the mining industry. The long-term objective is a control strategy that will optimize economics of bioprocess. To this end, a hierarchical control system is being developed and applied to a nonlinear, unstable, mixed culture bioprocess in a continuous stirred tank reactor (CSTR).[1] At the bottom of the hierarchy was a number of integrated set point controls and data acquisition modules. The next level was a diagnostic system that used expert knowledge to determine the operational status of the various sensors, actuators, and control modules. The top level was a supervisory shell that is currently under development. This stage was capable of identifying the bioreactor state by reading information from the low level sensors, control systems, and the diagnostic system. In its envisioned, full, implementation, the supervisory shell will control the operation of the reactor by using expert knowledge and the history of the reactor operation to determine the set points required to meet a set of production criteria. In this paper, we describe the microorganism, the integration of the diagnostic system and the results obtained to date as they will be implemented into the top level supervisory shell.

SYSTEM DESCRIPTION

Microbial Culture

The mixed culture bioprocess used as the model system for this program is one that would be utilized for the microbial desulfurization of coal. *Thiobacillus ferrooxidans*, the causative agent of acid mine drainage, is a valuable microorganism for the bacterial leaching of sulfide mineral ores and the oxidation of pyritic sulfur in coal. *T. ferrooxidans* is a microorganism that inhabits acidic environments, utilizes CO_2 as a carbon source and Fe^{2+} as the energy source. In our test system, this microorganism was defined as the biocatalyst with CO_2 and Fe^{2+} as substrates. Fe^{3+} and metabolic products were the product and byproduct, respectively. In natural environments, acidophilic heterotrophic microorganisms enhance the desulfurization activity of *T. ferrooxidans* by scavenging the metabolites and other inhibitory organic compounds. Thus, in later stages of the program, an acidophilic heterotrophic microorganism will be added that will utilize, as its growth and energy source, the metabolic products excreted by *T. ferrooxidans*.

T. ferrooxidans (ATCC 23270) was cultivated at 30°C using a modification of the basal salts medium of Johnson et al.[2] The medium (pH 1.8), contained per liter $(NH_4)_2SO_4$, 1.25 g; $MgSO_4 \cdot 7H_2O$, 0.50 g; K_2HPO_4, 0.25 g; trace elements solution, 1 mL and 50 mM $FeSO_4$.

Hardware

The bioreactor was a 2 liter continuous culture system (Multigen F-2000, New Brunswick Scientific Co., Inc.) that was modified to receive external control signals for stirrer speed and heating. A stainless steel lid was constructed and fitted with 4 liquid inlet ports; sampling port; thermocouple; heating probe; sensors for oxygen, pH and redox (Ingold Electrodes, Inc., Wilmington, MA); air exhaust through a demister/condensation column; and an impeller and aeration assembly. Air and CO_2 were humidified by sparging through sterile water. Five peristaltic pumps (Masterflex 7520-35; Cole-Parmer Instrument Co., Niles, IL) were used feed water, basal salts, iron solution, acid and base into the bioreactor. Passive over flow was used to maintain the working volume of the reactor. Each of the three main pumps, i.e., water, nutrients and iron, had a fuzzy logic control loop to maintain the desired flow rates.

A Macintosh IIx computer equipped with a NB-MIO-16HX multifunction Input/Output board and two NB-AO6 analog output boards (National Instruments, Austin TX). These boards provided a total capacity of 16 analog input, 14 analog output, and 32 digital I/O lines for the bioreactor system. The I/O lines were isolated and conditioned with 5B series back plane and isolation modules. Additionally, the Macintosh was equipped with a 4 port serial board. Combined with the computer's 2 ports, this provided six RS-422 serial lines. The RS-422 ports were wired with custom made cables that made them compatible with the RS-232 instruments used in the system. The pump subsystem of the bioreactor used 1 analog input, 5 analog outputs, and 4 serial lines. The computer and all of the instruments in the system were protected with a Fortress uninterruptable power supply (Best Power Technology, Inc., Nedcedah, WI). Computer programming, data acquisition and analysis was done using LabVIEW graphical programming language (National Instruments Corporation, Austin, TX). LabVIEW provided a convenient operator interface, as well as a sophisticated language interface to the I/O boards for data acquisition and control.

Analytical Methods

Off-line titration of Fe^{2+} species with potassium dichromate[3] was used to determine the concentration of Fe (II). The concentration of Fe^{3+} in solution was determined offline by absorption at 304 nm.[4] On line measures for total organic carbon (TOC) were obtained by difference of total carbon and inorganic carbon using a total organic carbon analyzer (Model TOC-5000, Shimadzu Corporation, Columbia, MD). Dissolved organic carbon determinations were obtained by off-line measures of a filtered (0.2 μm, Whatman Puradisc, polypropylene filter, Clifton, NJ) reactor fluid. Cell counts were made by staining cells filtered onto black polycarbonate membrane filters (0.2 μm, Poretics, Livermore, CA) with acridine orange (0.01% final concentration in water adjusted to a pH of 11 with NaOH). Prior to staining cells were washed with water adjusted to pH 1 with sulfuric acid then with water adjusted to pH 11 with NaOH. After staining cells were washed with deionized water and counted using an epifluorescence microscope.

Low-Level Sensing and Control System

On-line sensors were used to determine the pH, temperature, dissolved oxygen, redox potential, and air and carbon dioxide flow rates (Figure 1). In addition a carbon analyzer was used on line to

determine total organic carbon, dissolved organic carbon, and dissolved carbon dioxide. The difference between the TOC and DOC was used a measure of biomass. Off-line measurements included cell counts and $[Fe^{+2}]$ and $[Fe^{+3}]$ as described below. Fuzzy PID[5] controllers were implemented to control the pH and temperature of the reactor. The pH was controlled by activating one of two pumps to add acid or base as necessary and the temperature maintained at the desired set point above the ambient room temperature by turning on or off a heater. The flow of air and carbon dioxide was controlled by mass flow controllers. Substrate feed concentrations were controlled by setting the flow rates of two pumps that transferred basal salts and iron solution from reservoirs into the reactor and the dilution rate controlled by adding water through a third pump. The reservoirs were placed on scales and the pumps recalibrated every 24 hours using the scale measurements. In addition, the effluent mass was measured as a check on the dilution rate. The system accounted for the addition of acid or base for pH control when determining the water flow such that the dilution rate remains constant.

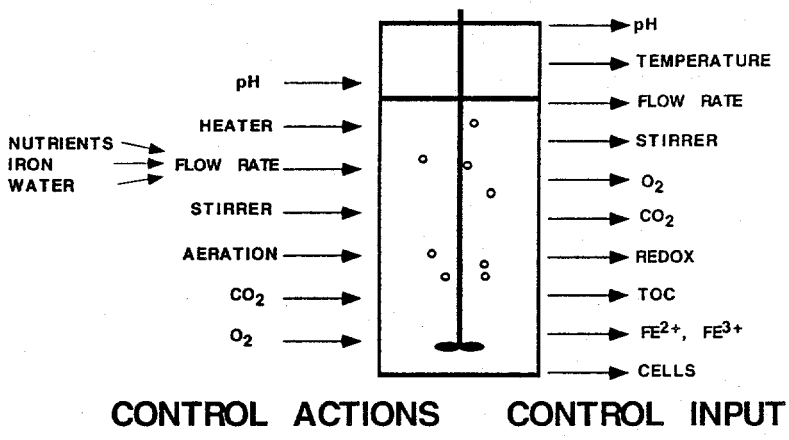

Figure 1. Schematic of reactor with control actions and control input variables obtained by on-line sensors and off-line analyses.

Diagnostic System

At the next level of control, a diagnostic system used expert knowledge to determine the operational status of the various sensors, actuators, and control modules. Sensed and controlled parameters were examined to be sure that the measured values were within the tolerance of the control system and, if not, the data was analyzed to determine the specific cause of the problem. Other problems were diagnosed indirectly from combinations of sensor data. For example, the increase in Redox and decrease in oxygen at 20 hours in Figure 2 was interpreted as a stopped stirrer by the diagnostics program. The importance of detection and diagnosis of instrument failures increases as run time increases. We have observed increased equipment malfunctions near the later stages of our extended bioreactor operations.

Supervisory Shell

The top level was a supervisory shell that is currently under development. At its current stage of development, the supervisory shell was capable of identifying the state of the bioreactor by reading information from the low level sensors and control systems and from the diagnostic system. In its envisioned implementation, the supervisory shell will be able to control the operation of the reactor by using expert knowledge and the history of the reactor operation to determine the set points required to meet a set of production criteria. This supervisor will observe the operation and make decisions to change the set points, adapting to the current status of the reactor and its inhabitants.

In this study, the supervisory shell monitored the acquired data to determine whether the bioreactor was in one of three operational states, 1) transition phase; 2) steady state or 3) washout. Transition phase is a transient state of the bioreactor that occurs when any operational parameter e.g., flow rates, substrate loading, or pH, has been changed. During the transition phase, as the reactor is approaching a new steady state, microbial activity is changing in response to the changes in the physical-chemical environment of the system. Steady state occurs when the microorganisms have achieved an approximate state of balanced growth in response to a steady environment. Once steady state has been achieved the human operator is prompted to modify operating parameters, i.e., flow rate if desired. While steady state can be defined in a variety of ways, our program defined steady state as a minimum of 5 reactor volumes, substrate (Fe^{2+}) and product (Fe^{3+}) concentrations that varied by less than 10% and biomass as determined by cell counts that varied by less than 25%. The latest installation of the program utilized TOC values that varied less than 10% instead of cell counts for the biomass measure. Washout condition is the operational state of the bioreactor in which the flow rate exceeds the maximum growth rate of the microorganisms and the cells are washed out of the reactor.

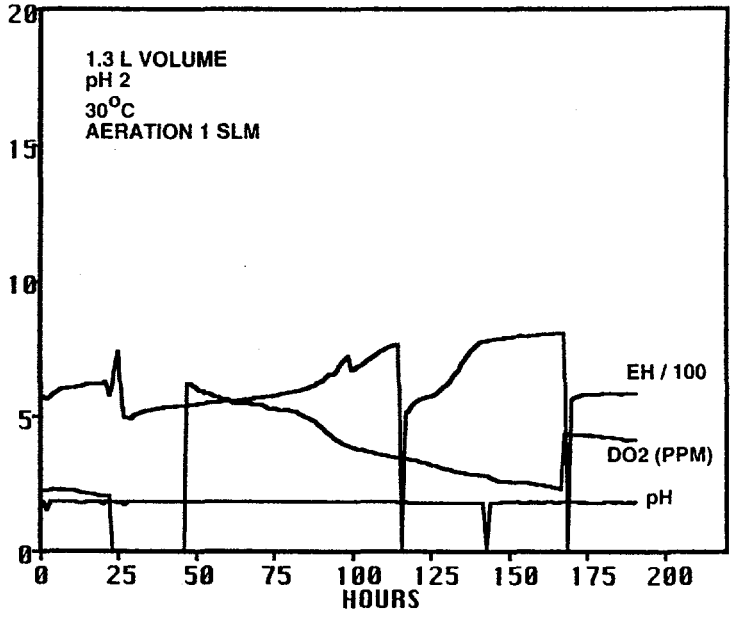

Figure 2. An example of the data set obtained by on-line Redox (mV), pH, and oxygen (ppm) determinations.

RESULTS AND DISCUSSION

We are developing and applying a hierarchical control system to a nonlinear mixed culture bioprocess in a CSTR. A CSTR bioreactor is inherently stable. However, we have introduced the dangers of instability by imposing an operating constraint that the volumetric productivity be a maximum. This requires that the bioreactor be operated near the washout point. To operate with an economic constraint also requires the minimum inputs of other nutrients. Data is reported here from a run of 47 days with a reactor volume of 1.3 L, air flow of 1 L/min, an iron feed concentration of 50 or 100 mM, and a range of dilution rates from $0.132\ hr^{-1} \leq D \leq 0.441\ hr^{-1}$ which corresponds to liquid delivery rates of 3 mls/min to 10 mls/min. The objectives were to test the lower-level control loops, to evaluate the ability of the diagnostic level to perform some simple tasks and to identify the limiting nutrient in order to start to construct rules by which the supervisory control system can move the system towards the optimal operating point.

Redox and oxygen probes were particularly subject to fouling problems, thus, were cleaned frequently. Differences in redox and oxygen values between fouled and cleaned probes was apparent from the data (Figure 2). Cell counts, and Fe^{2+} and Fe^{3+} concentrations were determined, at a

minimum, daily and entered into the data base (Figure 3). Excursions in TOC values occurred when the physical disturbance of the reactor resulted in the dislodging of solid material that had built up in dead zones in the reactor (Figure 3). While there was an increase in TOC during these excursions, there was little affect on the overall behavior of the reactor. In Figures 2 and 3, steady state was achieved at approximately 45 hours, and at 50 hours the flow rate was decreased from 10 mls/min to 6 mls/min. This corresponded to a decrease in dilution rate (D) from 0.441 hr^{-1} to 0.265 hr^{-1}. The decreased flow rate resulted in increased cell counts, and increased product (Fe^{3+}) concentration.

Redundant measures of process parameters will be used until the most effective and reliable means of assessing bioreactor performance are determined. While redox values provide an estimate the ratio of Fe(III) to Fe (II), they do not provide a measure of the concentration of the iron species. Total iron values obtained by the summation of values obtained for Fe (II) and Fe (III) by off-line quantitation agree with total iron concentrations obtained by atomic absorption spectroscopic methods (Data not shown). Fouling or coating of the redox probe and resulted in deviations from Redox potential of the bulk fluid. Graindorge et al.,[6] in relatively short bioreactor runs, utilized Redox measures as an estimate of biomass yield and biological activity. Because of errors introduced by fouling, Redox as a measure of microbial productivity could introduce error into our control decisions. Until a direct measure of microbial activity is developed in the context of this program, an indirect measure of activity will be biomass as measured by organic carbon measures and cell counting procedures. Initially, process monitoring and determination of steady state conditions was accomplished using cell counts as an estimate of microbial activity. With the addition of the total organic carbon (TOC) analyzer, on-line measures of organic carbon as an estimate of microbial growth and activity were used for the determination of steady state conditions.

The experimental plan that would determine the operational limits of the bioreactor was based on relationships for the kinetic behavior of a CSTR (Figure 4). Conventional treatment of kinetic data obtained from bioreactors assume that there is a single limiting nutrient in the liquid feed that, ultimately, controls the growth rate of the microorganisms. In our initial hypothesis, Fe^{2+} was the single limiting nutrient and that there would have been sufficient CO_2 introduced by aeration to support the growth of the microorganisms. The data from four steady-state conditions examined, plotted in Figure 5, show a pattern unlike that in Figure 4, indicating that microbial growth was not limited by Fe^{2+} or any other liquid-phase nutrient. Since dissolved oxygen was maintained at non-limiting values (4 -6 mg/L) throughout the experiment, the most likely hypothesis is that metabolism was limited by the availability of CO_2, the carbon source for the autotrophic *T. ferrooxidans*. Generally, on-line inorganic carbon values were less than 5

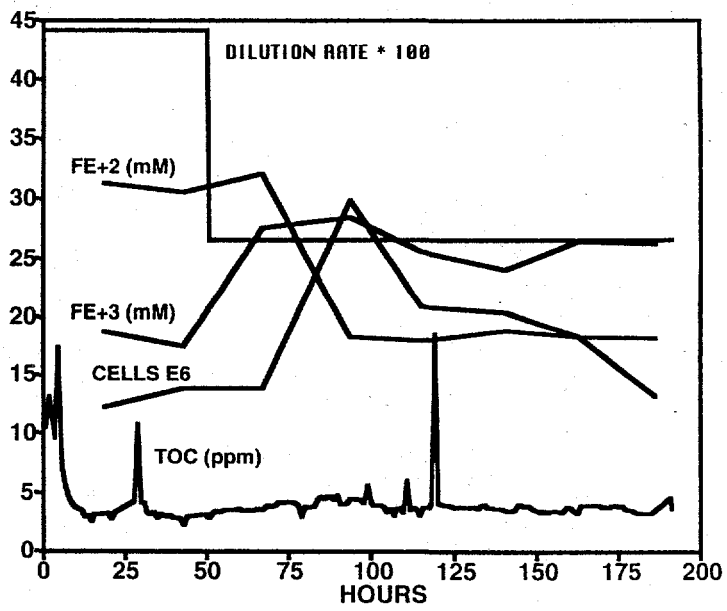

Figure 3. An example of the data set obtained for cell density (x E^6 cells/mL), Fe^{2+} concentration (mM), Fe^{3+} concentration (mM) and on-line total organic carbon determinations (ppm).

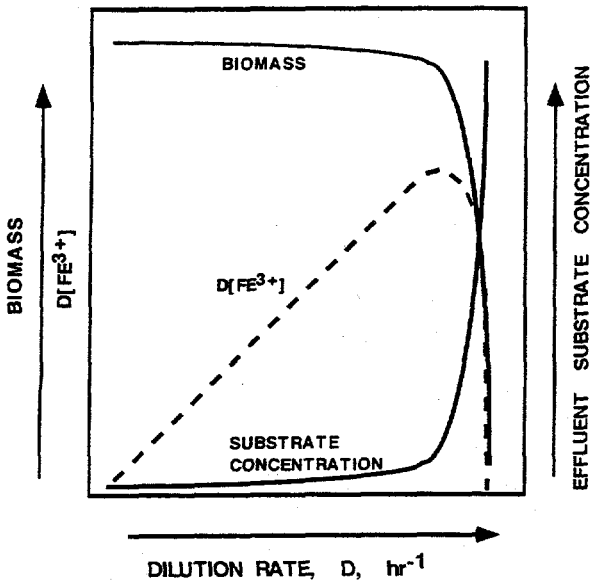

Figure 4. Expected relationships between dilution rate and cell yields, substrate concentration, or product concentration.

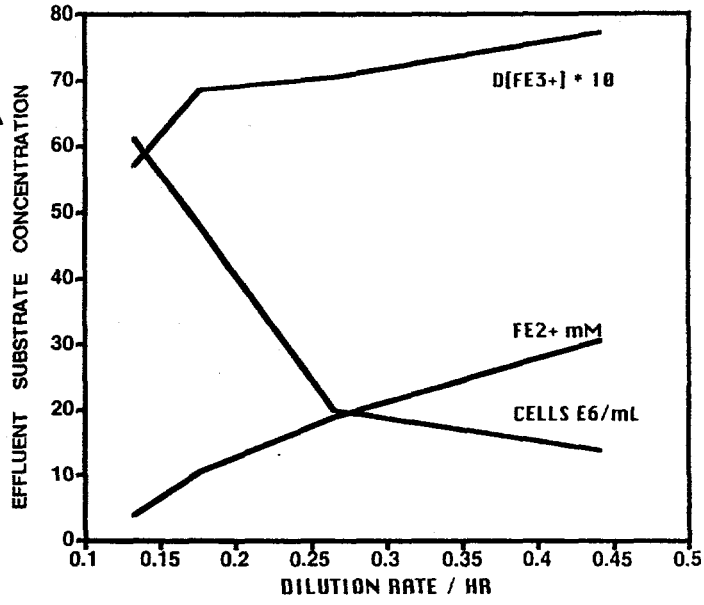

Figure 5. Experimentally determined relationships between dilution rate (Hr^{-1}), and effluent substrate concentration (mM), productivity (mM/Hr) and cell density (10^6 cells/mL).

ppb which suggested that the reactor was, indeed, operating under CO_2 limitation. Note that cell numbers did not rapidly approach zero as flow rate was increased (Figure 5). When the limiting nutrient must be transferred from the gas phase, cell washout did not occur was if would have if the limiting nutrient is dissolved in the liquid feed. Data obtained at steady state indicated that dilution rates greater than 0.176 (4 mL/min) resulted in marginal improvement in total Fe^{3+} yield (Figure 6). Maximum Fe^{3+} yield per unit biomass was observed for a dilution rate of 0.265 (6 mL/min). The observed CO_2 limitation at relatively low iron concentrations (~50 mM) has implications for the development of a control system that maximizes the iron oxidation rate. The feed must be enriched with CO_2 and controlled using on-line dissolved inorganic carbon measurements so as to maintain a reasonable non-limiting CO^2 concentration at reasonable cost.

SUMMARY

We have found that several lower-level control loops successfully performed control tasks such as pH and temperature control, accurate delivery of liquid feeds. Upper level control programs were successful in determining the operational state of the reactor and diagnosing equipment malfunctions. And working towards the goal of a supervisory control system, we have identified the limiting nutrient in order to start to construct rules by which this control system can move the system towards the optimal operating point. Problems such as analytical difficulties, equipment malfunctions and the complexity of the biological system which are typically encountered when running long term continuous processes must be accounted for and incorporated into any supervisory control program.

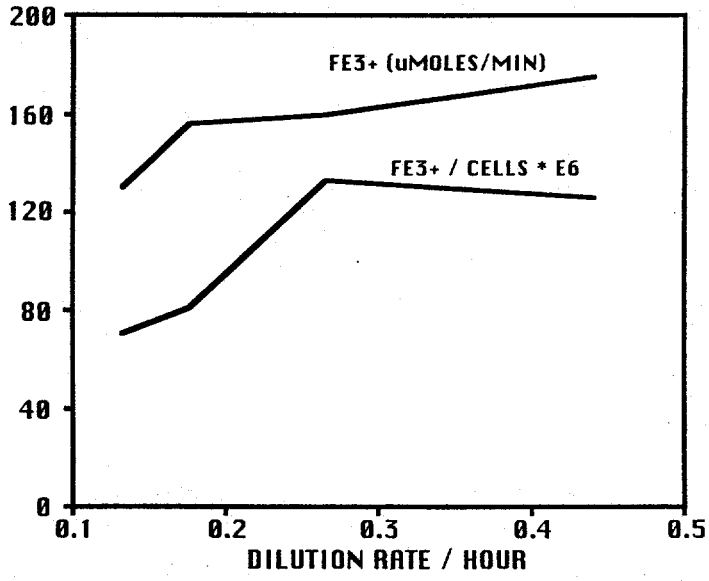

Figure 6. Relationship between total Fe^{3+} production (μmoles/min) and volumetric productivity (Fe^{3+}/cell numbers) and dilution rate.

ACKNOWLEDGMENTS

This work was supported by the U.S. Department of Energy, Office of Energy Research, Office of Basic Energy Sciences, under DOE Idaho Operations Office Contract No. DE-AC07-94ID13223.

REFERENCES

1. K. B. KONSTANTINOV and T. YOSHIDA, "Knowledge-Based Control of Fermentation Processes," *Biotechnol. Bioengineer.* 39, 479-486 (1992).

2. D. B. JOHNSON, J. H. M. MACVICAR, and S. WOLFE, "A New Solid Medium for the Isolation and Enumeration of *Thiobacillus Ferrooxidans* and Acidophilic Heterotrophic Bacteria," *J. Microbiol. Methods,* 7, 9-18 (1987).

3. D. A. SKOOG and D. M. WEST, *Fundamentals of Analytical Chemistry*, Holt, Rinehart and Winston, Inc., New York, 436-438 (1969).

4. M. STEINER and N. LAZAROFF, "Direct Method for Continuous Determination of Iron Oxidation by Autotrophic Bacteria," *Appl. Microbiol.*, 28, 872-880 (1974).

5. J. A. JOHNSON and H. B. SMARTT, "Advantages of an Alternative Form of Fuzzy Logic," *IEEE Transactions on Fuzzy Logic*, In Press, 1995.

6. P. GRAINDORGE, S. CHARBONNIER, J. P. MAGNIN, C. MAUVY, and A. CHERUY, A Software Sensor of Biological Activity Based on a Redox Probe for the Control of *Thiobacillus ferrooxidans* Cultures," *J. Biotechnol.* 35, 87-96 (1994).

Control of Complex Dynamics and Chaos in Distributed Parameter Systems

S. Chakravarti M. Marek* W. H. Ray†

Department of Chemical Engineering,
University of Wisconsin,
Madison, WI 53706

Abstract

This paper discusses a methodology for controlling complex dynamics and chaos in distributed parameter systems. The reaction-diffusion system with Brusselator kinetics, where the torus-doubling or quasi-periodic (two characteristic incommensurate frequencies) route to chaos exists in a defined range of parameter values, is used as an example. Poincaré maps are used for characterization of quasi-periodic and chaotic attractors. The dominant modes or topos, which are inherent properties of the system, are identified by means of the Singular Value Decomposition. Tested modal feedback control schemas based on identified dominant spatial modes confirm the possibility of stabilization of simple quasi-periodic trajectories in the complex quasi-periodic or chaotic spatiotemporal patterns.

Introduction

The discussion of problems connected with the development of a systematic framework for control of complex dynamics and chaos in distributed parameter systems is the subject of this work. The control of complex dynamics has significant practical implications. Transition to chaos via the quasi-periodic route occurs in a number of hydrodynamic and other systems. Control of such transitions could be used to improve characteristics of process systems. The issue of chaos control in distributed parameter systems (DPS) has been discussed in several papers [1]. However, there do not appear to be studies that address the problem of controlling chaos when it occurs through the quasi-periodic route in a DPS. The focus of this effort is to explore the possibility of controlling the chaotic attractor in a distributed system to one of the quasi-periodic attractors, namely tori from which it evolves based on an understanding of the underlying dynamics. The distributed parameter system considered is of the reaction-diffusion type with Brusselator kinetics. A quasi-periodic or torus doubling route to chaos is known to exist in the selected region of parameter space [2]. In order to achieve the desired control objective, it was found useful to combine ideas from previous work in the area of control of chaos in lumped parameter systems (LPS) and low dimensional maps [1], general methodology of identification and control of distributed parameter systems [3] and analysis of spatiotemporal patterns in distributed systems [4].

*Permanent Address: Dept. of Chemical Engineering, Prague Institute of Chemical Technology, Prague, Czech Republic

†Author to whom correspondence should be addressed

System description

The *Brusselator reaction kinetic scheme* is a standard model system used for the study of dissipative structures in nonlinear chemical systems [5]. The reaction scheme involves the transformation of initial components A and B into products D and E through the reaction intermediates X and Y.

$$\begin{aligned} A &\xrightarrow{k_1} X \\ B + X &\xrightarrow{k_2} Y + D \\ 2X + Y &\xrightarrow{k_3} 3X \\ X &\xrightarrow{k_4} E \end{aligned}$$

The case of the Brusselator reaction occurring in a membrane reactor is studied in this work. It is assumed that the reactor remains isothermal. A possible reactor design is shown in Figure (1). The reaction medium in the reactor is in a thin tube without radial variations in composition. The concentrations of A and B and of the products D and E in the reactor are controlled by a lateral semipermeable membrane between the reactor tube and the zoned chambers formed by the tube jacket. There are 19 such zoned chambers with concentrations being measured by sensors located at the mid-point of each zone. The only exceptions are the zones at either end which are 1.5 times longer than the rest and have measurement sensors at the two-thirds point. Separate membranes at the end of the reactor control the concentration of intermediates X, Y at each end of the tube. There is no convective contribution so that the system could be alternately viewed as a series of well mixed reaction cells coupled by diffusion. The governing set of partial differential equations for the Brusselator kinetics in a reaction-diffusion system can be expressed as [2, 5]:

$$\frac{\partial X}{\partial t} = \frac{D_X}{L^2}\frac{\partial^2 X}{\partial z^2} + X^2Y - (B+1)X + A \tag{1}$$

$$\frac{\partial Y}{\partial t} = \frac{D_Y}{L^2}\frac{\partial^2 Y}{\partial z^2} - X^2Y + BX \tag{2}$$

The length of the reactor L is chosen as the bifurcation parameter. The diffusion coefficients

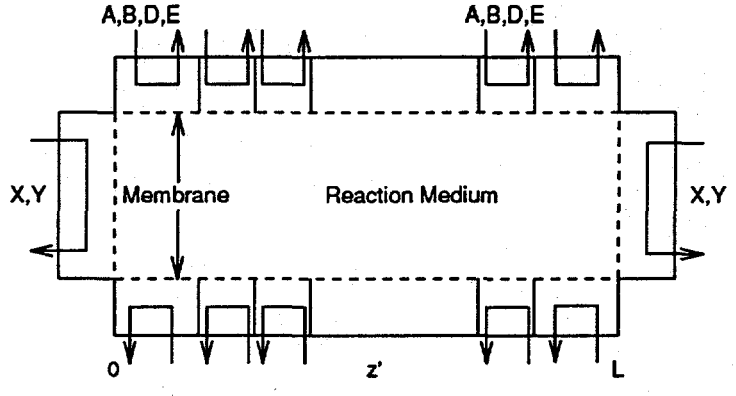

Figure 1: Membrane Reactor Geometry.

D_X, D_Y of X and Y are chosen as 0.008 and 0.004 respectively. The dimensionless distance coordinate z ranges from 0 to 1. Also, A and B are 2.0 and 5.45 respectively. The boundary conditions are of the Dirichlet type:

$$X(t,0) = X(t,1) = \bar{X}, \quad Y(t,0) = Y(t,1) = \bar{Y} \tag{3}$$

where $\bar{X}$ and $\bar{Y}$ are the steady state concentrations in the homogeneous system. Thus $\bar{X} = A = 2$ and $\bar{Y} = B/A = 2.725$.

For purposes of computation of spatiotemporal data for dynamic analysis, the finite difference approximation, where the spatial domain is discretized into 20 intervals of equal length, is used. Holodniok et al [2] observed that the leading eigenvalues of the monodromy matrix, a measure of the stability of the periodic solution, were almost identical for 20 and 40 intervals. Also, we found the results of the simulations performed with 40, 80, 160 intervals to be consistent with those for 20.

Poincaré maps

The nonlinear dynamics of interest can be studied by means of properly chosen Poincaré maps. The Poincaré map for the present problem essentially represents the intersection of the trajectory obtained by integration of equations (1) and (2) and a 37-dimensional hypersurface suitably defined. For example, the surface could be defined by the following equation:

$$X_{z=0.3}(t) = 2.0 \tag{4}$$

with $dX_{z=0.3}(t)/dt > 0$. The Poincaré map would then contain only those spatial profiles which satisfy the requirement of equation (4) as denoted by solid lines in Figures (2a) and (2b). To represent the Poincaré map in two dimensions it becomes necessary to project the map onto chosen two phase-space coordinates i.e. concentrations of X and Y at chosen location in the reactor. The concentrations of X and Y at $z = 0.5$ when the concentration of X at $z = 0.3$ is 2.0 and increasing (see points Q and R in Figure (2)) were used here. In such a 2D map, a single point denotes periodic behavior. A closed orbit indicates quasi-periodic behavior (or torus) while a double closed orbit would suggest a torus doubling.

Equations (1) and (2) were integrated using two sets of initial conditions. The first set of initial conditions, denoted by A (or IC-A) throughout this paper, corresponds to:

$$X = 2.32,\ Y = 1.75 \text{ for } z < 0.5 \text{ and } X = 3.32,\ Y = 2.75 \text{ for } z \geq 0.5$$

The second set of initial conditions, referred to as B (or IC-B) is the mirror image of the initial condition A. The Poincaré maps that result as L is varied from 1.403 to 1.43 are presented in Figure (3), which reveals the existence of two co-existing and mutually mirror-symmetric spatially asymmetric attractors. The symmetry arises from the symmetry in the geometry of the problem and the solution reached depends on the initial conditions used.

Singular Value Decomposition (SVD)

Spatiotemporal patterns can be better understood if they are decomposed into time-independent spatial structures and their time-varying amplitudes. This orthogonal decomposition can be accomplished by means of the Singular Value Decomposition [6]. Implementation of SVD in this context is in principle similar to the Karhunen-Loéve expansion. The SVD analysis is

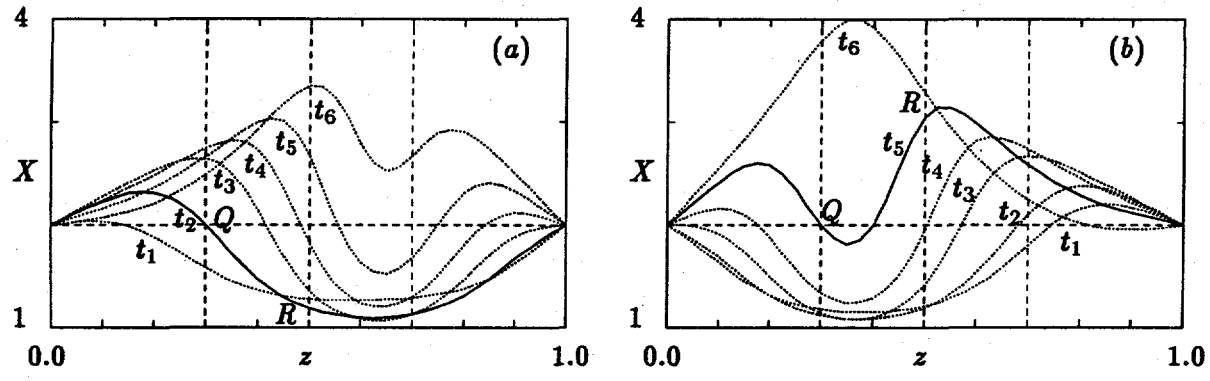

Figure 2: Selecting spatial profiles for Poincaré maps of DPS. (a) and (b) correspond to initial conditions A and B (cf. text). $t_1 < t_2 < t_3 < t_4 < t_5 < t_6$. Equation (4) defines the Poincaré surface.

applied to both reactants X and Y. The spatiotemporal data for reactant X typically consists of M snapshots at N points in space which constitutes an $N \times M$ matrix $\mathbf{X}'$. Application of the matrix SVD yields left and right unitary singular matrices and a diagonal singular value matrix. The columns of the left (spatially dependent) and right (time dependent) singular vectors are referred to as topos and chronos respectively.

Figure (4) illustrates the behavior of the topos, $\mathbf{w_i}(z)$, corresponding to the first two modes ($i = 1, 2$) when using initial condition A. Initial condition B yields a set of topos $\mathbf{w_i^*}(z)$ which satisfies the condition $\mathbf{w_i^*}(z) = \mathbf{w_i}(1 - z)$. The $(z, 1 - z)$ relation indicates that the symmetry is of the same mirror-image type seen in the Poincaré maps. The topos $\mathbf{w_i}(z)$ are *inherent properties* of the system and were found to fluctuate very little as L was varied.

From the square of the singular values, the relative energy of each mode can be assessed. The singular values are arranged in descending order. It was found that about 85% of the energy is concentrated in the first mode itself and another 12% in the second mode. Also the distribution of the energy amongst the dominant modes remained similar throughout the regime of transition to chaos i.e. $L = 1.403$—1.43. This observation coupled with the robustness of the topos lends support to the idea that in a feedback control framework, desirable performance could be achieved by controlling the first mode alone.

Modal Feedback Control

The primary goal is to develop a feedback control framework which would facilitate control of the chaotic attractor to any of the tori from which it evolves or vice-versa or from one torus to another. A modal feedback control methodology that accounts for the spatial nature of the output is schematically depicted in Figure (5). A detailed account of the different modal control schemes used can be found in [7].

First, let us suppose that we wish to control the chaotic attractor to the 1-torus. Let $X(z, t)$ in the open loop represent chaotic behavior and $X_{sp}(z, t)$ be indicative of the desired quasi-periodic behavior. Thus the set point is a dynamically varying profile. $\varepsilon(z, t)$ is the deviation

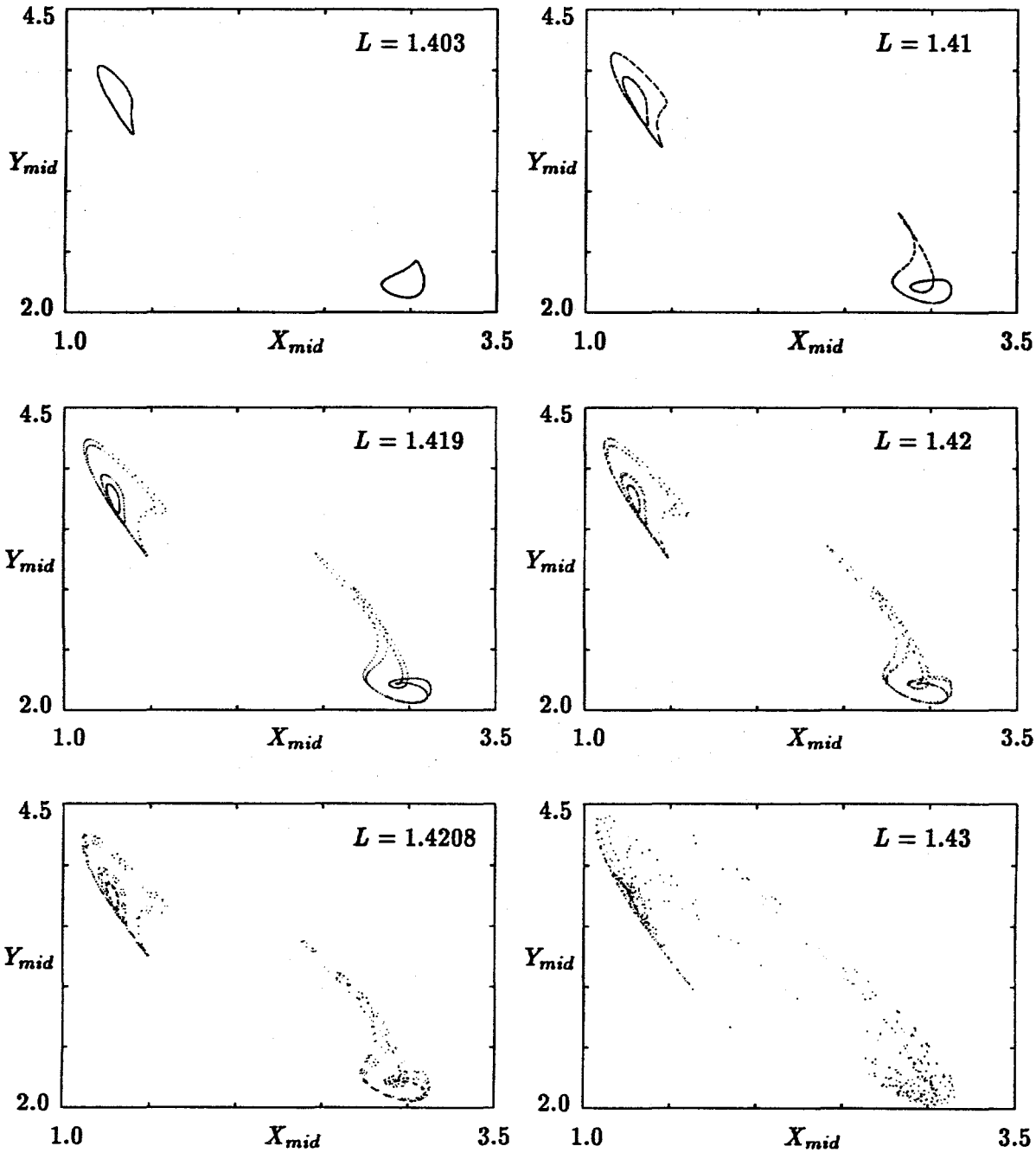

Figure 3: Poincaré maps. The horizontal and vertical axes represent the concentration of X and Y at the midpoint, $z = 0.5$. The attractors in the top left corner are obtained using initial condition A while the ones in the bottom right correspond to initial condition B. Equation (4) defines the Poincaré surface.

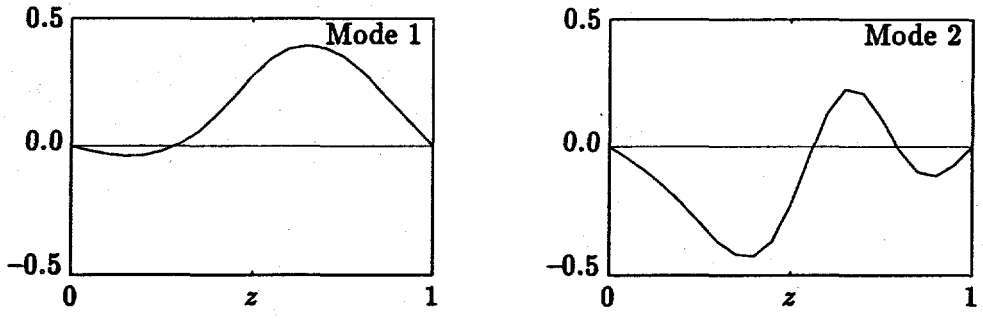

Figure 4: Topos for modes 1 and 2 with $L = 1.403$. Initial condition A is used. The horizontal axes denote the distance coordinate while the vertical axes represent the magnitude of the topos.

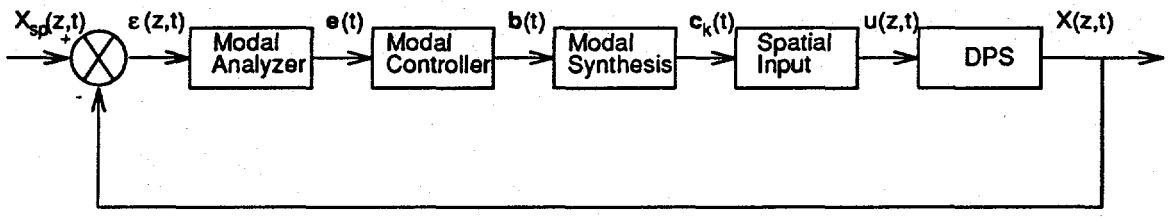

Figure 5: Modal feedback control scheme.

of the output profile $X(z,t)$ from the set point $X_{sp}(z,t)$:

$$\varepsilon(z,t) = X_{sp}(z,t) - X(z,t) \tag{5}$$

Since the topos $w_i(z)$ were shown to be intrinsic properties of the system (i.e. consistent throughout the transition regime), the modal error vector $\mathbf{e}(t)$ is obtained by projecting the deviation $\varepsilon(z,t)$ onto the topos.

$$e_i(t) = \int_0^1 \varepsilon(z,t) w_i(z)\, dz \tag{6}$$

The modal controller computes the control coefficients $b_i(t)$ corresponding to each $e_i(t)$. A suitable form of control law could be used. For instance, with proportional control, $b_i(t) = Ke_i(t)$. The control action $u(z,t)$ is then obtained as follows:

$$u(z,t) = \sum_{i=1}^{N} b_i(t) w_i(z) \tag{7}$$

Though a distributed parameter system is of infinite dimension (i.e. $N = \infty$), in practice N could be set to a value which ensures that the first N modes capture the desired amount (for example, 90%) of the original behavior. This information can be obtained from the singular values. It is difficult to practically implement a control action of the type described by equation (7) that is continuous in space. A more physically realizable technique would be having M zones of piecewise uniform control in the interval $z_k < z < z_{k+1}$ (cf. Figure (1) for an example). The

control action could then be expressed as:

$$u(z,t) = \sum_{k=1}^{M} c_k(t) g_k(z) \tag{8}$$

where $g_k(z) = H(z - z_k) - H(z - z_{k+1})$. $H(z)$ refers to the Heaviside step function. $c_k(t)$ can be obtained by using the orthogonality of $g_k(z)$, thus yielding the expression:

$$u(z,t) = \sum_{k=1}^{M} \sum_{i=1}^{N} K \left(\int_0^1 \left[X_{sp}(z',t) - X(z',t) \right] w_i(z')\, dz' \right) \left(\int_0^1 w_i(z') g_k(z')\, dz' \right) g_k(z) \tag{9}$$

In the reaction-diffusion system (equations (1) and (2)) control is physically accomplished by the addition or removal of reactants A and B as shown in Figure (1). The exact increments or decrements of A and B, referred to as u_X and u_Y, are computed based on the deviations of $X(z,t)$ and $Y(z,t)$ from $X_{sp}(z,t)$ and $Y_{sp}(z,t)$ respectively. Proportional feedback is used based on the observation that earlier works dealing with the problem of control of chaos have found such a scheme adequate for the purpose of stabilization of the strange attractor onto one of the embedded unstable orbits. With the inclusion of feedback control the governing equations (1) and (2) are transformed to:

$$\frac{\partial X}{\partial t} = \frac{D_X}{L^2} \frac{\partial^2 X}{\partial z^2} + X^2 Y - (B + u_Y + 1)X + (A + u_X) \tag{10}$$

$$\frac{\partial Y}{\partial t} = \frac{D_Y}{L^2} \frac{\partial^2 Y}{\partial z^2} - X^2 Y + (B + u_Y)X \tag{11}$$

The boundary conditions (equation (3)) remain unchanged. As in the case of dynamics, the computations are performed using the finite difference approximation with 20 intervals of equal length. The approach is to try several forms of modal control — 1 mode, 1 zone and 1 mode, 19 zones. Figure (6) illustrates the results of trying to direct the chaotic attractor to the 1 torus. Using 19 zones expectedly enhances the performance. The same modal feedback control scheme can also be used to control the chaotic attractor to any other torus and also any torus to the chaotic attractor or any other torus.

CONCLUSIONS

Through properly chosen Poincaré maps, it was observed that the dynamics of the reaction-diffusion system with Brusselator kinetics (in the parameter space of interest $L = 1.403$—1.43) is characterized by the presence of two co-existing and mutually mirror-symmetric spatially asymmetric attractors. The mirror-symmetry was initially ascertained from the use of mirror-symmetric sets of initial conditions. This finding was also corroborated from the relationship between the topos for the two sequences of attractors. Thus, Singular Value Decomposition proved to be a useful tool in detecting the presence of co-existing and mutually mirror-symmetric attractors. The consistency of the topos throughout the transition region coupled with the distribution of energy amongst the various modes suggested their possible use in the development of the control strategy.

Finally a modal control strategy was developed and applied to the control of chaos occurring through the torus doubling route in the reaction-diffusion system. The key idea was to compute the control action by projecting the deviation of the current dynamic behavior of the system

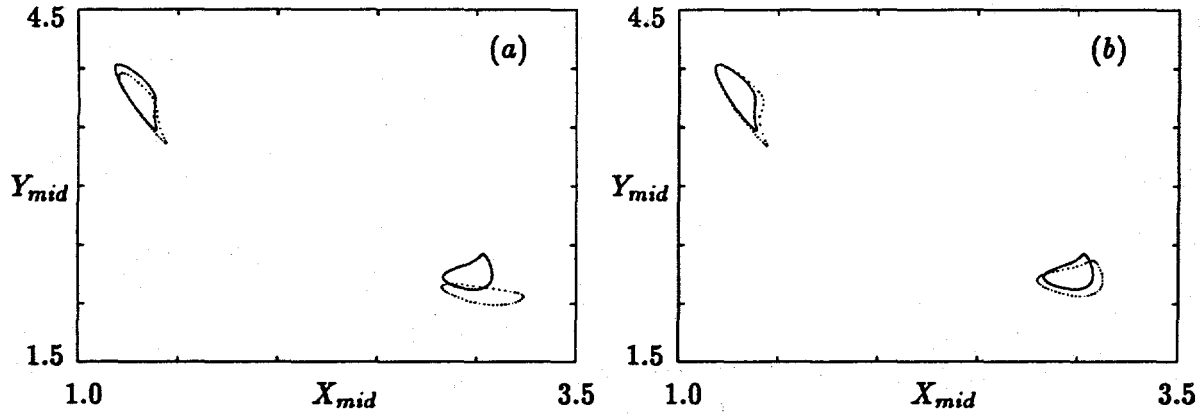

Figure 6: Poincaré map depicting the control of the open loop chaotic attractor ($L = 1.43$) to the underlying torus using (a) 1 zone, (b) 19 zones and the most dominant mode. Equation (4) defines the Poincaré surface. $K = 0.03$, solid line refers to the "set point" attractor, dots refer to the controlled attractor.

from the desired behavior onto the dominant modes. It was possible to obtain behavior close to any of the tori by suitably controlling the chaotic attractor and vice-versa. Although applied to an example which demonstrated a quasi-periodic route to chaos, the control scheme is essentially independent of the route to chaos and so could potentially be applied to instances of chaos in distributed parameter systems occurring through other routes too.

REFERENCES

[1] G. Chen. Control and Synchronization of Chaotic Systems (bibliography). EE Dept, Univ of Houston, TX - available from ftp: "uhoop.egr.uh.edu/pub/TeX/chaos.tex" (login name and password: both "anonymous").

[2] M. Holodniok, M. Kubíček, and M. Marek. Disintegration of an Invariant Torus in a Reaction-Diffusion System. Presented at the Fifth International Seminar NUMDIFF-5 held at the Martin-Luther-University, Halle, May 22-26, 1989.

[3] D. H. Gay and W. H. Ray. Identification and Control of Distributed Parameter Systems by means of the Singular Value Decomposition. *Chemical Engineering Science*, In Press.

[4] L. Sirovich. Turbulence and the Dynamics of Coherent Structures-Parts I,II,III. *Quarterly of Applied Mathematics*, XLV(3):561–590, October 1987.

[5] M. Marek and I. Schreiber. *Chaotic Behaviour of Deterministic Dissipative Systems.* Cambridge University Press, Cambridge, 1991.

[6] G. W. Stewart. On the Early History of Singular Value Decomposition. *SIAM Review*, 35(4):551–566, December 1993.

[7] S. Chakravarti, M. Marek, and W. H. Ray. Reaction-Diffusion System with Brusselator Kinetics — Control of Quasiperiodic Routes to Chaos. *Physical Review E*, In Press.

TURBULENCE GENERATION BY WAVES

D. Kaftori
X. S. Nan
S. Banerjee

Chemical Engineering Dept.
University of California Santa Barbara
Santa Barbara, CA 93106

ABSTRACT

The interaction between two-dimensional mechanically generated waves, and a turbulent stream was investigated experimentally in a horizontal channel, using a 3-D LDA synchronized with a surface position measuring device and a micro-bubble tracers flow visualization with high speed video.

Results show that although the wave induced orbital motion reached all the way to the wall, the characteristics of the turbulence wall structures and the turbulence intensity close to the wall were not altered. Nor was the streaky nature of the wall layer. On the other hand, the mean velocity profile became more uniform and the mean friction velocity was increased. Close to the free surface, the turbulence intensity was substantially increased as well. Even in predominantly laminar flows, the introduction of 2-D waves causes three dimensional turbulence. The turbulence enhancement is found to be proportional to the wave strength.

INTRODUCTION

This study is part of an ongoing research effort in our laboratory concerning turbulence at a gas-liquid interface. Previous works, both experimental and computational using direct numerical simulations, have focused on smooth turbulent open channel flows with and without imposed wind shear. In this work the question of turbulence in the presence of two-dimensional waves, moving with the current, and without wind is addressed.

One of the main effects of waves on a turbulent current is to increase the turbulence intensity close to the free surface (e.g. Kemp & Simons[1]). This may be most important in transport processes at the surface, particularly with sparingly soluble gases. The reason for the increased intensity is not clear. Rashidi et al.[2] examined this question by investigating the relationship be-

Table 1. Wave parameters

Re_h	h [mm]	H [mm]	f [Hz]	$\overline{u^*}$ [m/s]	λ [m]	Re_h	h [mm]	H [mm]	f [Hz]	$\overline{u^*}$ [m/s]	λ [m]
7500	37.2	7.0	1.90	9.4e-3	0.39	5000	40.8	6.13	2.40	6.1e-3	0.29
5000	55.0	8.4	1.90	4.8e-3	0.38	5000	41.3	12.13	2.37	6.1e-3	0.29
5000	40.5	6.4	1.62	6.5e-3	0.46	4400	39.5	5.55	2.37	6.0e-3	0.29

$Re_h = U_m h/\nu$ Reynolds number. ν is kinematic viscosity.
H Wave height.
$\overline{u^*}$ Mean friction velocity. See below.

tween the waves and the wall structures, because the structures are considered to be responsible for most of the turbulence production in the boundary layer. They found that the number of wall ejections increased in wavy flows and proposed that this may be the reason for the enhanced turbulence. However, the frequency of the bursts themselves (each containing a number of ejections), was not changed. Since it now seems that the large scale structures are the ones responsible for turbulence production (i.e., the bursts, or funnel-shaped vortices, as they were interpreted by Kaftori et al.[3]), rather than the internal structures (i.e., separate ejections), this question remains unresolved. In addition, Rashidi et al. could not make measurements very close to the wall and could not measure the variations in turbulence quantities there.

In this work the increased turbulence in wavy flow was examined. The rate of increase throughout the flow profile was measured in an attempt to identify the causes and mechanisms that govern it. Other turbulence characteristics, such as the velocity profile, friction velocity, and the wall structures, were also measured and observed. While the exact causes for the enhanced turbulence still remain unclear, the results obtained suggest that they are not related to the wall layer. Instead, it appears that they originate at the wavy interface. In addition, a relationship between the rate of increased intensity and the wave strength is presented.

EXPERIMENTS AND PROCEDURE

Experiments were conducted in an open water flume with waves superimposed onto the turbulent stream by a mechanical wedge-shaped wave maker. A diagram of the system is shown in

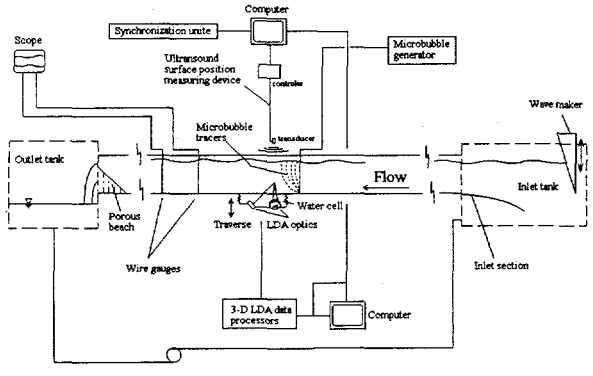

Figure 1: The experimental facility.

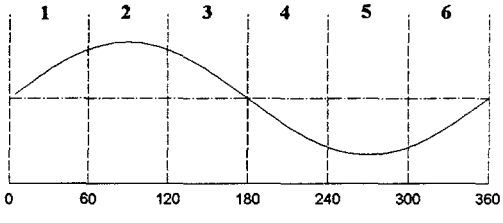

Figure 2: Wave phase division.

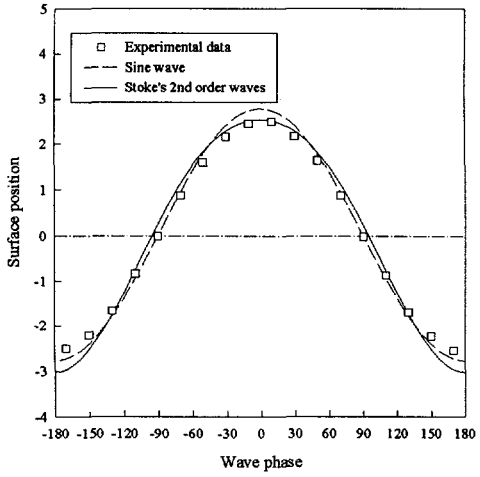

Figure 3: A comparison between a typical wave from the experiments, a sine wave, and a second order Stoke's wave.

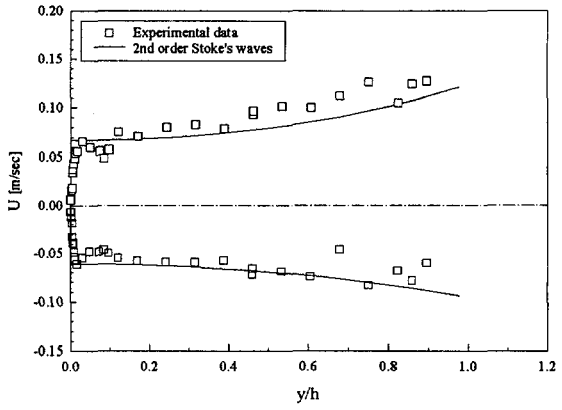

Figure 4: Wave velocity profile under the crest, in experiments and by assuming Stoke's second order waves.

Figure 1. The mean water depth in the channel was typically in the range of 40-55 mm.

The channel was equipped with a 3-D laser Doppler anemometry system for data acquisition, an ultrasound distance measuring device (Air gauge) for surface elevation measurements, and a microbubble tracers flow visualization apparatus with high speed video. The LDA and Air Gauge were synchronized so that each velocity data point could be related to the correct wave phase. In addition, two wire gauges, each measuring the instantaneous water depth, were used.

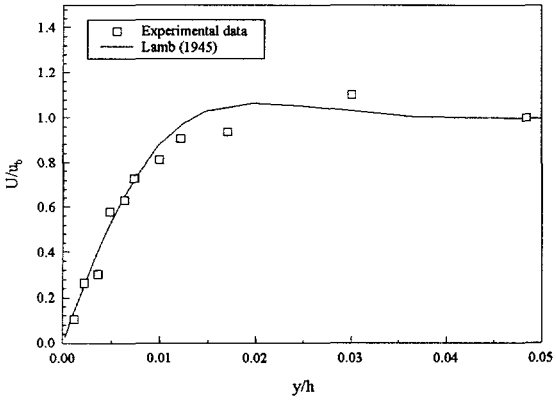

Figure 5: Wave velocity profile under the crest in the wave boundary layer, in experiments and according to Lamb[4]. Normalized by the velocity at the edge of the wave boundary layer.

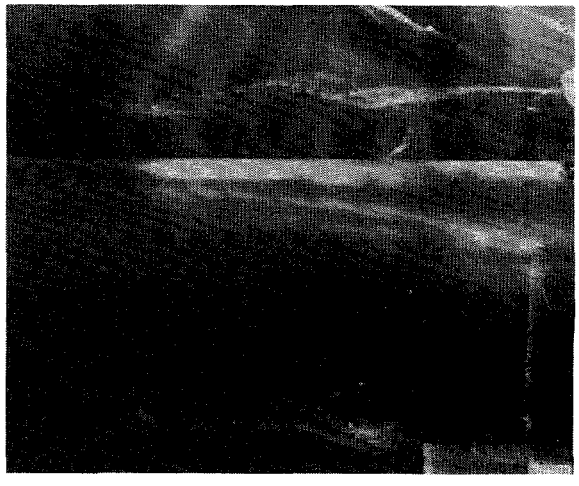

Figure 6: Funnel-shaped streamwise vortices in a wavy flow. Top - plan view from underneath. Bottom - side view. Microbubble tracers were generated only in the lower 1/3 of the flow. Scale: width of photo ~600 wall units.

The gauges were displaced in the streamwise direction so that the phase lag between them could be used as a measure of the wave length λ. The measured wave length was within 7% of the theoretical length, based on linear wave theory:

$$(\omega - kU_m)^2 = gk \cdot \tanh(kh) \quad , \tag{1}$$

where $\omega=2\pi f$ is wave period with f the wave frequency, $k=2\pi/\lambda$ is wave number, U_m is mean velocity of the turbulent current, g is gravitational acceleration, and h is mean water depth.

In all, 6 experiments with waves were conducted, along with several runs with a smooth surface. The wave parameters were varied between experiments and are detailed in Table 1.

In order to distinguish between the various contributions to the velocity field, each measured velocity data - u, was decomposed into mean velocity of the turbulent stream - U, wave induced fluctuations - u_w, and turbulence fluctuations - u', as:

$$u = U + u_w + u' \quad . \tag{2}$$

The average (mean) velocity was computed at each measuring point as:

$$U = \frac{1}{n}\sum u \quad , \tag{3}$$

where n is the number of data samples. The wave induced velocity was calculated for each phase of the waves by dividing the waves into 6 (or, in some experiments, 18) sections, each representing a phase, as in Figure 2. The average wave induced velocity was then calculated for each phase:

$$u_w\Big|_{ph} = \overline{u_i}\Big|_{ph} - U \quad . \tag{4}$$

Here $u_i\Big|_{ph}$ is a velocity data point at a given phase of the wave, and the overbar represents an average over all waves. In determining the wave phase of each data point, the information col-

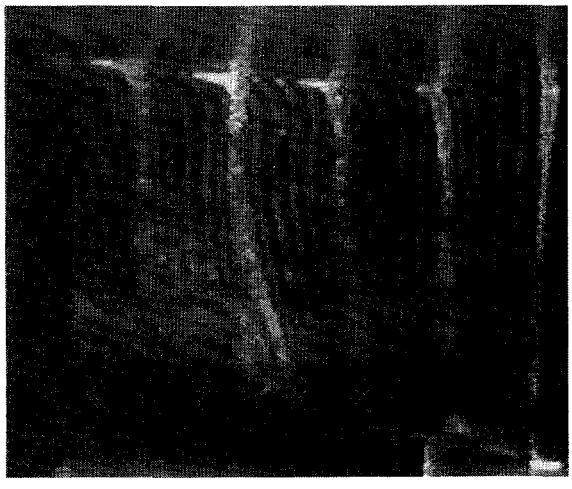

Figure 7: Instantaneous velocity profile under wave trough. Note flow reversal at the surface and close to the wall. Scale: width of photo ~340 wall units.

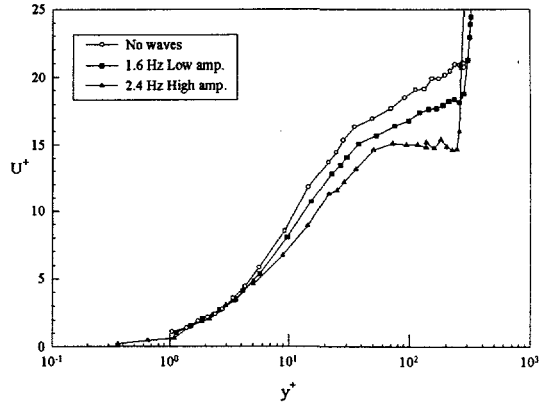

Figure 8: Normalized mean velocity profiles in smooth and wavy flows.

lected from the ultrasound surface elevation measurements was used. The fluctuating turbulence velocity component was deduced from Eq. (2).

In order to qualify the type of waves in the experiments, the measured velocities and wave forms were compared with some establish wave types. Figure 3 depicts a typical wave form measured in an experiment together with a sinusoidal wave form and a second order Stokes wave given by:

$$\eta = \frac{H}{2}\cos(kx-\omega t)+\frac{Hk}{16}\frac{\cosh(kh)}{\sinh^3(kh)}[2+\cosh(kh)]\cos[2(kx-\omega t)] \quad , \tag{5}$$

where x is the streamwise coordinate and t is time. The first term on the right is the sine wave in the figure. As can be seen, the waves were close to second order waves but with a somewhat sharper crest, implying a higher order of non-linearity. The wave velocity profile was also in agreement with that of second order Stoke's waves, as illustrated in Figure 4. Close to the wall the wave velocity was also in agreement with Lamb's[4] prediction, based on linear wave theory, as shown in Figure 5.

RESULTS

Wall Structures

The behavior of turbulence wall structures in wavy flow was examined and compared to smooth flow using microbubble tracers with high speed video. These observations show that the same structures which are seen in smooth flows appear in wavy flow as well. These funnel-shaped vortical structures (see Kaftori et al.[3]), originate close to the wall and stretch in the streamwise direction while expanding outward from the wall in a spiraling motion. In wavy flow the structures seem to be of the same size and shape, as shown in Figure 6. This was true in spite of the fact that the effect of the waves was apparent all the way to the wall, where the orbital wave induced velocity caused the flow to reverse at the wall, as shown in Figure 7.

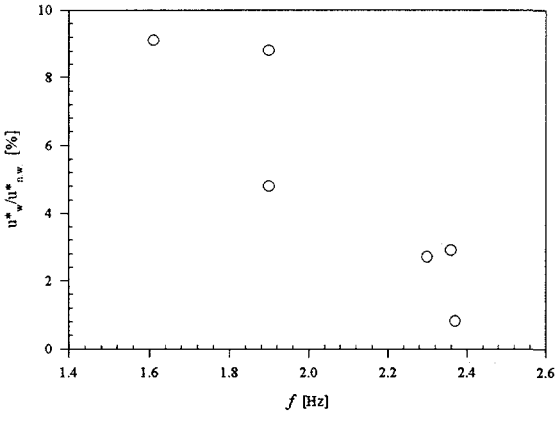

Figure 9: Percent increase in friction velocity as a function of wave frequency.

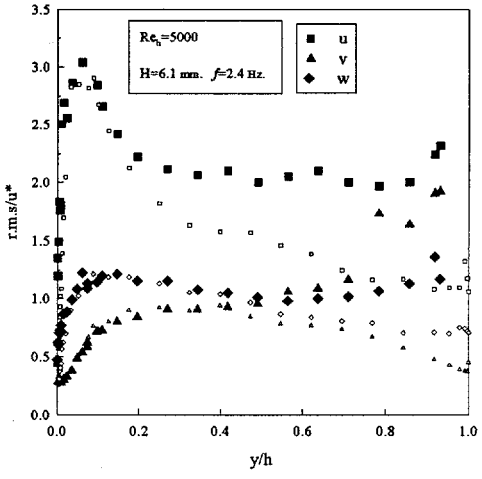

Figure 10: Turbulence intensities profile (wave induced velocity removed).

The streaky structure of the wall layer, typical to smooth flow, was also preserved when waves were introduced. The streak spacing seemed to remain approximately the same (~100 wall units). It seems that the streaks became better defined, with a larger difference between the streamwise velocity of the high- and low-speed regions. Similar observations were make by Rashidi et al.[2].

Velocity profile

The effect of surface waves on the mean velocity profile is shown in Figure 8. It appears that the waves reduce the mean velocity in the outer part of the flow but do not affect the profile in the wall layer. In general, the velocity profiles become more uniform and the effect is stronger with larger waves. The deficit in mass flow rate due to the lower velocities in the figure is balanced by the flow in the crest region of the waves. The instantaneous velocity profiles varied with wave phase. An example of the profile under a trough was given in Figure 7, where the velocity is reversed close to wall, positive in the mid section, and is negative again close to the free surface. The same type of instantaneous profile was recorded by Kemp & Simons[1].

The mean friction velocity $\overline{u^*}$, was calculated from the average velocity profile in the viscous layer ($y^+ \leq 5$). In wavy flows the friction velocity was up to 10% higher than in smooth flow. The increase was proportional to the wave length, and indirectly proportional to the frequency, as depicted in Figure 9.

Turbulence intensities

r.m.s velocity fluctuations of a wavy flow are compared to those of smooth flow in Figure 10 with the wave induced fluctuations removed, the r.m.s. curves are of the same shape as in smooth flow but the intensities of the three components are higher in the upper portion of the flow profile. The increase was larger for stronger waves. The waves did not affect the r.m.s close to the wall.

These results imply that turbulence production occurred in the upper portion of the flow as a result of the waves. While wave induced motion can be seen throughout the flow profile, they seem not to affect the turbulence wall structures, which are generally responsible for most of the turbulence production, nor alter the shape or magnitude of the turbulence intensities in the wall region. They do, however, significantly increase the intensities close to the free surface. Thus it appears that unlike simple turbulent open channel flow, where wall shear is the primary mechanism for turbulence production, in wavy flow there exists another production mechanism. This turbulence source is strongest close to the wave trough and weakens toward the wall.

In order to test this hypothesis, turbulence production in laminar wavy flow was examined using dye and particle tracers flow visualization. In these experiments dye diffusion and particle dispersion were observed and measured in both simple laminar flow, and in laminar flow with waves. Figure 11 is a sample of a dye diffusion experiments. In simple laminar flow there is hardly any diffusion at all. In the wavy flow, on the other hand, there is turbulent diffusion and the dye is dispersed immediately. The diffusion was three dimensional, with the same rate of dispersion in the spanwise direction as in the wall normal direction. The spanwise dispersion can only be accounted for by turbulence.

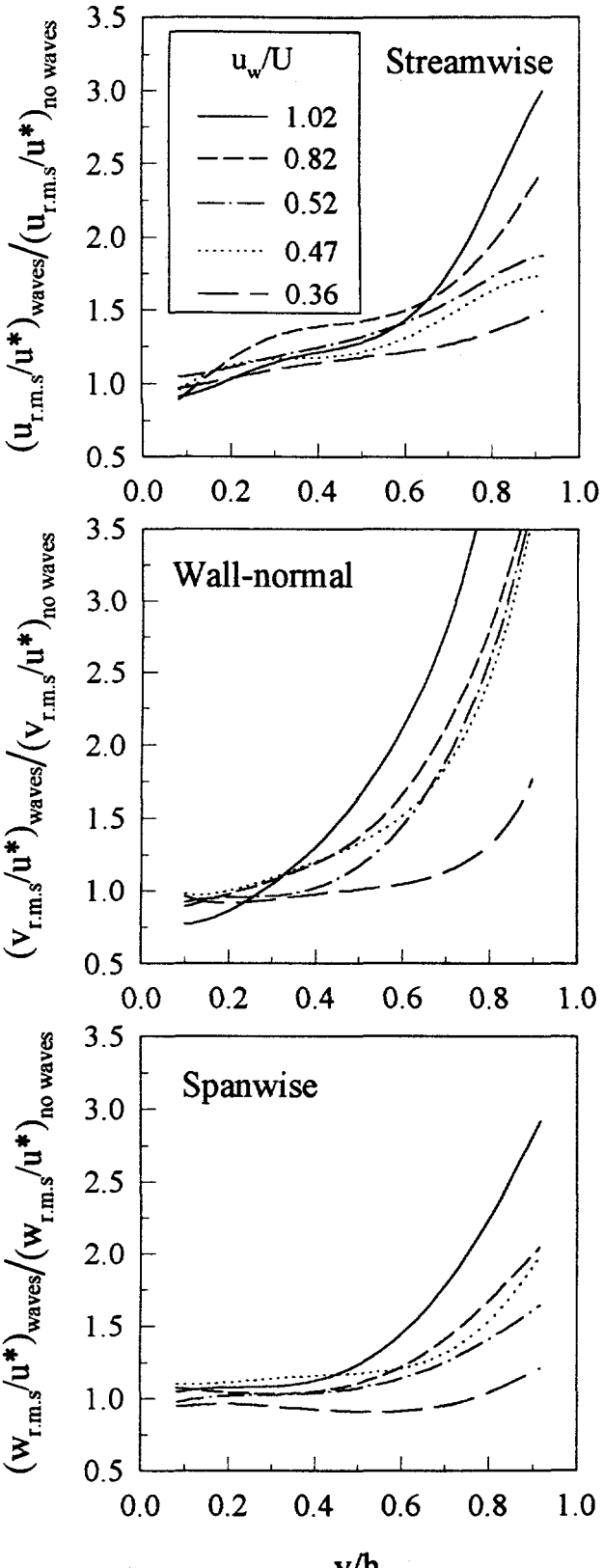

Figure 12: Increase in r.m.s level in wavy flow compared to smooth flow, as a function of wave strength. Lines are curve fits.

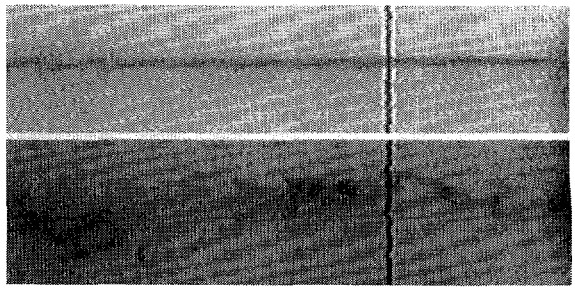

Figure 11: Dye diffusion experiment.
Top - Simple laminar flow.
Bottom - Laminar flow with waves.

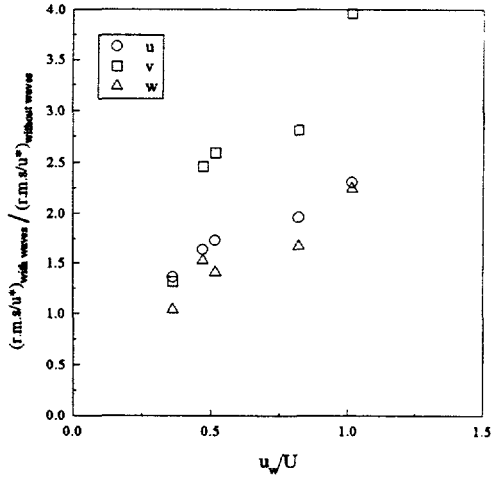

Figure 13: Increase in r.m.s levels with waves at y/h=0.8.

In the particle tracers experiments, polystyrene particles (specific density ~1.05, nominal diameter 275 μm) were released into the flow and were photographed using high speed video. Their spanwise displacement was then measured in order to examine the particle spanwise dispersion. Results show that in wavy flow the particle spanwise dispersion rate was up to three times higher compared to the non-wavy flow. These findings confirm that three-dimensional turbulence is generated by the predominantly two-dimensional waves.

As mentioned above, the rate of turbulence production due to waves increased with wave amplitude and frequency. Figure 12 shows the increase in turbulence intensities of the three velocity components as a function of wave strength, defined as the ratio of (a fluid) particle velocity to mean current velocity. The particle velocity at the mean water level was used. As can be seen, the r.m.s level in the upper half of the flow profile increases with increasing wave strength. In order to quantify this behavior, the r.m.s increases of all runs were compared at y/h=0.8. Results are in Figure 13. There it seems that the increase is directly proportional to wave strength.

The reason for the turbulence enhancement by the waves is still not clear. Evidently, it must be related to a coupling between the wave induced velocity fluctuations and the turbulence fluctuations, resulting in additional Reynolds stress-type terms in the momentum equation. In addition, since a wave induced drift usually exists in wavy flows (Phillips[5]), additional viscous shear may be introduced. These points and their relative importance are currently under investigation.

CONCLUSIONS

The introduction of 2-D waves onto a turbulent stream substantially increases the level of turbulence in the upper portion of the flow, while having only little effect on the turbulence in the wall layer. Even in laminar flow the introduction of waves causes the onset of turbulence. The enhancement seems to scale with the strength of the waves, namely the ratio of wave induced velocity to the mean current velocity. Since the turbulence characteristics close to the wall, and the nature of the wall structures, seemed to be unchanged by the waves, it appears that the enhanced turbulence is not related to increased shear at the wall or to turbulence in the wall layer. Rather, it seems that it may originate at the wavy region. This must be investigated further.

REFERENCES

1 P. H. Kemp and R. R. Simons, The interaction between waves and a turbulent current: waves propagating with the current," *J. Fluid Mech.* **116**, 227-250, (1982)

2 M. Rashidi, G. Hetsroni, and S. Banerjee, "Wave-turbulence interaction in free-surface channel flows," *Phys. Fluids A* **4** (12), 2727-2738, (1992).

3 D. Kaftori, G. Hetsroni, and S. Banerjee, "Funnel-shaped vortical structures in wall turbulence," *Phys. Fluids* **6** (9), 3035-3050, (1994).

4 H. Lamb, Hydrodynamics, Sixth edition, Dover Publications, New York (1945).

5 O. M. Phillips, The dynamics of upper ocean, Cambridge at the university press (1966).

NUMERICAL SIMULATION OF HIGH REYNOLDS NUMBER BUBBLE MOTION

John B. McLaughlin
Department of Chemical Engineering, Clarkson University
Potsdam, N.Y. 13699-5705, USA

ABSTRACT

This paper presents the results of numerical simulations of bubble motion. All the results are for single bubbles in unbounded fluids. The liquid phase is quiescent except for the motion created by the bubble, which is axisymmetric. The main focus of the paper is on bubbles that are of order $1mm$ in diameter in water. Of particular interest is the effect of surfactant molecules on bubble motion. Results for the "insoluble surfactant" model will be presented. These results extend research by other investigators to finite Reynolds numbers. The results indicate that, by assuming complete coverage of the bubble surface, one obtains good agreement with experimental observations of bubble motion in tap water. The effect of surfactant concentration on the separation angle is discussed.

INTRODUCTION

Bubble motion in liquids is of interest in many engineering problems. In the context of Bioreactors, bubbles are important in mass transfer, the hydrodynamics of the reactors, and because they represent a volume that is not available for reaction [1]. Visual inspection of fluidized bed ethanol Bioreactors indicates that the bubbles are typically on the order of a few millimeters in diameter [1, 2]. A characteristic of Bioreactors is that they typically contain surface active materials in the form of biopolymers that are generated by the microbes.

Thus, it is of interest to develop models for the effect of surfactants on bubble motion. Andrews et al. [2] took a step in this direction. They developed a boundary layer analysis to describe the surfactant concentration on the upper portion of bubble. Their analysis is valid up to the point of flow separation. An interesting result is that large concentrations of surfactant can cause the point of separation to move closer to the top of the bubble, suggesting that there may be a corresponding increase in wake volume.

The approach taken by Andrews et al. cannot provide information about the nature of the wake. Ryskin and Leal [3-5] developed a numerical simulation technique for axisymmetric bubbles. They presented results for bubble Reynolds numbers as large as 200 and Weber numbers as large as 20. A surprising result was that, as they increased the Weber number for a fixed Reynolds number, flow separation from a bubble was preceded by the formation of detached eddies.

Haberman and Morton [6], Saffman [7], and Hartunian and Sears [8] reported experimental results for bubble motion in water and a variety of other liquids. Bubble velocities in distilled water and tap water are virtually the same for bubbles with equivalent spherical diameters, d_e, smaller than about $1mm$. Bubbles of this size are approximately spherical and have approximately the same drag coefficient as a rigid sphere of the same diameter. For values of d_e between $1mm$ and about $6mm$, there are significant differences between distilled water and tap water. In distilled water, the bubble rise velocity exhibits a local maximum at $d_e = 1.4mm$. Bubbles of this size rise twice as fast in distilled water as in tap water ($35cm/s$ compared to $17cm/s$). The corresponding Reynolds numbers, based on d_e, are 490 and 240.

The differences between bubble motion in distilled water and tap water have been attributed to the presence of surfactants [6-8]. The air-water interface is particularly susceptible to surfactants because of the polarity of the water molecule. Sadhal and Johnson [9] devised a theory for the effects of surfactants

on bubbles and drops for Stokes flow. They assumed that the adsorption-desorption kinetics was slow and that one could neglect surface diffusion. This approximation has been referred to as the "insoluble surfactant" approximation. They showed that the surfactant would collect in a cap on the rear portion of the bubble, and obtained an exact solution.

The insoluble surfactant approximation has been used by Stone and Leal [10] to study the effect of surfactants on bubbles in two-dimensional straining flow. They studied only the Stokes flow limit.

Pan et al. [11] used the static pendant drop method to determine the kinetic rate constants for surfactant exchange between an aqueous sublayer and an air-water interface. A key feature of their approach is the use of high volume concentrations of surfactant. They showed theoretically that, by using sufficiently high volume concentrations of surfactant, one could distinguish kinetics from diffusion. The availability of such results opens the possibility of checking the conditions of the insoluble surfactant approximation for experiments with controlled amounts of a known surfactant.

GOVERNING EQUATIONS

The numerical techniques in this study were described by Ryskin and Leal [3-5]. Therefore, this section contains only a brief summary of the equations and the computational parameters.

In what follows, the equivalent spherical radius, r_e, the bubble rise velocity, U, the liquid density, ρ, the fluid kinematic viscosity, ν, the interfacial surface tension, γ ,and the acceleration of gravity, g, will be used to make quantities dimensionless. The gas density is assumed to be negligible. The Reynolds number, Re, the Weber number, W, and the Morton number, M, may be used to characterize the fluid mechanics problem for clean interfaces:

$$Re = \frac{d_e U}{\nu} \tag{1}$$

$$W = \frac{\rho(d_e)U^2}{\gamma} \tag{2}$$

$$M = \frac{g\mu^4}{\rho\gamma^3}. \tag{3}$$

The drag coefficient, C_D, is given by

$$C_D = \frac{4}{3}\frac{(d_e)g}{U^2}. \tag{4}$$

The above quantities are related by

$$M = \frac{3}{4}C_D\frac{W^3}{Re^4}. \tag{5}$$

Figure 1 shows a (σ, x) plane in a cylindrical coordinate system (σ,ϕ, x). Following Ryskin and Leal [3], it is convenient to introduce an orthogonal, curvilinear coordinate system (ξ,η,ϕ) in which the variables ξ and η lie between 0 and 1. The coordinate mesh is shown in Figure 1. The surface of the bubble is given by $\xi = 0$. The point at infinity corresponds to $\eta = 0$. The positive x axis corresponds to $\eta = 0$ and the negative x axis corresponds to $\eta = 1$. The coordinate mapping is determined by the covariant Laplace equations as described by Ryskin and Leal. For the bubble in Fig. 1, $Re = 200$ and $W = 5$. Only half the bubble is shown since the flow is axisymmetric.

The present study is limited to axisymmetric motion. Therefore, it is convenient to use the stream-function-vorticity method. For steady motion, the governing equations, written in dimensionless form, are

$$L^2(\omega\sigma) - \frac{Re}{2}\left(\frac{\partial\psi}{\partial\xi}\frac{\partial\omega/\sigma}{\partial\eta} - \frac{\partial\psi}{\partial\eta}\frac{\partial\omega/\sigma}{\partial\xi}\right) = 0 \tag{6}$$

$$L^2\psi + \omega = 0, \tag{7}$$

where the operator L^2 is defined by

$$L^2 = \frac{1}{h_\xi h_\eta}\left[\frac{\partial}{\partial\xi}\left(\frac{f}{\sigma}\frac{\partial}{\partial\xi}\right) + \frac{\partial}{\partial\eta}\left(\frac{1}{f\sigma}\frac{\partial}{\partial\eta}\right)\right]. \tag{8}$$

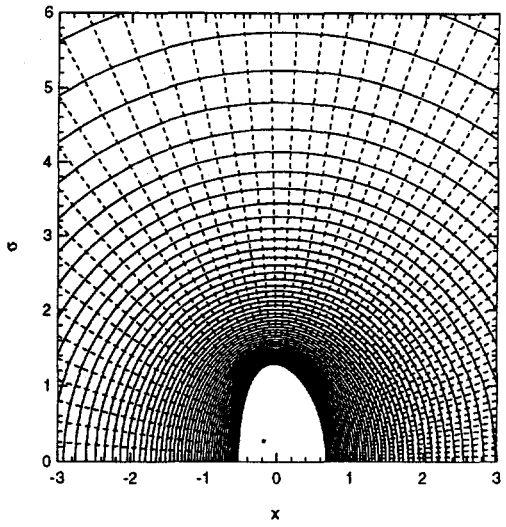

Figure 1: Coordinate Curves for a Bubble with $Re = 200$, $W = 5$

In Eqs. (6-8), ω is the ϕ component of the vorticity, ψ is the streamfunction, h_ξ and h_η are metric functions, and f is the ratio h_η/h_ξ. All quantities are dimensionless.

The pressure on the interface may be obtained by integrating the Navier-Stokes equation along the bubble surface:

$$p = \frac{3}{4}C_D x - u_\eta^2 - \frac{4}{Re}\int_0^\eta \frac{f}{\sigma}\frac{\partial}{\partial \xi}(\sigma\omega)d\eta, \tag{9}$$

where the pressure has arbitrarily been chosen to be zero at $\eta = 0$. By demanding that, in steady-state, the net force on the bubble vanishes, one may express C_D in terms of p_{dyn}, where p_{dyn} is the sum of the second and third terms on the right hand side of Eq.(9).

The boundary conditions at the surface of the bubble are as follows:

$$\psi = 0 \tag{10}$$

$$\omega - 2\kappa_\eta u_\eta = 0 \tag{11}$$

$$\tau_{\xi\xi} - \frac{4}{W}(\kappa_\eta + \kappa_\xi) = 0. \tag{12}$$

In Eqs.(10-12), κ_η and κ_ξ are the normal curvatures, u_η is the η component of the liquid velocity, and $\tau_{\xi\xi}$ is a component of the liquid stress tensor at the interface. The normal curvatures may be computed from expressions given by Ryskin and Leal [4].

The covariant Laplace equations and the streamfunction-vorticity equations are put into a canonical form discussed by Ryskin and Leal [4] and solved with the constant step ADI method suggested by Ryskin and Leal. In this iterative approach, one uses an artificial time step, Δt, and relaxation parameters for the vorticity boundary condition, β_ω and the normal stress balance, β_h.

When an insoluble surfactant is present, one must include the transport equation for the surface concentration of surfactant, Γ:

$$\nabla_s \cdot (\Gamma u_\eta - \frac{1}{P_s}\nabla_s \Gamma) = 0, \tag{13}$$

where ∇_s is the surface gradient operator and P_s is the surface Peclet number. If $P_s >> 1$, one obtains the Sadhal-Johnson result:

$$u_\eta = 0, \ \theta < \phi \tag{14}$$

$$\Gamma = 0, \ \theta > \phi, \tag{15}$$

where the angle ϕ is a cap angle in which the surfactant is concentrated. The angles ϕ and θ are measured from the positive x-axis. Thus, one may specify a cap angle and then use essentially the same procedure

as for the clean interface. The main modification is that one must impose a condition on the normal derivative of the streamfunction associated with the no-slip condition on the surfactant cap.

The calculations to be reported were performed for an "ideal gas" equation of state for the surfactant. This equation of state has the following form:

$$\gamma = \gamma_0 - RT\Gamma, \tag{16}$$

where γ is the surface tension, γ_0 is the surface tension of the clean interface, R is the gas law constant, T is the absolute temperature, and Γ is the surfactant concentration ($moles/m^2$) on the interface. This model is reasonable as long as the average distance between surfactant molecules remains large compared to the molecular size. For the calculations to be reported, this condition is satisfied.

To express Eq.(16) in dimensionless form, one can use γ_0 as the characteristic surface tension. The dimensionless surfactant concentration is defined by

$$\Gamma' = \frac{RT\Gamma}{\gamma_0}. \tag{17}$$

Thus, the dimensionless form of the ideal gas law is

$$\gamma' = 1 - \Gamma'. \tag{18}$$

The total amount of adsorbed surfactant, S, is given by the integral of Γ over the bubble surface. Using the axisymmetry of the problem, this integral may be reduced to the following form:

$$S = 2\pi r_e^2 \int_0^1 \Gamma \sigma h_\eta d\eta. \tag{19}$$

One way of characterizing the amount of surfactant is with the dimensionless parameter S' defined as follows:

$$S' = \frac{1}{4\pi r_e^2} \frac{SRT}{\gamma_0}. \tag{20}$$

One may also express S' in terms of the Marangoni number, Ma, the capillary number, C, and the dimensionless surface area, A', as follows:

$$S' = MaCA', \tag{21}$$

where

$$Ma = \frac{1}{A} \frac{SRT}{\mu U} \tag{22}$$

$$C = \frac{W}{Re} \tag{23}$$

$$A = 2\pi r_e^2 \int_0^1 \sigma h_\eta d\eta \tag{24}$$

and

$$A' = \frac{A}{4\pi r_e^2}. \tag{25}$$

NUMERICAL SIMULATIONS

Haberman and Morton [6] measured the bubble rise velocity in tap water and filtered water as well as a variety of other liquids. Figure 2 shows their measurements for tap water and filtered water. In filtered water, the bubble rise velocity reached a local maximum at $d_e = 1.4mm$. The corresponding values of Re and W are 490 and 2.35, respectively. The program was run with 61 equally spaced grid points in both the ξ and η coordinates. The computed Morton number, M, was $2.64 \cdot 10^{-11}$. The value of M for

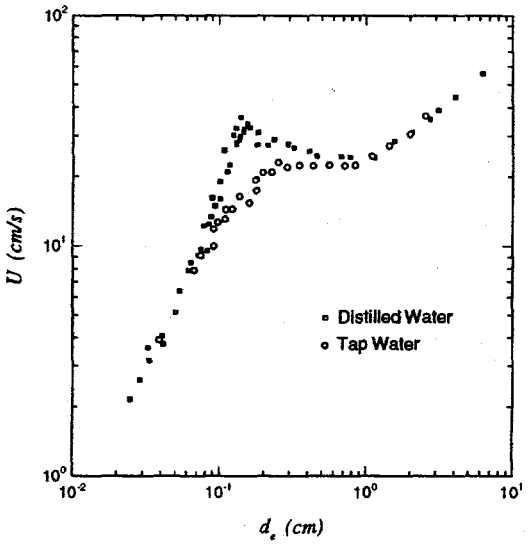

Figure 2: Bubble Rise Velocities Measured by Haberman and Morton [6]

the Haberman-Morton experiments was $2.55 \cdot 10^{-11}$. The flow did not separate, which is consistent with Hartunian and Sear's conclusion that flow separation occurs for $W > 3.2$ in clean, low Morton number fluids.

Numerous authors have suggested that the difference in bubble rise velocities between distilled water and tap water is due to the presence of surface active materials in tap water. A goal of the present work is to test this idea with computer simulations using the insoluble surfactant model. The program was tested by making a series of runs for $Re = 0.1$ and comparing the results with the Sadhal-Johnson theory. The results for the drag coefficient as a function of cap angle are shown in Fig. 3.

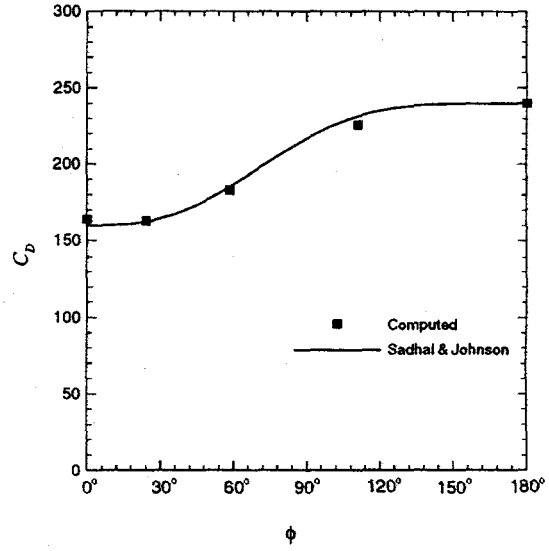

Figure 3: Computed Drag for $Re = 0.1, W = 0.02$ Compared with Sadhal and Johnson [9]

For tap water, Haberman and Morton's experiments indicate that the rise velocity of a bubble with $d_e = 1.4mm$ is approximately $17cm/s$. For such a bubble, $Re = 240$ and $W = 0.55$. A run was made with the latter values of Re and W and $\phi = 180°$. This corresponds to a bubble interface that is covered with surfactant (although the distribution is nonuniform). The computed Morton number was $2.62 \cdot 10^{-11}$. Table 1 contains a summary of runs with different cap angles, ϕ. For $\phi = 148°$, the Morton number is $2.55 \cdot 10^{-11}$. Thus, the insoluble surfactant model suggests that the rising bubbles are nearly covered

with surfactant. The value of S' is 0.0227. This may indicate that the ideal gas law is a reasonable way of estimating the surface tension. For example, Andrews et al. [2] estimated the maximum surface concentration of heptanoic acid to be $4.4 \cdot 10^{-10} cm^2/s$. The corresponding value of S' is 0.142. The average distance between molecules at close packing is about $6\mathring{A}$. Other molecules with comparable (low) solubilities in water will likely have about the same maximum surface concentration. The maximum bulk solubility of heptanoic acid in water at room temperature is $8mg/L$.

Table 1

Computer Runs for $Re = 240$, $W = 0.55$

ϕ	C_d	$M \cdot 10^{11}$	θ_{sep}	A'	χ	S
0^o	0.192	0.722		1.000	1.070	0
16.6^o	0.192	0.724		1.000	1.070	0.000011
26.0^o	0.194	0.729		1.000	1.070	0.000054
32.1^o	0.196	0.736		1.000	1.069	0.000120
36.5^o	0.198	0.744	8.06^o	1.000	1.068	0.00019
60.5^o	0.221	0.832	36.8^o	1.000	1.058	0.00139
90.8^o	0.353	1.33	58.1^o	1.000	1.039	0.00555
111.9^o	0.495	1.86	64.9^o	1.000	1.038	0.0103
134.8^o	0.633	2.38	67.3^o	1.000	1.041	0.0179
148.4^o	0.680	2.56	68.0^o	1.000	1.042	0.0227
166.4^o	0.697	2.62	68.5^o	1.000	1.043	0.0273
180^o	0.698	2.62	68.6^o	1.000	1.043	0.0287

Figure 4 shows the dimensionless surface tension as a function of the polar angle measured from the positive x-axis (i.e., measured from the direction of liquid motion in the bubble frame of reference). For this figure, $\phi = 180^o$. The surface tension varies by only a few percent even though this variation is sufficient to immobilize the interface. The surface tension at $\theta = 180^o$ is taken to be the surface tension of pure water. This assumption is not necessary. However, in modeling tap water, it produces results that agree well with experiment.

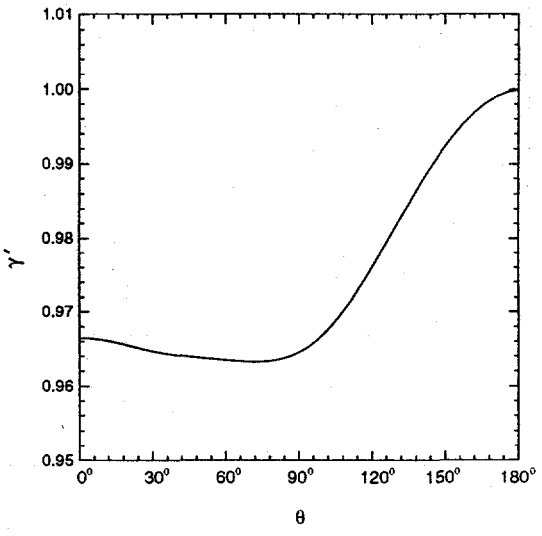

Figure 4: Dimensionless Surface Tension as a Function of Polar Angle for $Re = 240$, $W = 0.55$, and $\phi = 180^0$

Even in distilled water, bubbles that are smaller than about $0.8mm$ behave like rigid spheres. Thus, there is evidently enough surface active material to immobilize the surface of sufficiently small bubbles.

Does this low level of surfactant have an effect on the $1.4mm$ bubble considered earlier? Figure 5 shows the drag coefficient as a function of the cap angle for $Re = 490$, $W = 2.35$. One can obtain the observed rise velocity in two ways. One way is to assume that the interface is completely clean. The other way is to assume that the cap angle is approximately 105^o. The corresponding value of S' is 0.015, which is considerably lower than the value for tap water (0.023), but still significant. An important consequence of the adsorbed surfactant is that there is sizeable wake behind the bubble. The separation angle is close to 75^o. This may be consistent with the experimental observations made by Subramanian and Tien [12]. Subramanian and Tien performed visualization experiments using India ink. The experiments indicated the presence of a sizeable wake behind bubbles that were roughly $1mm$ in diameter even in distilled water. However, the ink may have acted as a surfactant. If the above inference is correct, it indicates that the boundary layer analyses based on potential flow theory such as those of Moore [13-14] are in inappropriate for bubbles in distilled water.

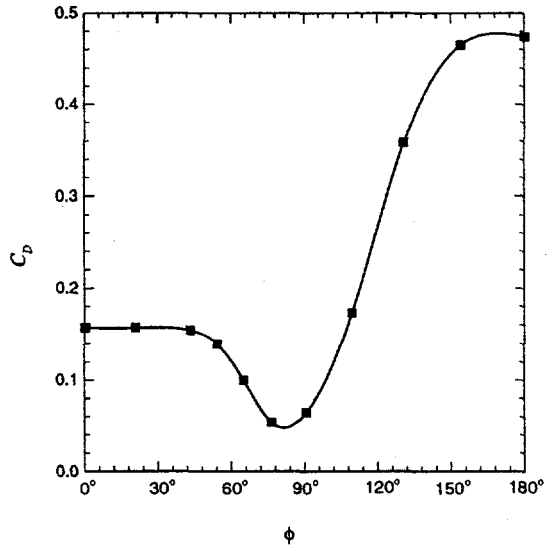

Figure 5: Drag Coefficient as a Function of Cap Angle for $Re = 490$, $W = 2.35$

The results for water indicate that surfactants have little effect on the rise velocities of bubbles with $W = 5$. The Reynolds number of these bubbles is 1600. Calculations at such a Reynolds number would be computationally expensive. According to Hartunian and Sears, the Reynolds number should have little effect on the stability of the bubble for $Re > 200$. Therefore, a run was made for a clean bubble with $Re = 200$ and $W = 5$. The corresponding Morton number is $4.26 \cdot 10^{-8}$. To determine the effect of surfactant on the wake, runs were made at smaller Reynolds numbers with different cap angles. To simplify the physical interpretation, the bubble volume was held constant. This was done by computing the Weber number as follows:

$$W = 5(\frac{Re}{200})^2. \tag{1}$$

For each Reynolds number, the cap angle was varied to obtain the correct Morton number. The Reynolds number for $\phi = 180^o$ is 167. Therefore, surfactant has relatively little effect of on the motion of bubbles of this size. However, the wake is considerably larger for contaminated interfaces. For the clean interface, the separation angle is 57.2^o, but, for complete coverage, the separation angle is 79.9^o. For a rigid sphere, the separation angle is 70.4^o.

CONCLUSIONS

The Ryskin-Leal simulation technique has been used to compute axisymmetric bubble motion at higher Reynolds numbers than previously reported. The effects of an insoluble surfactant have been included using

the ideal gas model. Assuming complete coverage, one obtains good agreement with the observations for a $1.4mm$ bubble in tap water. The computations predict the existence of a large wake behind the bubble. The computations also reveal the possibility that the bubble may possess a large wake in distilled water. This suggests that boundary layer treatments based on potential flow theory may be inappropriate even for distilled water.

Computations at large Weber numbers show that the the surfactant has little effect on the bubble rise velocity. However, the bubble wake is increased substantially.

ACKNOWLEDGEMENT

The author gratefully acknowledges helpful discussions with Dr. Brian Davison and Dr. Charles Maldarelli.

REFERENCES

1. R. BAJPAI, J.E. THOMPSON, and B.H. DAVISON, "Gas holdup in three-phase immobilized-cell Bioreactors," *Appl. Biochem. Biotech.* 24/25, 485-496 (1990).

2. G.F. ANDREWS, R. FIKE, and S. WONG, "Bubble hydrodynamics and mass transfer at high Reynolds number and surfactant concentration," *Chem. Eng. Sci.* 43, 1467-1477 (1988).

3. G. RYSKIN and L.G. LEAL, "Orthogonal mapping," *J. Comput. Phys.* 50, 71-100 (1983).

4. G. RYSKIN and L.G. LEAL, "Numerical solutions of free-boundary problems in fluid mechanics. Part 1. The finite difference technique," *J. Fluid Mech.* 148, 1-17 (1984).

5. G. RYSKIN and L.G. LEAL, "Numerical solutions of free-boundary problems in fluid mechanics. Part 2. Buoyancy-driven motion of a gas bubble through a quiescent liquid," *J. Fluid Mech.* 148, 19-35 (1984).

6. W.L. HABERMAN and R.K. MORTON, "An experimental investigation of the drag and shape of air bubbles rising in various liquids," *David Taylor Model Basin, Rep.* no. 802 (1953).

7. P.G. SAFFMAN, "On the rise of small air bubbles in water," *J. Fluid Mech.* 1, 249-275 (1956).

8. R.A. HARTUNIAN and W.R. SEARS, "On the instability of small gas bubbles moving uniformly in various liquids," *J. Fluid Mech.* 3, 27-47 (1957).

9. S.S. SADHAL and R.E. JOHNSON, "Stokes flow past bubbles and drops partially coated with thin films. Part 1. Stagnant cap of surfactant film - exact solution," *J. Fluid Mech.* 126 , 237-250 (1983).

10. H.A. STONE and L.G. LEAL, "The effects of surfactants on drop deformation and breakup," *J. Fluid Mech.* 220, 161-186 (1990).

11. R. PAN, C. MALDARELLI, B. ENNIS, and J. GREEN, "Mixed diffusive-kinetic control in the adsorption of the polyethoxylated surfactant $C_{12}E_6$ to the clean air/water interface," (submitted for publication, 1994).

12. G. SUBRAMANIAN and C. TIEN, "Longitudinal mixing in liquid columns due to bubble motion," Syracuse University, Final Report to Federal Water Pollution Control Administration for Grant No. WP 00922 (1970).

13. D.W. MOORE, "The rise of a gas bubble in a viscous liquid," *J. Fluid Mech.* 16, 113-130 (1963).

14. D.W. MOORE, "The velocity of rise of distorted gas bubbles in a liquid of small viscosity," *J. Fluid Mech.* 23, 749-766 (1965).

STRUCTURE AND MODELING OF TURBULENCE

E.A. Novikov

Institute for Nonlinear Science
University of California, San Diego
La Jolla, CA 92093-0402

ABSTRACT

The "vortex strings" scale $\ell_s \sim LRe^{-3/10}$ (L-external scale, Re - Reynolds number) is suggested as a grid scale for the large-eddy simulation. Various aspects of the structure of turbulence and subgrid modeling are described in terms of conditional averaging, Markov processes with dependent increments and infinitely divisible distributions.

The major request from the energy, naval, aerospace and environmental engineering communities to the theory of turbulence is to reduce the enormous number of degrees of freedom in turbulent flows to a level manageable by computer simulations. The vast majority of these degrees of freedom is in the small-scale motion. The study of the structure of turbulence provides a basis for subgrid-scale (SGS) models, which are necessary for the large-eddy simulations (LES). The general strategy, developed in this work is summarized in the Diagram.

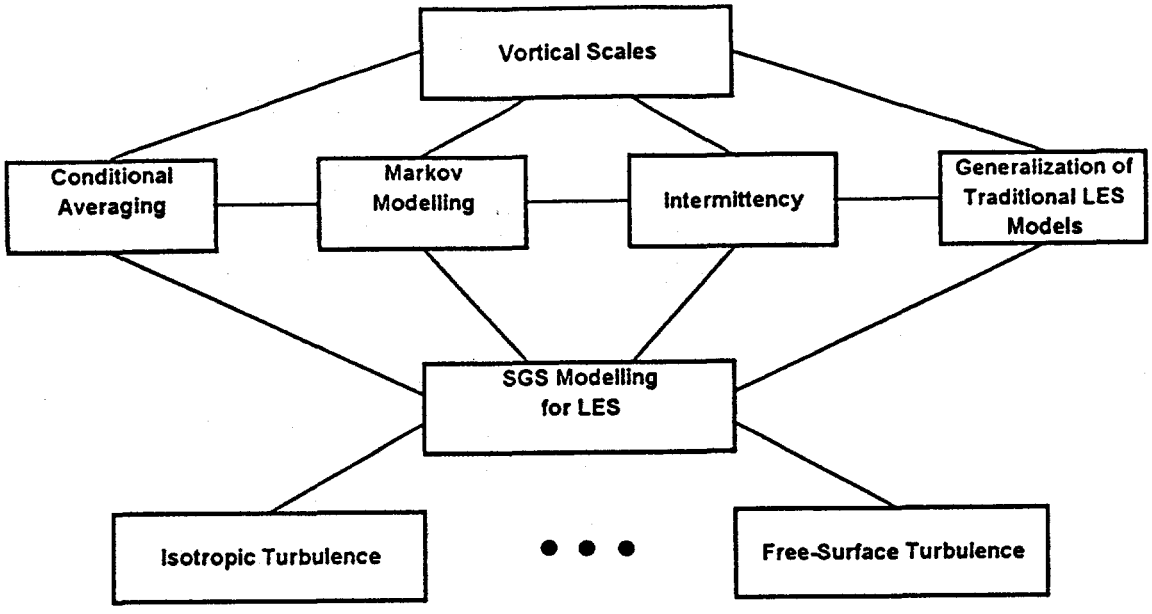

Diagram: Structure and Modeling of Turbulence

The first block in the Diagram ("vortical scales") is about an interface between numerics and a model. It seems natural to choose a grid scale for LES to be of the order of the "vortex strings" scale[1] $\ell_s \sim LR^{-3/10}$ (L-external scale, $Re = VL\nu^{-1}$ - Reynolds number, V - characteristic velocity, ν - molecular viscosity). At this scale, the most important (physically and numerically) nonlinear effect of vortex stretching in three-dimensional (3D) turbulence does not produce a flux in the vorticity correlations. Thus, we expect a smooth connection between numerics and modeling at this scale. The effective number of degrees of freedom with such grid scale is $N_s \sim (L/\ell_s)^3 \sim Re^{9/10}$. A potential reduction in the numerical capacity is huge if we compare N_s with the classical estimate[2] $N \sim Re^{9/4}$, based on the Kolmogorov internal scale $\ell_\nu = \nu^{3/4}\epsilon^{-1/4}$ (ϵ - mean rate of the energy dissipation).

Next in the Diagram is a horizontal row of four blocks, representing various aspects of the statistical structure of turbulence and ingredients of SGS modeling. The first block in this row refers to the conditional averaging of the Navier-Stokes equations with fixed vorticity in a point (for 3D flow). It was analytically predicted[3-5] that for high Re the effect of vortex stretching is statistically balanced with viscous dissipation on any level of fixed vorticity ω and other terms in the vorticity balance are $\sim Re^{-1/2}$. This prediction was recently confirmed by direct numerical simulations (DNS)[6], which also revealed that the conditionally averaged rates of vortex stretching and dissipation increase exponentially with ω. It was also predicted[3-5] and recently confirmed by DNS[7] that conditionally averaged vorticity field $\overline{\mathbf{\Omega}}(\mathbf{r},\omega)$, as a function of distance $\mathbf{r}$ from a point with fixed vorticity ω, has a characteristic twist of vortex lines, connected with the effect of vortex stretching. It was also argued[6] that local imbalance between vortex stretching and dissipation leads to the formation and destruction of twisted vortex strings with characteristic scale ℓ_s indicated above. Having the field $\overline{\mathbf{\Omega}}$, we can construct a relaxation scheme[8], which will make vorticity on a grid in LES to be consistent with $\overline{\mathbf{\Omega}}$. We plan to test such a scheme in the near future.

Let us note, that instead of vorticity we can use microcirculations (velocity circulations over infinitely small fluid contours), which are inviscid invariants of motion. Such approach separates the effect of vortex stretching into an additional linear equation (for fluid surface elements) with independent initial condition[9]. Conditional averaging was also applied to the free-surface turbulence[10] with the use of the fully nonlinear dynamical boundary condition on free surface.

The second block in the same row in the Diagram refers to the Lagrangian and Eulerian description of velocity increments in terms of Markov processes with dependent increments, consistent with the Navier-Stokes equations[11-14]. The 3D vector of velocity increments (vi) can be presented in the form:

$$u_i = v_i(\mathbf{x}+\mathbf{r}) - v_i(\mathbf{x}) = u_r n_i + \tilde{u}_i, \qquad n_i = r_i r^{-1} \tag{1}$$

Here $u_r = u_i n_i$ is the radial (longitudinal) component of vi, $\tilde{u}_i$ is the transversal vi, normal to the separation distance $\mathbf{r}$. In the inertial range ($\ell_\nu \ll r \ll L$) we have the Kolmogorov result:

$$< u_r^2 >= -\frac{4}{5}\epsilon r \tag{2}$$

which can be written in tensor form[11]:

$$< u_i u_j u_k >= -\frac{4}{15}\epsilon(r_i\delta_{jk} + r_j\delta_{ki} + r_k\delta_{ij}) \tag{3}$$

Here $< >$ means statistical (unconditional) averaging. The Kolmogorov result (2) has been originally obtained for decaying turbulence. The same result was derived[15], by using

a special functional formalism[15,16], for statistically stationary turbulence with large-scale random forces, supplying energy. This formalism was also used in the derivation of the balance equation for the vorticity correlations[1] leading to the indicated above scale ℓ_s.

Two components of *vi* are physically different, even simply because of incompressibility condition:

$$\frac{\partial}{\partial r_i} < u_i u_j >= 0 \tag{4}$$

Loosely speaking u_r and $\tilde{u}_i$ signify correspondingly deformation along the vector **r** and rotation around a vector, normal to **r**. Statistical preference of negative u_r, emphasized by (2), corresponds to compression of fluid element in the direction of **r** and (because of incompressibility) expansion in a normal direction. Since $\tilde{u}_i$ represents vortex, oriented normally to **r** , we can interpret (2) as an inertial range manifestation of the same effect of vortex stretching, which is analyzed by conditional averaging (see above). Probability density function (*pdf*) for the vector *vi* has unusual form[13,14]. Asymptotically (when $u^2 \gg < u^2 >$) it reduces to the function of peculiar argument:

$$P(u_r u_i, r) = (\epsilon r \tilde{u})^{-3/4} f\left[\frac{u_r^2 + \tilde{u}^2}{(\epsilon r \tilde{u})^{1/2}}\right] \tag{5}$$

$$\tilde{u}^2 \equiv \tilde{u}_i^2, \qquad f(z) = N_{\pm}^{-1} \exp\{-\theta_{\pm} z^{2/3}\} \tag{6}$$

Here constants N and θ are different for the cases $u_r > 0$ and $u_r < 0$, which is reflected by subscript $\pm$. This asymptotic was obtained[13] without Markovian assumption and corresponds to experimentally observed exponential behavior of *pdf* for u_r. The global *pdf* for the vector *vi* is obtained[13,14] assuming that relative velocity of fluid particles is Markovian with a local relaxation and simplest forcing (diffusion in the velocity space). The Markovian assumption is consistent with (3)-(6) and with the classical similarity. It also gives the Lagrangian description of turbulence[11–14], which corresponds, in particular, to the Richardson law:

$$< r^2(t) >_L \sim \epsilon t^2 \tag{7}$$

Here $r(t)$ is the distance between two fluid particles and subscript L indicates the Lagrangian ensemble of averaging. The exact relations between Lagrangian and Eulerian descriptions[17,18] are used in this approach.

Preliminary LES tests of a Markov type SGS model give positive results. However, intermittency effects, which are important physically and numerically, have to be included into SGS modeling. This leads to the next block in the same row in the Diagram. The intermittency is described in terms of the breakdown coefficients (*bdc*) for the energy dissipation[19,12,20]. The most recent progress is associated with the imbedding of self-similar intermittency into the theory of infinitely divisible distributions[20]. This gives us access to the well developed mathematical apparatus[21]. An intermittency correction in terms of *bdc* for a simple SGS model was obtained in Ref. [12]. For the comparison with the experiment we use data sets, obtained from the big Russian wind tunnel[22], and plan to use data sets from atmospheric boundary layer.

The last block in the same row in the Diagram refers to traditional SGS models (Smagorinsky[23], Bardina[24]) and their broad generalization[25,26].

All models are coming into a melting pot - block "SGS modeling for LES", which serves as a "free market" for SGS models. Here we use the test-filtering procedure (running LES with two different resolutions) in order to determine dynamically weighing coefficients to all models and to find optimal combinations of models for different applications. These

applications, represented in the last row in the Diagram, range from the simplest (isotropic turbulence) to the most complex (free-surface turbulent flows with fully nonlinear dynamical conditions on free surface).

Each of these blocks in the Diagram is an independent and fruitful area of research. By putting them together and focusing on LES implementation, we can see new connections and a more general picture of the structure and modeling of turbulence is developing.

ACKNOWLEDGEMENT

This work is supported by the U.S. Department of Energy under Grant No. DE-FG03-91ER13188, with Dr. Oscar P. Manley as program manager.

REFERENCES

1. E.A. NOVIKOV, *Phys. Rev. Let.* **71**, 2718 (1993).
2. L.D. LANDAU and E.M. LIFSHITZ, "*Fluid Mechanics*", Pergamon, 1959.
3. E.A. NOVIKOV, *Dokl. Akad. Nauk SSSR* **12**, 299 (1967) [*Sov. Phys. Dokl.* **12**, 1006 (1968)].
4. E.A. NOVIKOV, in Proc. of Monte-Verita Sympos. "New Approaches and Concepts in Turbulence" 1991, ed. T. Dracos and A. Tsinober (Birkauser, Basel, 1993); *J. Phys. A* **25**, L657 (1992).
5. E.A. NOVIKOV, *Fluid Dyn. Res.* **12**, 107 (1993); *Phys. Rev. E* **49**(2), R975 (1994); *J. Phys. A.* **27**, L797 (1994).
6. E.A. NOVIKOV and D.G. DOMMERMUTH, *Modern Phys. Lett. B* **8**(23), 1395 (1994).
7. D.G. DOMMERMUTH, R.C.Y. MUI and E.A. NOVIKOV, "Conditionally averaged vorticity field", in preparation.
8. E.A. NOVIKOV, "Conditionally averaged dynamics of turbulence, new scaling and stochastic modeling", in "Lévy Flights and Related Phenomena in Physics" (eds. U. Frish, B. Mandelbrot, M. Shlesinger and G. Zaslavsky), Springer, 1995, to be published.
9. E.A. NOVIKOV, "Microcirculations in Turbulent Flows", submitted to *Phys. Rev. E.*
10. E.A. NOVIKOV, "Conditional averaging of turbulent free surface", submitted to *Phys. Rev. E.*
11. E.A. NOVIKOV, *Phys. Fluids A* **1**, 326 (1989).
12. E.A. NOVIKOV, *Phys. Fluids A* **2**, 814 (1990).
13. E.A. NOVIKOV, *Phys. Rev. A* **46**(10), R6147 (1992).
14. G. PEDRIZZETTI and E.A. NOVIKOV, *J. Fluid Mech.* **280**, 69 (1994).

15. E.A. NOVIKOV, *Zh. Eksp. Teor. Fiz* **47**, 1919 (1964) [*Sov. Phys. JETP* **20**, 1290 (1965)].

16. W.D. McCOMB, "The Physics of Fluid Turbulence", Appendix H (Claredon, Oxford, 1990).

17. E.A. NOVIKOV, *Appl. Math. Mech* **33**, 862 (1969).

18. E.A. NOVIKOV, *Phys. Fluids* **29**, 3907 (1986).

19. E.A. NOVIKOV, *Appl. Math. Mech.* **35**, 231 (1971).

20. E.A. NOVIKOV, *Phys. Rev. E* **50**(5), R3303 (1994).

21. W. FELLER, "An Introduction to Probability Theory and its Applications" (Wiley, New York, 1991, reprinted from 1966 edition) Vol. 2.

22. A.A. PRASKOVSKY, private communication.

23. J. SMAGORINSKY, *Mon. Weather Rev.* **91**, 99 (1963).

24. J. BARDINA, J.H. FERZIGER and W.C. REYNOLDS, AIAA 80-1357 (1980).

25. T.S. LUND and E.A. NOVIKOV, *Ann. Res.*, CTR, Stanford, 27 (1992).

26. D.G. DOMMERMUTH and E.A. NOVIKOV, "Direct-numerical and large-eddy simulations of turbulent free-surface flows", Proc. Sixth Internat. Conf. on Numerical Ship Hydrodynamics, Iowa City, p. 239-270 (1993).

CONTAMINANT DISPERSAL IN BOUNDED TURBULENT SHEAR FLOW

James M. Wallace, Peter S. Bernard, Kwo-Fu Chiang & Lawrence Ong

Department of Mechanical Engineering
University of Maryland, College Park, MD 20742, U.S.A.

ABSTRACT

The dispersion of smoke downstream of a line source at the wall and at $y^+ = 30$ in a turbulent boundary layer has been predicted with a non-local model of the scalar fluxes, $\overline{uc}$ and $\overline{vc}$. The predicted plume from the wall source has been compared to high Schmidt number experimental measurements using a combination of hot-wire anemometry to obtain velocity component data synchronously with concentration data obtained optically. The predicted plumes from the source at $y^+ = 30$ and at the wall also have been compared to a low Schmidt number direct numerical simulation . Near the source, the non-local flux models give considerably better predictions than models which account solely for mean gradient transport. At a sufficient distance downstream the gradient models gives reasonably good predictions.

INTRODUCTION

The prediction of thermal and mass concentration fields diffusing within turbulent shear flows is of paramount importance in numerous applications in environmental science and engineering. Current prediction methods are mainly confined to simple Gaussian diffusion models [1], solutions of the Reynolds averaged equations for which the turbulent scalar flux rate must be modeled [2-4] and to random flight models which mimic the motion of individual tracers in turbulence through an assumed Markov process [5-8]. Closure models for the scalar flux correlation usually have adopted the gradient form in the absence of better knowledge about the physics of scalar transport, although it has long been recognized [9-11] that gradient transport is incapable of representing the short time dispersion near the source of contaminant plumes.

While many tests of the predictions of random flight and closure models have been made against experimental data, until recently [12-17] such comparisons have not been in controlled settings where accurate information about the turbulence scales and other correlations appearing in the models are available. As a result, it has been difficult to discern what the relative strengths of the two methodologies are, and especially whether the substantially greater computational cost of random flight methods in comparison to closure models pays off by providing greater accuracy in the prediction of the near field of scalar dispersal.

Past work of our research group [17] has provided a successful analysis of some important aspects of the physical mechanisms associated with the scalar flux in the near field of plumes. This uses a Lagrangian technique which had heretofore been instrumental in exploring the mechanisms of Reynolds stress and vorticity transport [18 - 20]. Among the accomplishments of this work was a demonstration that the turbulent flux in the near field of plumes is due to meandering of the turbulent field over the source, a physical process bearing no relationship to gradient diffusion. It was also shown, however, that gradient transport physics does emerge at locations far enough downstream of the source. Extensive tests of closure models versus random flight models were made for the case of Prandtl number 0.71 in which a direct numerical simulation (DNS) of the plume flow was used to supply an accurate solution. These tests showed the closure models to be

generally superior to the random flight approach both in speed and accuracy, though serious errors near the source were apparent due to the inappropriateness of the gradient model.

A new non-local turbulent transport theory has been derived as an outgrowth of the previous formal Lagrangian analysis of transport using ensembles of backward particle paths [21]. This is based on replacing ensemble averaging by spatial averaging over the initial locations of the fluid particles. The probability density function (*pdf*) of initial particle position – which plays a critical role in the theory – is derived heuristically and shown to be in good agreement with available data. Applications of the approach to the scalar field in a fully developed channel flow with a uniform source and to a spanwise line source plume, show the non-local formulation to offer some considerable improvements over gradient transport models.

We have carried out closely coordinated experimental, numerical and modeling studies of diffusion of near wall plumes. The inherent restriction of DNS to low Prandtl (or Schmidt) number plumes in relatively simple geometries at low Reynolds numbers places a high premium on well designed experiments to guide the development and testing of scalar transport models suitable for realistic complex flow conditions. For this purpose we have experimentally obtained the mean scalar concentration and concentration fluxes in plumes resulting from a spanwise line source of scalar smoke particles originating at the wall of a turbulent boundary layer. Comparisons for high Schmidt numbers, when combined with the $Pr = 0.71$ number model comparisons and evaluations with the DNS, give a fairly complete picture of the capabilities of current models under a significant range of shear flow conditions. Our analysis of the near source plume diffusion indicates how models need to be formulated to acquire a greater measure of physical accuracy. Implementation and testing of one such model, using experimental data as the essential and final arbiter for determining physical appropriateness, forms the main thrust of this paper.

EXPERIMENTAL FACILITY, INSTRUMENTATION AND METHOD

Experiments (cf.[22-23]) have been carried out in a turbulent boundary layer at $R_\tau \approx 725$ ($R_\theta \approx 1600$) in which smoke was seeped into the sublayer through a downstream facing slot at a location 7 m downstream of the boundary layer trip. The smoke, formed by smoldering incense, was passed through steel wool to remove the tar and then through a heat exchanger to bring it to the temperature of the flow. The smoke generation can be maintained in an equilibrium state for up to two hours and can be reproduced from experiment to experiment. The particle sizes ranged in diameter from $0.12 - 1.92$ μm, and thus follow the flow quite well. Care has been taken to control the smoke injection from the slot so as not to create a wall jet.

In oder to obtain concentration flux values, the U (streamwise, x-direction) and V (wall normal, y-direction) velocity components were measured with a calibrated 4-sensor hot-wire probe, which accounted for binormal cooling of the sensors. It was positioned in a sheet of laser light, oriented in the $x - y$ plane, which illuminates the dispersing scalar smoke particles. In order to create this light sheet, the beam from a 15 W copper-vapor pulsed laser was passed through a set of spherical and cylindrical lenses to form an approximately 1mm thick sheet. The illuminated smoke was photographed on Kodak TMAX instrumentation film (ASA 400 and resolution of 400 lines/mm) with a high speed Photonec 16 mm movie camera during the acquisition of synchronized hot-wire data. These photographs constitute an ensemble of images with light intensities which were subsequently mapped into quantitative values of scalar concentration by means of a calibration and transformation procedure, described below. Averaging over the ensemble yielded contours of mean concentration in the plane of illumination; the averaged products of the instantaneous velocity fluctuations, u and v, with the instantaneous concentration fluctuation values yielded the scalar fluxes.

The images recorded on film were digitized with a personal computer controlled image acquisition system, which consist of a Reticon 8 bit (256 grey levels), 2048 pixel line scanning camera and a motorized film transport device. The averaged digitized image was contrast-enhanced to maximize the range of usable grey levels. Particle sampling was carried out isokinetically at several locations above the wall. The grey level intensities from the images were calibrated against the measured number density of the smoke particles, sorted by particle size with a Laser Aerosol Spectrometer, over a matrix of locations for the same flow and particle emission conditions. The dependence of the light intensity on particle diameter, d, was accounted for by determining an effective number density, N_{eff}, for an arbitrarily chosen particle size (from within the size range), that would scatter

(4) which accounts for any systematic relationship between the velocity field and alterations to C along particle paths. These changes may occur either by diffusion or by the presence of sources in the flow.

Equation (4) may be made the basis for a physically consistent transport model by replacing the ensemble averages by averages over initial particle location. A detailed account of this methodology may be found in [21]. Here, some of the principal ideas are summarized together with numerical results. First, the theory appropriate to a uniform constant source of strength $2/R_eS_c$ is briefly discussed; to be followed by consideration of plume flows. For the wall normal flux in a channel flow (4) gives

$$\overline{vc}(y) = \overline{v_a(\overline{C}_b - \overline{C}_a)} + \overline{v_a(C_a - C_b)}. \tag{5}$$

The formal Lagrangian expansion

$$v_a = v_b + (\overline{V}_b - \overline{V}_a) + (V_a - V_b), \tag{6}$$

to which may be added the natural approximation

$$v_b \approx \frac{y - y'}{T_{22}}, \tag{7}$$

where y' denotes the y coordinate of the particle at b and T_{22} is a Lagrangian integral time scale, provides a basis for modeling v_a in (5). For channel flow $\overline{V}_b - \overline{V}_a = 0$ while the fluid particle acceleration can be modeled as

$$V_a - V_b = -T_{22}\frac{\partial \overline{P}^*}{\partial y}, \tag{8}$$

where the asterisk is meant to denote an average between y' and y. Similarly, the approximation

$$C_a - C_b = \frac{T_{22}}{R_eS_c}\left(\frac{d^2\overline{C}^*}{dy^2} + 2\right) \tag{9}$$

may be developed.

Now substituting volume averages over the initial locations of the fluid particles for the ensemble averages in (5), and using (6 - 9) it follows that

$$\overline{v_a(\overline{C}_b - \overline{C}_a)}(y) = -\int_0^h \frac{y' - y}{T_{22}}(\overline{C}(y') - \overline{C}(y))p(y', y)dy' - T_{22}\int_0^h (\overline{C}(y') - \overline{C}(y))\,\frac{\partial \overline{P}^*}{\partial y}\,p(y', y)\,dy', \tag{10}$$

and

$$\overline{v_a(C_a - C_b)} = -\int \frac{y' - y}{R_eS_c}\,\frac{d^2\overline{C}^*}{dy^2}\,p(y', y)\,dy' - \int \frac{\partial \overline{P}^*}{\partial y}\,\frac{T_{22}^2}{R_eS_c}\left(\frac{d^2\overline{C}^*}{dy^2} + 2\right), \tag{11}$$

where h is the channel height and $p(y', y)$ is the *pdf* for the chance that a fluid particle originating at y' travels to y over a mixing time. In each of the terms in (10), the identity $\overline{C}_b - \overline{C}_a = \overline{C}(y') - \overline{C}(y)$ is used.

Equations (10) and (11) are useful once an explicit formula for $p(y', y)$ is provided. If it is assumed that the *pdf* of v at any point in a flow is Gaussian, then it may be shown heuristically that

$$p(y', y) = \frac{1}{\sqrt{2\pi}l_2}e^{-\frac{(y'-y)^2}{2(l_2)^2}} \tag{12}$$

where $l_2 \equiv \sqrt{\overline{v^2}T_{22}}$. This equation is exact for the case of a linear distribution of $\overline{C}$ in homogeneous turbulence.

Near boundaries it can be expected that the *pdf* of v departs from Gaussianity, so some modification to (12) is necessary near solid walls. For a fixed wall at $y = 0$, $p(y', y) = 0$ for $y' = 0$,

the same amount of light as the poly-sized particle cloud:

$$I \propto \sum d_i^2 N_i = d_{eff}^2 N_{eff}, \tag{1}$$

where I is the average grey-level intensity at the corresponding concentration measurement location. Thus at each node of the calibration matrix,

$$N_{eff} = \left(\frac{d_i}{d_{eff}}\right)^2 N_i. \tag{2}$$

When this effective number density is plotted against the average light intensity, as shown in Fig. 1, a linear calibration relationship between these two variables is obtained. With this relationship, the grey level intensities in each instantaneous image were converted to effective concentration values. The value of the particle flux was determined across the vertical plane at $x^+ = 95$, and this value was used to set the release rate of the source term in the model, to be described below.

NUMERICAL SIMULATION AND MODELING

To analyze the physics of transport, ensembles of backward particle paths were obtained from a direct numerical simulation of a line source plume developing in turbulent channel flow. The paths were computed from a large set of previously computed and stored consecutive numerical velocity fields. The simulation [17] has a mesh with $96 \times 97 \times 96$ points in the streamwise, wall-normal and spanwise directions, respectively, and a computational box of dimensions $1822 \times 290 \times 683$, expressed in wall units. The numerical scheme consists of a pseudo-spectral method to solve the full incompressible 3D Navier-Stokes equations. The velocity and scalars on off nodal points needed in the path computations are obtained through tricubic interpolation [24]. The Reynolds number of the simulation is $R_\tau = U_\tau h/\nu = 145$, where U_τ is the friction velocity and h is the channel halfwidth. The mean velocity and Reynolds stresses for the simulation agree closely with those found in previous studies [25]. In a further test of the code, a spatially uniform source flow was computed and shown to agree very closely with previous simulations [12,13].

We have attempted to develop a physically accurate model of scalar transport using a Lagrangian decomposition of the scalar flux correlation, $\overline{u_i c}$, into identifiable physical processes. This correlation appears naturally in the averaged scalar transport equation

$$\frac{\partial \overline{C}}{\partial t} + \overline{U}_i \frac{\partial \overline{C}}{\partial x_i} = -\frac{\partial \overline{u_i c}}{\partial x_i} + \frac{1}{ReSc} \nabla^2 \overline{C} + Q, \tag{3}$$

where C is the concentration field, $\overline{C}$ and c are its mean and fluctuating parts with overbars denoting ensemble averaging, u_i is the velocity fluctuation vector, $\overline{U}_i$ is the mean velocity vector and Q is a source term for the scalar. The basis for the model described below is the identity

$$\overline{u_{i_a} c_a} = \overline{u_{i_a} c_b} + \overline{u_{i_a}(\overline{C}_b - \overline{C}_a)} + \overline{u_{i_a}(C_a, -C_b)}, \tag{4}$$

where the subscript a refers to the given endpoint of a large ensemble of fluid particle paths at time t which are at the random locations b at an earlier time $t - \tau$. As discussed elsewhere in related contexts and verified numerically [17-20], the mixing condition $\overline{u_{i_a} c_b} = 0$ is satisfied for τ large enough. We define the mixing time, say τ_m, as the smallest interval at which $\overline{u_{i_a} c_b} \approx 0$. τ_m may be thought of as the time over which events in the flow cause the correlation between u_i and c to develop. Equation (4) thus shows that for times $\tau > \tau_m$, $\overline{u_i c}$ is a result of the processes represented by the last two terms.

The second term on the right-hand side of (4) represents transport arising from the displacement of fluid particles. It is a formal statement of the classical argument that in the presence of a gradient in the mean scalar field, turbulent eddying motion should lead to a net transport. In particular, the resulting directional dependence of the scalar flux on the gradient of $\overline{C}$ is created by fluid particles carrying on average – without alteration – the local mean scalar field of their starting point to their final point over a mixing time. Non-gradient sources of transport are contained in the last term in

since fluid particles on the surface have no chance of migrating to interior points in the flow. A convenient means of enforcing this condition is to generalize (12) via

$$p(y',y) = \frac{1}{\sqrt{2\pi}l_2^*}\left(e^{-\frac{(y'-y)^2}{2(l_2^*)^2}} - e^{-\frac{(y'+y)^2}{2(l_2^*)^2}}\right) \tag{13}$$

where $l_2^* = \min\{l_2, y/3\sqrt{2}\}$, a condition assuring that $\int_0^h p(y',y)dy' \approx 1$ for y near the boundary. Numerical computations show that l_2^* slightly deviates from l_2 only in the region $y^+ \leq 25$.

Despite the heuristic derivation of (13), its general validity is supported by comparisons with measurements of $p(y',y)$ obtained in a turbulent channel flow. Fig. 2 shows predictions of $p(y',y)$ at $y^+ = 7.4$ and $y^+ = 36.6$ obtained from a direct numerical simulation compared to (13). It is clear that the latter gives a reasonable estimate of $p(y',y)$ including an excellent prediction of the scale of its support. The model curves do not show the effect of the boundary to the same degree as the DNS results, suggesting that (13) does not sufficiently take into account the departure of the *pdf* of v from Gaussianity near the wall. On the whole, however, (13) provides a sufficiently accurate description to make a useful implementation of the theory.

Application of (5) and equivalent formulas for $\overline{uc}$ give excellent predictions of channel flow containing a uniform source as shown in [21]. It was found that the first term in (10) is a dominant effect in wall normal transport and may be used by itself to most efficiently capture the important physics for predictive schemes. Now we concentrate on an extension of the method suitable for two-dimensional plumes. In this case, previous work [17] showed that the physics of transport along a plume is distinctly different near and far from the source. In the former case, transport is primarily due to the effect captured in the last term in (5), which represents fluid particles picking up the scalar as they meander through the source. Away from the source the physics are well accounted for by the first term in (10). Proceeding formally, we have that near the source the most important effect is

$$\overline{v_a(C_a - C_b)} = -\int \frac{y'-y}{T_{22}}\left(\int_{-T_{22}}^{0} Q(s)ds\right)\, p(\mathbf{x}',\mathbf{x})d\mathbf{x}' \tag{14}$$

where $\int Q(s)ds$ is the amount of scalar acquired by a fluid particle arriving at a given point $\mathbf{x}$ after leaving from $\mathbf{x}'$. Note that for constant Q, this term is zero, which is why it does not appear in (11). An estimate of $\int Q(s)ds$ for fluid particles traveling from $\mathbf{x}'$ to $\mathbf{x}$ must be found if (14) is to be evaluated. Here it will be assumed that the only paths for which $\int Q(s)ds \neq 0$ are those for which the source lies between $\mathbf{x}'$ and $\mathbf{x}$, i.e. $\mathbf{x}'$ lies in the 'shadow' behind the source as viewed from $\mathbf{x}$ (see Fig. 2). Thus, every fluid particle leaving from the region contained within the dashed line in the figure and arriving at $\mathbf{x}$ after a mixing time is assumed to pass over the source, while no others do so. This probabilistic model is consistent with the approximations such as (7) and our intuitive sense of where the particles most likely to cross the source come from.

To evaluate (14), the source region is discretized into small sections represented by the grid as shown in Fig. 3. For each of these, such as the one which is dark shaded, it is assumed that all fluid particles starting out in the region contained in the dashed outline will pass through this part of the source and thus have a non-zero value of $\int Q(s)ds$. The amount of $\int Q(s)ds$ can be estimated as the local magnitude of the source in a particular area, say Q_{ij} for the i,jth box, times the time it takes the fluid particle to cross it, say τ. The latter may be estimated as the characteristic dimension of the grid spacing Δx divided by the speed at which the fluid particle passes over this area. The estimate may then be made:

$$\int Q(s)ds = Q_{ij} \times \frac{\Delta x}{\sqrt{(x-x')^2 + (y-y')^2}/\tau} \tag{15}$$

The width of the dashed region behind the source element is given by the small number Δx, so that after substitution of (15) into (14), it is justifiable to collapse the area integral in (14) to just a line integral along the length of the shadow region in Fig. 3. Collecting these results together gives

$$\overline{vc}(y) = - \int \frac{y'-y}{T_{22}} (\overline{C}(\mathbf{x}') - \overline{C}(\mathbf{x})) p(\mathbf{x}', \mathbf{x}) d\mathbf{x}'$$

$$- \sum_{ij} \frac{Q^*_{ij} Y_{ij}}{2\pi l_1 \sqrt{1-\rho^2} R_{ij}} \int_{-\infty}^{-R_{ij}} da \, e^{-\frac{a^2 Y_{ij}^2}{2R_{ij}^2} - \frac{\left[a\left(\frac{X_{ij}}{R_{ij}} - \rho \frac{Y_{ij}}{R_{ij}}\right) + \overline{X}\right]^2}{2(1-\rho^2)}} \tag{16}$$

where $Q^*_{ij} = Q_{ij} \Delta A_{ij}$, ΔA_{ij} is the area of the (i,j)th source element, $X_{ij} = (x - x_{ij})/l_1$, $Y_{ij} = (y - y_{ij})/l_2$, $R_{ij} = \sqrt{(x-x_{ij})^2 + (y-y_{ij})^2}/l_1$ and $\overline{X} = \overline{U} T_{22}/l_1$.

An equivalent analysis of the streamwise flux may be performed with similar results. The complete non-local closure may be applied to the study of plume flows in a wide variety of circumstances.

RESULTS

Fig. 4 illustrates the improvement over a gradient law which is attainable from (16). Predictions of $\overline{vc}$ are given along the line $y^+ = 43.5$ through a plume centered at $x^+ = 0, y^+ = 30$. Equation (16) shows very good agreement with the DNS while the gradient model is subject to extremely large errors in the vicinity of the source. These only diminish to a reasonable level by $x^+ = 250$, after which point the gradient model appears to be a reasonable approximation. The different roles of the two terms in (16) is shown in Fig. 5. Near the origin of the plume the displacement effect is negligible and transport is entirely due to the source term. Downstream, the situation is reversed as the displacement mechanism begins to dominate transport by $x^+ = 200$. These results are fully consistent with the previous evaluation of (5) using ensembles of particle paths, [17]. It should be noted that the results from the DNS shown here have not been sufficiently averaged to remove some of the obvious statistical variations. This is most true of the gradient curve in Fig. 4 which was evaluated from finite differences of the mean scalar field computed in the DNS.

Contours plots of $\overline{C}$ determined from the gradient model, the DNS and experiment are shown in Fig. 6. Clearly the gradient model does not capture the character of the DNS plume near the source. This is shown even clearer in Fig. 7 where the values of $\overline{C}$ along the wall are plotted. Further downstream the gradient model, the DNS and the experiment are in relatively good agreement. Experimental values of the fluxes $\overline{uc}$ and $\overline{vc}$, were measured; they show the expected trend in sign and magnitude in the buffer layer and in the lower part of the logarithmic layer.

CONCLUSION

A non-local closure for turbulent scalar flux was derived as an extension of a previous Lagrangian transport analysis. Assuming the availability of the appropriate length and time scales of the underlying turbulent flow field, the closure was shown to be effective in capturing many aspects of scalar transport which are erroneously predicted by gradient closures, by comparison to experimental and DNS results.

REFERENCES

1. R. W. BOUBEL, D. FOX, D. TURNER and A. STERN, *Fundamentals of Air Pollution*, 3rd Ed., Academic Press, San Diego (1994).

2. A. YOSHIZAWA, "Statistical modeling of passive scalar diffusion in turbulent shear flows," *J. Fluid Mech.* 195, 541 (1988).

3. M. M. ROGERS, N. N. MANSOUR, and W. C. REYNOLDS, "An algebraic model for the turbulent flux of a passive scalar," *J. Fluid Mech.* 203, 77 (1989).

4. K. HORIUTI (1992), "Assessment of two-equation models of turbulent passive scalar diffusion in channel flow," *J. Fluid Mech.* 238, 405 (1992).

5. H. VAN DOP, F. T. M. NIEUWSTADT, and J. C. R. HUNT, "Random walk models for particle displacements in inhomogeneous unsteady turbulent flows," *Phys. Fluids* 28, 1639 (1985).

6. D. J. THOMSON, "A random walk model of dispersion in turbulent flows and its application to dispersion in a valley," *Quart. J. Roy. Met. Soc.* 112, 511 (1986).

7. Y. SHAO, "Turbulent dispersion in coastal atmospheric boundary layers: an application of a Lagrangian model," *Bound. Layer Met.* 59, 363 (1992).

8. J. M. MACINNES and F. V. BRACCO, "Stochastic particle dispersion modeling and the tracer-particle limit," *Physics Fluids A* 4, 2809 (1992).

9. M. R. RAUPACH, "A practical Lagrangian method for relating scalar concentrations to source distributions in vegetation canopies," *Quart. J. Royal Met. Soc.* 115, 609 (1989).

10. G. I. TAYLOR, "Diffusion by continuous movements," *Proc. London Math. Soc.* Ser. 2, 20, 196 (1921).

11. C. A. DEGRAZIA and O. L. L. MORAES, "A model for eddy diffusivity in a stable boundary layer," *Boundary Layer Met.* 58, 205 (1991).

12. W. C. REYNOLDS, M. M. ROGERS and N. D. Sandham, "Advances in turbulent transport modeling based on direct simulations of turbulence," *Transport Phenomena in Turbulent Flows: Theory, Experiment, and Numerical Simulation*, edited by M. Hirata, N. Kasagi, (Hemisphere, N. Y.), 701 (1988).

13. J. KIM and P. MOIN, "Transport of passive scalars in a turbulent channel flow," in *Turbulent Shear Flows 6*, edited by J.-C. Andre et al., (Springer, N. Y.), 5-2-1 (1987).

14. N. KASAGI and Y. OHTSUBO, "Direct numerical simulation of passive scalar field in a turbulent channel flow," *ASME J. Fluids Engrg.* 114, 598 (1992).

15. P. K. YEUNG, J. G. BRASSEUR and D. M. Bell, "Evolution of passive scalar sources in a numerically simulated boundary layer," in *Near Wall Turbulent Flows*, edited by R. M. C. So, C. G. Speziale and B. E. Launder, (Elsevier, Amsterdam) 307 (1993).

16. D. M. BELL and J. H. FERZIGER, "Turbulent boundary layer DNS with passive scalars," in *Near Wall Turbulent Flows*, edited by R. M. C. So, C. G. Speziale and B. E. Launder, (Elsevier, Amsterdam) 327 (1993).

17. P. S. BERNARD and A. L. ROVELSTAD, "On the physical accuracy of turbulent scalar transport models in inhomogeneous turbulence," *Physics Fluids* 6, 3093 (1993).

18. P. S. BERNARD, "Turbulent Vorticity Transport in Three Dimensions," *Theoretical and Computational Fluid Dynamics*, 2, pp. 165 (1990).

19. P. S. BERNARD and R. A. HANDLER, "Reynolds Stress and the Physics of Turbulent Momentum Transport," *Journal of Fluid Mechanics*, 220, pp. 99 (1990).

20. P. S. BERNARD, J. M. THOMAS and R. A. HANDLER, "Vortex Dynamics and the Production of Reynolds Stress," *J. of Fluid Mechanics*, 253, pp. 385 (1993).

21. P. S. BERNARD, "A Non-local Physically Consistent Turbulent Transport Model," to appear in Proceedings of Turbulent Shear Flows 10, Penn State Univ. (1995).

22. H. STAPOUNTZIS and R. E. BRITTER, "Turbulent diffusion behind a heated line source in a nearly homogeneous turbulent shear", in *Proc. 6th Turbulent Shear Flows 6*, (Springer-Verlag,Berlin), 9.2.1 (1987).

23. U. KARNIK and S. TAVOULARIS,"Measurements of heat diffusion from a continuous line source in a uniformly sheared turbulent flow", *J. Fluid Mech.* 202, 233 (1989).

24. A. L. ROVELSTAD, R. A. HANDLER and P. S. BERNARD, "The Effect of Interpolation Errors on the Lagrangian Analysis of Simulated Turbulent Channel Flow," *J. Computational Physics*, 110, pp. 190 (1994).

25. KIM, J., MOIN, P. and MOSER, R. D., 1987 "Turbulence statistics in fully-developed channel flow at low Reynolds number" *J. Fluid Mech.*, 177 (133).

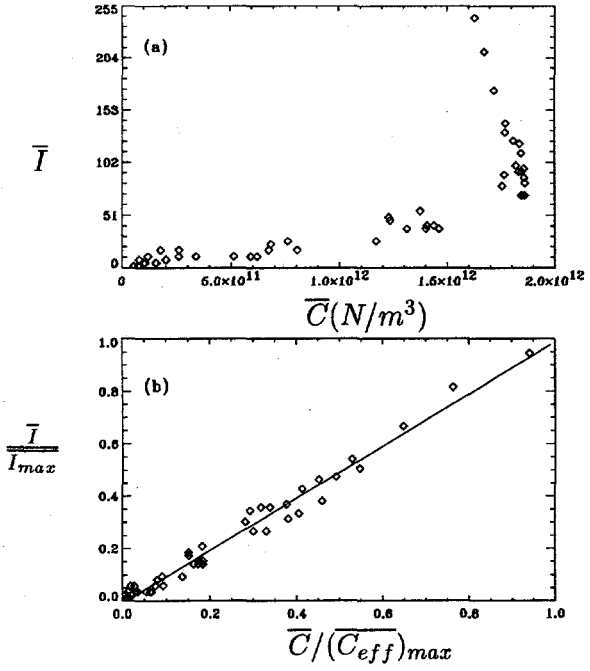

Figure 1: Calibration relationship between (a) the grey level intensity and the raw particle concentration, (b) the grey level intensity and the effective particle concentration.

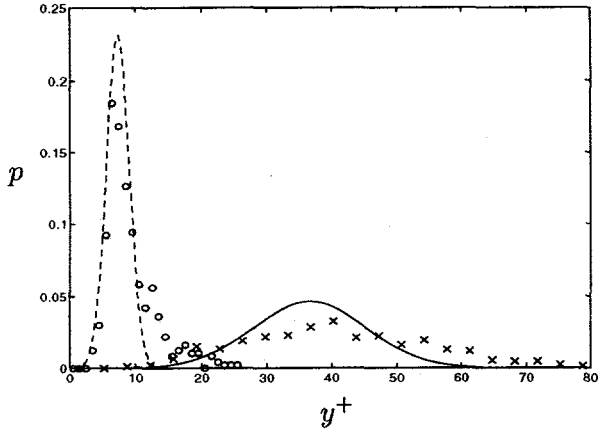

Figure 2: *pdf* of initial particle position. ∘, DNS for $y^+ = 7.4$; ×, DNS for $y^+ = 36.6$; – – –, Eq. (13) for $y^+ = 7.4$; and, ——, Eq. (13) for $y^+ = 36.6$.

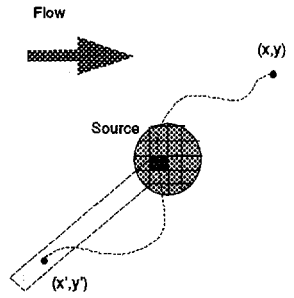

Figure 3: Model of transport due to source.

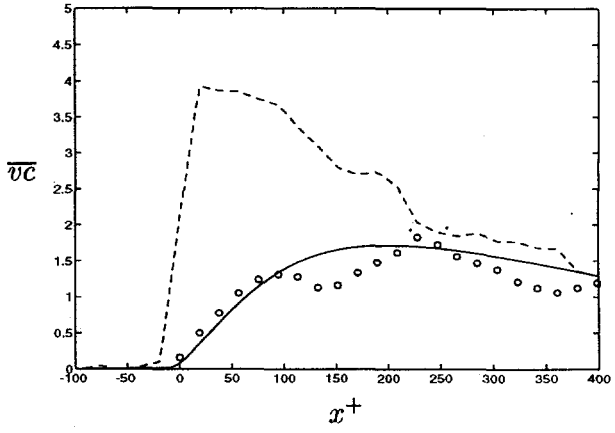

Figure 4: $\overline{vc}$ on line $y^+ = 43.5$: ∘, DNS; ——, Eq. (16); – – –, gradient model.

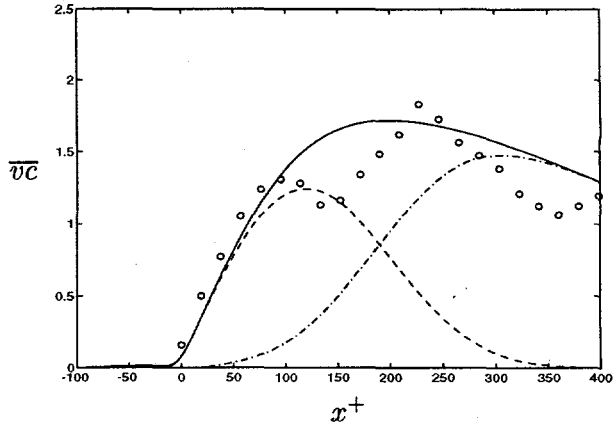

Figure 5: $\overline{vc}$ on line $y^+ = 43.5$: ∘, DNS; ——, Eq. (16); –·–, displacement term in (16); – – –, source term in (16).

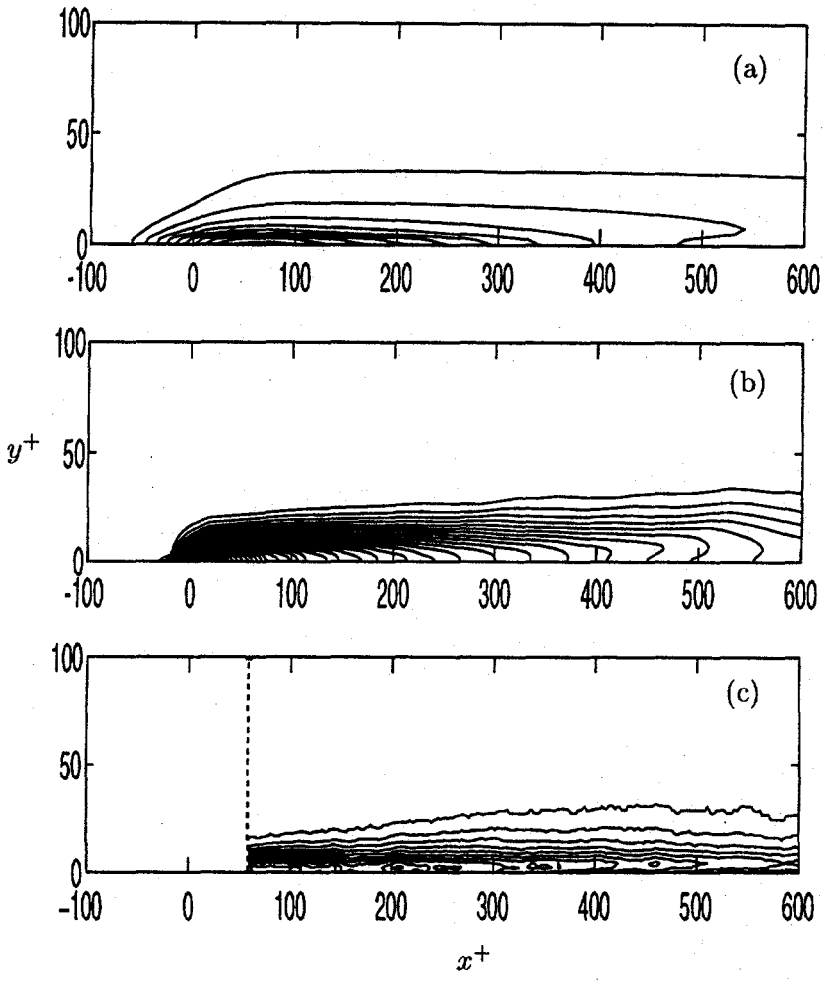

Figure 6: Concentration contours: (a) Gradient model, (b) DNS, (c) Experiment.

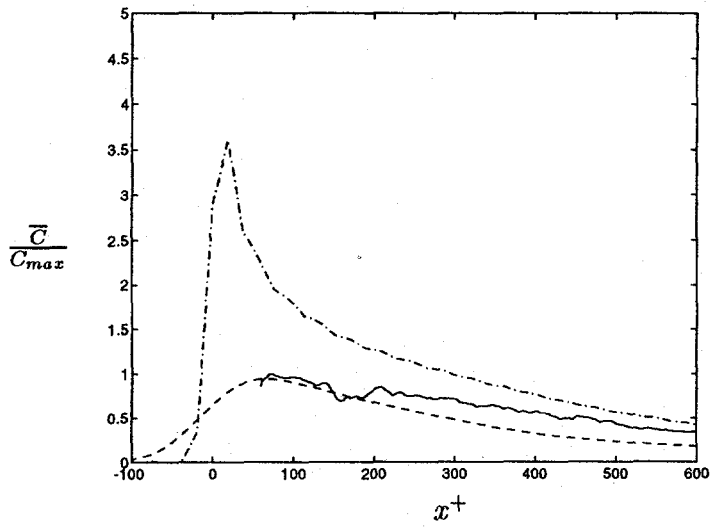

Figure 7: Streamwise concentration profile at $y^+ = 0$: $- \cdot - \cdot -$ DNS, $- - - -$ Gradient model, —— Experiment.

ANOMALOUS SCALING OF A SCALAR FIELD ADVECTED BY TURBULENCE

Robert H. Kraichnan

Robert H. Kraichnan, Inc.
369 Montezuma 108, Santa Fe, NM 87501-2626

ABSTRACT

Recent work leading to deduction of anomalous scaling exponents for the inertial range of an advected passive field from the equations of motion is reviewed. Implications for other turbulence problems are discussed

Understanding of the dynamics of the small scales of turbulence is essential to construction of improved parametrization of small scales in computer modeling of turbulence. It is also an outstanding challenge in non-equilibrium statistical mechanics. For over 50 years, thinking about the small scales of turbulence has been dominated by the cascade ideas first presented by Kolmogorov in 1941 and modified in 1962 to include phenomena associated with intermittency of dissipation [1]. It has long been recognized that the small scales of turbulence are intermittent and that the intermittency of the velocity derivatives increases with Reynolds number. An unsettled question is whether the increase persists to infinite Reynolds number so that the scaling exponents of the inertial-range structure functions at infinite Reynolds number differ from the total self-similarity by Kolmogorov in 1941 (K41) [1].

In the years since 1962, a very large number of models of intermittency in the inertial and dissipation ranges have been proposed and compared with experimental data [1]. In particular, many fractal models of inertial range structure have been offered, some of great sophistication and mathematical complexity. One thing conspicuously missing in almost all of this work is contact with the equations of motion; the models are not derived from the Navier-Stokes (NS) equation. The present paper reviews recent work in which this pattern has been broken in the case of a particular limit of the advection of a passive scalar contaminant field by a random incompressible velocity field. Non-trivial anomalous scaling exponents for the inertial-range structure functions of the scalar field are deduced from the equations of motion [2,3]. The implications of the scalar-field analysis for two other problems, Burgers and NS dynamics, are discussed qualitatively.

Successive random strainings of flow subvolumes containing a passively advected scalar field tend to produce intermittency in the gradient of the scalar field. If there were no counteracting mechanism, the probability distribution function of the scalar gradient would become ever more intermittent as the number of effective independent steps of straining increases. Thus the steady-state intermittency would increase with increase of ratio of macrolength scale to dissipation length scale (increase of Péclet number). A corresponding argument suggests an increase of intermittency

of vorticity with Reynolds number as a result of successive strainings. The increase is compounded by vorticity intensification as vortex tubes are stretched.

What can oppose the increase? One mechanism that can inhibit growth of intermittency is molecular diffusivity/viscosity, which relaxes a non-Gaussian field toward Gaussian statistics. Crudely speaking, this is because unusually strong spikes in the field are preferentially relaxed (spread in space). The same effect can come from the action of eddy diffusivity/viscosity associated with scales smaller than those suffering the relaxation. At a given scale size in an inertial range, the eddy diffusivity/viscosity effects are of the same order as the straining effects that act to increase intermittency. Thus power counting, order-of-magnitude arguments, and associated dimensional considerations, are inadequate to determine whether increase of intermittency with decrease of scale size eventually is halted by the relaxation effects [4].

Eddy relaxation effects characterize both NS dynamics and the advection of a passive scalar field by a stochastic velocity field. They take a degenerate form in Burgers dynamics, where nonlinearity produces shocks that eventually relax without loss of form under the combined action of molecular viscosity and self-advection. Burgers dynamics exhibits extreme intermittency of velocity gradients.

Turbulence may be examined in either the physical space (x space) or wavenumber (k space) domains. There are also hybrid representations, such as by wavelets or by subfields in x space that are band-limited in k space. There are some pitfalls in passing among different representations. In particular, one must be wary of asserting that certain quantities live exclusively in the inertial range.

Isotropic absolute-value structure functions for an isotropic, homogeneous velocity field $\mathbf{u}(\mathbf{x})$ may be defined by

$$S_n^{\mathbf{u}}(r) = \langle |\mathbf{u}(\mathbf{x}+\mathbf{r}) - \mathbf{u}(\mathbf{x})|^n \rangle , \tag{1}$$

where $\langle\ \rangle$ denotes ensemble average. If the inertial-range spectrum of the velocity field is $E(k) \propto k^{-5/3}$, or something near to that form, then there is a close link between description by structure functions and band decomposition: If the statistics are not too exotic, and n is not too large, the value of $S_n^{\mathbf{u}}(r)$ is dominated by contributions from $O(1/r)$ velocity-field wavenumbers. Thus there is justification for linking "scale size" r to a band of wavenumbers k and speaking of "inertial-range scales r".

The concept of a pure inertial-range of r for structure functions is less justified when one turns to dynamics. The equation of motion for $S_n^{\mathbf{u}}(r)$ involves molecular dissipation in an essential way, even when r is in the inertial range [2]. This is easily understood by taking the simplest case of Gaussian $\mathbf{u}(\mathbf{x})$, expanding the right side of (1), and decomposing the average into sums of products of covariances. If r is in middle of a long inertial range, the covariance $\langle \mathbf{u}(\mathbf{x}+r)\cdot\mathbf{u}(\mathbf{x}) \rangle$ decays negligibly from direct molecular dissipation. However, the variance $\langle |\mathbf{u}(\mathbf{x})|^2 \rangle$ also occurs. Its decay rate is finite and independent of r because its spectral support includes the dissipation range of wavenumbers. Molecular viscosity appears directly, and importantly, in the equation of motion for $S_n^{\mathbf{u}}(r)$ at inertial-range r. It should play a central role also in the construction of dynamical models of the inertial-range $S_n^{\mathbf{u}}(r)$.

Suppose that there is a power-law scaling range of r such that

$$S_n^{\mathbf{u}}(r) \propto r^{\zeta_n}, \tag{2}$$

where the exponents ζ_n are independent of r. It is useful to define the terms "regular scaling", "anomalous scaling", and "progressive scaling". Scaling shall be called regular here if $\zeta_n/\zeta_m = n/m$. This corresponds to full similarity of statistics at all r in the range. A more concrete description may be given in terms of the band-limited fields. Suppose that the entire scaling range of $k = 2\pi/r$ is divided into decade bands in wavenumber. Then regular scaling implies that all moments of the x-space velocity field in a band are independent of band location, provided that the moments are

normalized by the variance of the band-limited velocity. Regular scaling corresponds to the K41 picture of the inertial range.

All scaling that is not regular shall be called anomalous here. If the scaling range is infinitely long, and structure functions at macroscales r are finite, Hölder inequalities require $\zeta_n/n \leq \zeta_m/m$ if $n > m$; as n increases, anomalous exponents can only decrease below regular values. Progressive scaling shall denote anomalous scaling in which the exponent differences $\zeta_{n+1} - \zeta_n$ become ever smaller as n increases.

Burgers equation

$$\frac{\partial u}{\partial t} + u\frac{\partial u}{\partial x} = \nu\frac{\partial^2 u}{\partial x^2} \tag{3}$$

evolves the velocity $u(x,t)$ of an infinitely compressible fluid of viscosity ν. Shocks form under (3) as fast-moving fluid overtakes slow-moving fluid. The inertial range at large Reynolds number is asssociated with the neighborhoods of the shocks. The shocks have a characteristic sawtooth shape which represents coherence over a wide range of wavenumbers. Dissipation is concentrated within the shocks and thereby is highly intermittent. The structure functions $S_n^u(r) = \langle |u(x+r) - u(x)|^n \rangle$ for inertial-range r have the form

$$S_n^u(r) = u_0^n r/L, \tag{4}$$

where u_0 is the root-mean-square (rms) velocity and L is a macroscale for velocity fluctuations. The support of $S_n^u(r)$ is dominated by the shocks: r/L in (4) measures the probability that a major shock occurs between $x + r$ and x while u_0 measures the jump in velocity at a major shock.

Equation (4) is an extreme example of anomalous scaling. It is not progressive scaling. The differences $\zeta_{n+1} - \zeta_n$ degenerate to zero and so do not decrease as n increases. The strong intermittency of high-Reynolds-number Burgers flow arises from the shocks, which are structures involving coherence over a wavenumber range that extends from $1/L$ to dissipation wavenumbers. Nevertheless, it is easy to demonstrate that the cascade of energy toward higher wavenumbers is local in the wavenumber space [5]. The straining across a distance r that sharpens the shocks and maintains them in a sharp state is dominated by contributions from wavenumbers $O(1/r)$. Spatial coherence and dynamical locality in wavenumber do not preclude each other.

The scalings of $S_2^u(r)$ and $S_3^u(r)$, features closely associated with existence of shocks, are given correctly by an approximation that is quite incapable of explicit description of shocks or any coherent spatial structures. This is the Lagrangian-history direct-interaction approximation (LHDIA) [5]. The LHDIA uses only limited information from Burgers equation: conservation laws and invariance to Galilean transformations as incorporated in expressions quadratic in the interaction coefficients of individual wavenumber-triad amplitudes. Cross terms between different wavenumber-triad coefficients, which could express phase coherence in physical space, are absent. An implication of the success of this approximation is that relatively elementary properties of the interaction coefficients directly imply the scaling, so that it is possible to recover the latter without being able actually to describe the structures in space. In this picture, the shock structures are regarded not as the cause of the scaling but as a parallel manifestation of an underlying dynamics.

The equation of motion of a passive scalar field $T(\mathbf{x},t)$ advected by an incompressible velocity field $\mathbf{u}(\mathbf{x},t)$ is

$$\left(\frac{\partial}{\partial t} + \mathbf{u}(\mathbf{x},t)\cdot\boldsymbol{\nabla}\right) T(\mathbf{x},t) = \kappa\nabla^2 T(\mathbf{x},t), \tag{5}$$

where κ is molecular diffusivity. The inertial-range structure of T depends on that of $\mathbf{u}$. In order to clarify what causes what, it helps to start with a Gaussian $\mathbf{u}$ field rather than a solution of the NS equation. Maximum simplification occurs when $\mathbf{u}(\mathbf{x},t)$ has a correlation time that is infinitely short compared to any eddy circulation time. This limit yields exact expressions for the effects of

advection on scalar-field statistics [6,7]. It can be approached in such a way that the single-particle and two-particle eddy diffusivities resemble those of more realistic fields.

In the rapid-change limit, the exact evolution equation for the structure functions $S_{2n}^{\mathrm{T}}(r) = \langle |\Delta T(\mathbf{r})|^{2n} \rangle$, where $\Delta T(\mathbf{r})$ denotes $T(\mathbf{x}+\mathbf{r}) - T(\mathbf{x})$, can be derived as

$$\frac{\partial S_{2n}^{\mathrm{T}}(r)}{\partial t} - \frac{2}{r^{d-1}} \frac{\partial}{\partial r} \left(r^{d-1} \eta(r) \frac{\partial S_{2n}^{\mathrm{T}}(r)}{\partial r} \right) = \kappa J_{2n}(r). \tag{6}$$

Here d is space dimensionality, $\eta(r)$ is the two-particle eddy-diffusivity scalar defined by

$$\eta(r) = \frac{1}{2} \int_0^t \langle [\delta_{\parallel} u(\mathbf{r},t) \delta_{\parallel} u(\mathbf{r},t')\rangle \, dt', \tag{7}$$

with $\delta_{\parallel} u(\mathbf{r},t) = [\mathbf{u}(\mathbf{x},t) - \mathbf{u}(\mathbf{x}+\mathbf{r},t)] \cdot \mathbf{r}/r$, and

$$J_{2n}(r) = 2n \left\langle [\Delta T(\mathbf{r})]^{2n-1} (\nabla_x^2 + \nabla_{x'}^2) \Delta T(\mathbf{r}) \right\rangle, \tag{8}$$

is the dissipation term anticipated in the discussion following (1). It is assumed that the velocity field is switched on at $t = 0$ and that $T(\mathbf{x}, t = 0)$ is Gaussian [2].

The difficulties in turbulence theory usually are ascribed to the nonlinearity in stochastic quantities, which poses the so-called closure problem. In the present case, the dynamical effects on $S_{2n}^{\mathrm{T}}(r)$ of the advection term in (5), which contains all the stochastic nonlinearity, are fully and exactly described by the $\eta(r)$ term in (6), so what is usually called the closure problem disappears. However, another kind of closure problem remains: the dissipation term $J_{2n}(r)$ in (6) contains space derivatives in such a way that it cannot be expressed in a closed form that involves only the structure functions. Closed equations can be written for the general $2n$-point, single-time moment of T, but they are much more complicated than (6) [7]. Equations (6)–(8) do form a closed set for $n = 1$.

Despite the lack of closure of (6)–(8), it has been possible to make some progress in deducing the inertial-range scaling exponents from them. A key step is the introduction of the conditional mean

$$H[\Delta T(\mathbf{r})] = \left\langle (\nabla_x^2 + \nabla_{x'}^2) \Delta T(\mathbf{r}) | \Delta T(\mathbf{r}) \right\rangle, \tag{9}$$

where $\langle \cdot | \Delta T(\mathbf{r}) \rangle$ denotes ensemble average conditioned on a given value $\Delta T(\mathbf{r})$. $J_{2n}(r)$ may be written

$$J_{2n}(r) = 2n \left\langle [\Delta T(\mathbf{r})]^{2n-1} H[\Delta T(\mathbf{r})] \right\rangle. \tag{10}$$

It can then be argued persuasively (but not yet rigorously) that there are only two forms for $H[\Delta T(\mathbf{r})]$ that permit steady-state power-law scaling solutions of (6) in the inertial range [3]. Either H has the form $r^{-\zeta_2/2} h(\Delta T / r^{\zeta_2/2})$, where h is a function to be determined, or else H is a linear function of ΔT of the form $f(r)\Delta T(r)$. The former case yields regular scaling and the latter case leads to a fully-determined expression for $J_{2n}(r)$,

$$J_{2n}(r) = 2n S_{2n}^{\mathrm{T}}(r) A(r) / S_2^{\mathrm{T}}(r), \tag{11}$$

where $A(r) = \nabla^2 S_2^{\mathrm{T}}(r) - \nabla^2 S_2^{\mathrm{T}}(0)$, and anomalous scaling of a precise form:

$$\zeta_{2n} = \tfrac{1}{2} \sqrt{4nd\zeta_2 + (d - \zeta_2)^2} - \tfrac{1}{2}(d - \zeta_2), \tag{12}$$

where $\eta(r) \propto r^{\zeta(\eta)}$, $S_{2n}^{\mathrm{T}}(r) \propto r^{\zeta_{2n}}$ in the inertial range and $\zeta_2 = 2 - \zeta(\eta)$. As $n \to \infty$, $\zeta_{2n} \propto n^{1/2}$.

An independent argument involving realizability inequalities on the dissipation field $\nabla^2 T$ appears to rule out regular scaling [3], so that, if the analysis is valid, (12) remains as the only possible power-law scaling in the inertial range. This result was obtained under the special assumption of very rapidly changing velocity field, but some features may be of broad applicability. Plausible arguments can be made that the dependence of the ζ_{2n} on $\zeta(\eta)$ is unchanged if the velocity field has finite correlation times but remains Gaussian. Corrections to the ζ_{2n} are expected if the velocity field displays intermittent (anomalous) scaling.

It was noted earlier that some scaling properties of Burgers turbulence are correctly given by a statistical approximation (LHDIA) that is incapable of describing the shocks associated with the scaling. If (12) is correct, something analogous may be going on in the passive scalar case. The high-order anomalous exponents certainly are strongly affected by spatial structures in which the scalar gradient is exceptionally large. Such structures are not captured by statistical description in terms of the $S_{2n}^{\mathrm{T}}(r)$ alone, and the scalar-field analysis sketched above certainly takes no account of specific spatial structures. The hope raised is that it may be unnecessary to do so if only scaling exponents are sought.

The Burgers scaling discussed earlier can be obtained from a framework like that erected for the passive scalar by adding heuristic elements associated with LHDIA. The advection term in the equation of motion for $S_{2n}^{\mathbf{u}}(r)$ cannot be written exactly as for a passive scalar with rapidly changing velocity field. However, a very similar form is obtained by doing renormalized perturbation approximation based on LHDIA. The result is an equation like (6), but with an important difference: a factor of $2n$ appears in the advection term on the left side because, in contrast to the scalar case where there is only one $\mathbf{u}$ factor, any of the $2n$ factors u in $\left\langle u^{2n}\partial u/\partial x\right\rangle$ may be regarded as the advecting velocity.

For inertial range r, $\eta(r) \propto r$ in Burgers dynamics, where $S_2^{\mathbf{u}}(r) \propto r$. One way to see this is to note that the cascade rate $\eta(r)r^{-2}S_2^{\mathbf{u}}(r)$ mediated by eddy viscosity is then independent of r. The similar fact for NS under K41 assumptions is that $\eta(r)r^{-2}S_2^{\mathbf{u}}(r)$ is independent of r with $\eta(r) \propto r^{4/3}$, $S_2^{\mathbf{u}}(r) \propto r^{2/3}$. In both cases, ∇^2 is expressed by r^{-2}. With $\eta(r) \propto r$, the analog of (6) gives the correct Burgers scaling $S_{2n}^{\mathbf{u}}(r) \propto r$ by balance of advective and dissipative terms, if the dissipative term is taken in the form corresponding to (11). It is easy to see independently that this form is exact in the shock-dominated Burgers inertial range, where dissipation is confined to the shocks.

It is unclear to what extent similar procedures are meaningful in three-dimensional NS dynamics, where intense vortex tubes and sheets are expected to make major contributions to high-order structure functions in place of the shocks of Burgers dynamics. One can write a balance equation like (6) in steady state and argue as in [3] that, if both sides scale as as powers of r, then anomalous scaling is possible only if the conditional mean corresponding to (9) is linear so that the dissipation term has a form like (11).

To go further, some estimate must be made of the advective term. Here the vector character of $\mathbf{u}$, incompressibility, and pressure all make things more complicated than in the Burgers case. An LHDIA-like perturbative evaluation can be carried out, as in the Burgers case, but this has not yet been done. Plausibly, the Burgers and rapid-velocity-field passive scalar cases represent limits for three-dimensional NS scaling. Burgers presents the most rapid possible growth of intermittency with decrease of scale size; there is no disruption of coherence by eddy effects. The passive scalar, on the other hand, appears to give the best possible opportunity for relaxation of intermittency by eddy transport effects.

The stretching of vorticity in an incompressible three-dimensional NS field would seem much more analogous to stretching of scalar blobs than to the formation of shocks under Burgers equation. If so, the $n^{1/2}$ behavior for the scaling exponents of a scalar field given by (12) may be a meaningful zeroth approximation to the exponents of the NS velocity field. At the present time this is only

speculation. However, Nelkin has shown that models incorporating such behavior can be consistent with experimental data on NS structure functions [8]. He points out that the $n^{1/2}$ dependence can be related to a class of fractal processes recently described by Novikov [9].

In general, the determination of higher scaling exponents has proved very resistant to analytical treatment. The shock-mediated intermittency of Burgers and the scalar advected by a rapidly-changing velocity field are particularly friendly cases. It may be of general significance that the deduction of scaling exponents for the passive scalar reviewed above involves conditional means in an essential way. Most analytical work on turbulence has been related more or less closely to renormalized perturbation analysis. Systematic approximations for moments can be constructed fairly straightforwardly by such analysis, but this is very much not the case for conditional means. The present analysis suggests, therefore, that nonperturbative methods should be sought if higher statistics are the goal.

AKNOWLEDGEMENT

This work was supported by the U. S. Department of Energy under Grant DE-FG03-90ER14118.

REFERENCES

[1] "Turbulence and Stochastic Processes", ed. by J. C. R. Hunt, O. M. Phillips, and D. Williams, Proc. Roy. Soc. London A **434**, 1-240 (1991). This commemorative collection of articles gives a comprehensive picture of work on inertial-range scaling during the fifty years starting with Kolmogorov's 1941 papers on turbulence.

[2] R. H. Kraichnan, Phys. Rev. Lett. **72**, 1016 (1994).

[3] R. H. Kraichnan, V. Yakhot, and S. Chen, submitted to Phys. Rev. Lett. (1995).

[4] R. H. Kraichnan, J. Fluid Mech. **62**, 305 (1974)

[5] R. H. Kraichnan, Phys. Fluids **11**, 266 (1968).

[6] R. H. Kraichnan, Phys. Fluids **11**, 945 (1968).

[7] B. I. Shraiman and E. D. Siggia, Phys. Rev. E **49**, 2912 (1994).

[8] M. Nelkin, submitted to Phys. Rev. E (1995).

[9] E. A. Novikov, Phys. Rev. E **50**, R3303 (1994).

CONVECTION IN A NEMATIC LIQUID CRYSTAL WITH HOMEOTROPIC ALIGNMENT AND HEATED FROM BELOW

Guenter Ahlers

Department of Physics and
Center for Nonlinear Studies
University of California
Santa Barbara, CA 93106

ABSTRACT

Experimental results for convection in a thin horizontal layer of a homeotropically aligned nematic liquid crystal heated from below and in a vertical magnetic field are presented. A subcritical Hopf bifurcation leads to the convecting state. There is quantitative agreement between the measured and the predicted bifurcation line as a function of magnetic field. The nonlinear state near the bifurcation is one of spatio-temporal chaos which seems to be the result of a zig-zag instability of the straight-roll state.

INTRODUCTION

Convection in an *isotropic* fluid heated from below is well known as Rayleigh-Bénard convection (RBC).[1,2] However, this phenomenon is altered dramatically in the case of a nematic liquid crystal (NLC). Here we discuss what happens when the NLC has homeotropic alignment (*i.e.*, has a director which is aligned in the vertical direction parallel to the heat flux) and is heated from below.[3,4,5] The usual Rayleigh-Bénard destabilization due to a thermally-induced density gradient is opposed by the stiffness of the director field which is coupled to and distorted by any flow. It turns out that relaxation times of the director field are much longer than thermal relaxation times. For that reason it is possible for director fluctuations and temperature/velocity fluctuations to be out of phase as they grow in amplitude. This situation typically leads to an oscillatory instability (also known as overstability), and the bifurcation at which these time-periodic perturbations acquire a positive growth rate is known as a Hopf bifurcation.[6] This case is closely analogous to convection in binary-fluid mixtures with a negative separation ratio.[7,8] In that case, concentration gradients oppose convection, and concentration diffusion has the slow and heat diffusion the fast time scale. It turns out that the Hopf bifurcation in the NLC case is subcritical,[5] and that the fully developed nonlinear state no longer is time periodic. Instead, the statistically stationary state above the bifurcation is one of spatio-temporal chaos with a typical time scale which is about two orders of magnitude slower than the inverse Hopf frequency.[9]

However, it was possible to actually measure the Hopf frequency by looking at the growth or decay of small perturbations which were deliberately introduced when the system was close to the conduction state and near the bifurcation point.[5]

A convenient aspect of thermal convection in NLCs is that an external magnetic field will couple to the fluid because the diamagnetic susceptibility is anisotropic. A field of modest strength can have a dramatic effect on the phenomena which are observed. This adds greatly to the richness of the physics accessible to the experimentalist. In the case of homeotropic alignment to be discussed, the field is parallel to the heat current.

An interesting aspect of NLC convection is that we are dealing with a system whose equations of motion are well known,[10;11] but significantly more complicated than the Navier-Stokes equations for isotropic fluids. The usual viscosity η and conductivity λ are replaced by six viscosities $\alpha_i, i = 1, \ldots, 6$ and two conductivities $\lambda_{\|}$ and $\lambda_{\perp}$, and the equations for momentum and energy balance must be coupled to an equation for the director field which contains three elastic constants $k_{ii}, i = 1, 2, 3$. In spite of these complexities, it has been possible to carry out quantitative stability analyses, and under some conditions predictions in the weakly nonlinear regime have been made.[12,13,14] Thus, one may argue that comparison of quantitative experiments on thermal convection in NLC's with corresponding detailed theoretical calculations provides an excellent testing ground for the applicability of methods of stability analysis and of weakly nonlinear theory to systems which are more complex than isotropic fluids.

From another point of view, thermal convection in NLCs provides a rich system for the study of general problems in pattern formation. During the last two decades interest in this nonlinear topic has seen a revival in the physics community, and a great deal has been learned from experiments about nonlinear pattern-forming dissipative systems.[15,16] The case under consideration here leads to a spatio-temporally complex pattern often referred to as spatio-temporal chaos (STC).

The most common NLC for the study of Rayleigh-Bénard convection has been p-methoxy benzylidene-p-n-butylaniline (MBBA). The reason for this apparently is historical; MBBA was the first material for which all relevant physical properties, which are necessary for comparison between experiment and theory, had been measured. However, a recent survey of the literature revealed that the properties of some of the cyano-biphenyls are known nearly as well. These materials are far more stable and less toxic than MBBA, and thus have advantages for precise experimental work. They are also relatively inexpensive, and this is an important factor for thermal convection because comparatively large amounts (typically perhaps 30 cm^3) are required.[17] In the present work we have used 4–n–pentyl–4′–cyanobiphenyl (5CB).

THEORETICAL PREDICTIONS

As for Rayleigh-Bénard convection in an isotropic fluid, the conduction state has rotational symmetry in the horizontal plane because its director is oriented vertically and parallel to the magnetic field and the heat flow. Thus, patterns of arbitrary angular orientation should form unless the boundary conditions of the experiment select a particular direction.

The first instability should be a Hopf bifurcation, that is the disturbances which first acquire a positive growth rate should be time-periodic.[3,4] As the magnetic field is increased, the threshold for convection is predicted to shift to larger values.[5,13] This was confirmed by

early experimental work on this system.[5] For sufficiently high fields the primary bifurcation is predicted to be to a stationary state of convection.[13] There is a codimension-two point where the two bifurcation lines meet. The situation is somewhat similar to binary-mixture convection,[15] which has been studied extensively in recent years.

The quantitative aspects of the instabilities are determined by four dimensionless parameters which are formed from combinations of the fluid properties.[18] They are[12] the Prandtl number

$$\sigma = \frac{(\alpha_4/2)}{\rho\kappa_\parallel} \quad , \tag{1}$$

the ratio between the director relaxation time and the heat diffusion time

$$F = \frac{(\alpha_2/2)\kappa_\parallel}{k_{33}} \quad , \tag{2}$$

the Rayleigh number

$$R = \frac{\alpha g \rho d^3 \Delta T}{(\alpha_4/2)\kappa_\parallel} \quad , \tag{3}$$

and the dimensionless magnetic field

$$h = H/H_{F,\parallel} \tag{4}$$

with the Fréedericksz field

$$H_{F,\parallel} = \frac{\pi}{d}\sqrt{\frac{k_{33}}{\rho\chi a}} \quad . \tag{5}$$

The time scale of transients and pattern dynamics is measured in terms of

$$t_v = d^2/\kappa_\parallel \quad . \tag{6}$$

As usual, $\kappa_\parallel$ is the thermal diffusivity $\lambda_\parallel/\rho C_p$. Both h and R are easily varied in an experiment, and may be regarded as two independent control parameters. The availability of h in addition to R makes it possible to explore an entire line of instabilities. The parameters F, σ, and t_v are essentially fixed once a particular NLC and temperature range have been chosen, and even between different NLCs there is not a great range at our disposal. For 5CB at 26° we have $\sigma = 272$ and $F = 460$. The critical value R_c of R and the fluid parameters determine the critical temperature difference ΔT_c for a sample of a given thickness d. The realistic experimental requirement that $\Delta T_c \simeq$ a few °C dictates that the sample thickness should be a few mm. Typical values of $H_{F,\parallel}$ are near 20 *Gauss*. Thus modest fields of a *kGauss* or so are adequate to explore the entire range of interest.

A linear stability analysis was carried out by several investigators.[4,19,20,21] A very detailed analysis of this case was presented recently by Feng, Decker, Pesch, and Kramer (FDPK).[13] These authors also provided a weakly nonlinear analysis, and we shall briefly describe their results.

For low fields, FDPK predict that the first instability will be a subcritical Hopf bifurcation. The critical Rayleigh number $R_c(H)$ varies typically from about 1500 at small fields to about 3400 for $h \simeq 50$. The details of $R_c(H)$ depend upon σ and F, and have

to be computed for each particular case. The wavevector which first becomes unstable is predicted to vary from about 3.2 to 4.6 as the field increases from $h = 0$ to $h \simeq 50$. The Hopf frequency is expected to be between about 12 and 2 over this range. It would not be too helpful to be more specific here since the details of all these parameters depend upon σ and F. At $h = h^{ct} \simeq 50$ (assuming typical parameter values for MBBA), the Hopf bifurcation line meets a stationary bifurcation at a codimension-two point. At this point, the Hopf frequency is predicted to be finite (close to 2) and there is a discontinuity of about 10% in the wavevector. The stationary bifurcation for $h > h^{ct}$ initially is also predicted to be subcritical, but for $h \gtrsim 63$ (for typical MBBA parameters) it is expected to become supercritical. At $h = h^{ct} \simeq 63$, the coefficient of the cubic term in a Ginzburg-Landau equation vanishes and a tricritical point is predicted for the stationary bifurcation branch.

EXPERIMENTAL RESULTS

Early measurements for this system were made by Guyon, Pieranski, and Salan[5] (GPS). These authors used the NLC MBBA. Their sample had a thickness $d = 5\ mm$, yielding $H_{F,\|} \simeq 15\ Gauss$. It had a circular cross section, and a diameter of 54 mm.[22] At half-height, several thermocouples were mounted in the fluid to monitor the local temperature. A heater wire near the thermocouples also traversed the sample. It is difficult to say whether these intrusive devices had an influence on the hydrodynamics. The temperature stability of the water baths above and below the sample was of the order of 0.01°C. GPS measured the onset of convection by monitoring the response of their thermocouples to a temperature perturbation induced by a heat pulse delivered by the heater wire. If this response grew (decayed) as a function of time, the threshold of their system had (had not) been exceeded. They were also able to determine a characteristic frequency from the thermocouple response during the transients which led to the convecting nonlinear state. The results for ΔT_c are qualitatively consistent with the theoretical results[13] for the laterally infinite system. The magnitude of ΔT_c at a given field was within 10 or 20 % of the theoretical value. ΔT_c increased with H up to $H \simeq 580\ Gauss (h \simeq 33)$, and then decreased again. The maximum was interpreted[13] as the predicted codimension-two point which for the laterally infinite system is expected at $h^{ct} = 51$, although it occurred at a rather low field. The measurements also provided clear evidence for hysteresis at the primary bifurcation. The measured Hopf frequency had a maximum near $h = 13$, whereas the theory predicts the maximum to occur near $h = 32$. The frequency was generally of the same size as the one given by the theory, but at the highest field values $h \simeq 33$ it was still much larger than expected for $h = h^{ct}$. We conclude that these experiments clearly established a number of central features of the bifurcation. These include its subcritical nature and the time-periodic behavior of the growing perturbations of the conduction state. However, at the quantitative level there are substantial differences between the experiments and the theory for the laterally infinite system.

We used a circular cell with $d = 3.94\ mm$ and $r = 41.9\ mm$, corresponding to a radial aspect ratio $\Gamma \equiv r/d = 10.6$. The fluid was 5CB. For this system, $t_v = 136\ s$ and $H_{F,\|} = 21.1\ Gauss$. Monodomain homeotropic samples were prepared before each experimental "run". The heat current was increased in small steps while the top temperature was held fixed at 19°C, until convection occurred. The heat current then was decreased again in small steps until convection ceased. At each heat-current value, the bottom-plate temperature was measured at one-minute intervals for two hours ($\simeq 53 t_v$). The temperature measurements and the heat current were used to determine the Nusselt number, which

is given by

$$N \equiv \lambda_{eff}/\lambda_{\|} \quad . \tag{7}$$

Here $\lambda_{\|}$ is the conductivity of the homeotropically aligned sample, and

$$\lambda_{eff} \equiv -Qd/\Delta T \tag{8}$$

is the effective conductivity and contains contributions from diffusive conduction and from hydrodynamic flow. While the current was steady, images of the convection pattern were acquired by the computer-interfaced CCD camera.

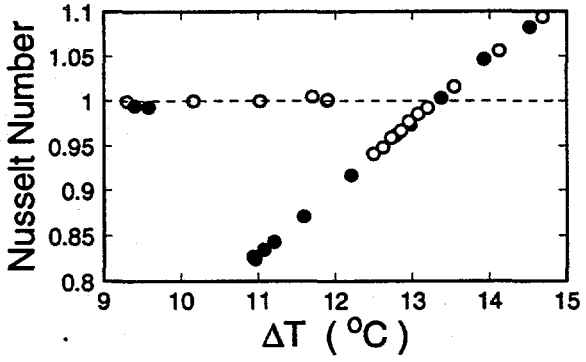

Figure 1. Nusselt number measurements for $h = 9.4$ ($H = 200$ *Gauss*). Open (filled) circles were obtained with increasing (decreasing) steps in ΔT.

Figure 1 shows N as a function of ΔT for $H = 200$ *Gauss* ($h \simeq 9.4$). Surprisingly, N decreased below one when convection started. This can be understood because the conductivity of a sample with parallel alignment, in which $\mathbf{Q}$ is perpendicular to $\hat{n}$ ($\lambda_{\perp}$), is much less than the conductivity of the homeotropic case ($\lambda_{\|}$).[23] The direct hydrodynamic contribution to the heat flux is smaller than the decrease in the heat flux due to the deviations of the director from parallel alignment caused by the flow. As the current decreased, the conduction state was reached at a value of ΔT equal to $\Delta T_s < \Delta T_c$, showing the predicted and previously observed[5] hysteresis. For small fields ($H < 250G$), the conduction state reached from the convecting state had a conductivity less than $\lambda_{\|}$, corresponding to $N < 1$, because the hydrodynamic flow experienced by the sample had introduced defects which reduced the average conductivity below $\lambda_{\|}$. At the field value of this experiment, the elimination of defects from the sample occurred on a time scale which was much longer than the duration of the experiment. The visual appearance of the conduction state reached after convection is interesting. It had the appearance of curdled milk, with the clusters of non-homeotropic alignment corresponding to the curds suspended in a nearly-clear background fluid of homeotropic alignment.

From data like those in Fig. 1, values of the critical temperature difference ΔT_c and of the temperature difference at the saddle node ΔT_s were determined with an uncertainty of about 0.5 %. The corresponding Rayleigh numbers are shown in Fig. 2 as a function of h^2 (solid circles: ΔT_c, open circles: ΔT_s). The solid line in the figure is the theoretical prediction,[13] evaluated for the properties of 5CB at the mean temperature of the experiment. As can be seen, the agreement with the measurements is excellent. The small deviations at large h are probably caused by excessive variations of the fluid properties over the temperature interval of the measurement when the temperature of the cell bottom is

rather close to T_{NI}. There are as yet no predictions for R_s. It is interesting that R_s is only about 10% below R_c. Nonetheless, a calculation may turn out to be difficult because there is already severe distortion of the originally homeotropic director field by the fluid flow, as evidenced by the defects encountered after the conduction state is reached once more.

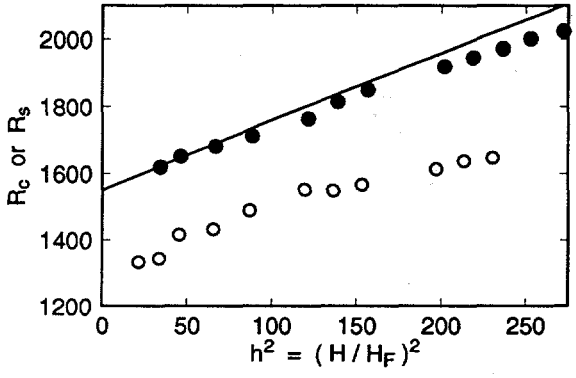

Figure 2. Solid circles: Critical Rayleigh numbers for the onset of convection as a function of h^2. Open circles: Rayleigh numbers at the saddle node where convection ceased when the heat current was lowered.

The pattern which evolves beyond the bifurcation is extremely interesting. The first two rows of Fig. 3 show typical images of the flow field immediately above the convective threshold for $h = 9.4$. By examining relatively rapid time sequences of images, it was found that, on the time scale of the inverse of the expected Hopf frequency, the convection rolls were steady rather than travelling or standing waves. This is not in contradiction to the predicted Hopf bifurcation because the subcritical nature of the bifurcation leads to a finite-amplitude state at threshold whereas the theory pertains to an infinitesimal perturbation of the conduction state. A similar situation is encountered in binary-mixture convection, where for a range of values of the separation ratio the convection rolls are steady when $\Delta T = \Delta T_c$ even though small perturbations of the conduction state are travelling waves. In our experiment, there unfortunately was no way to determine the frequency of small-amplitude transients as had been done by GPS.

On a much longer time scale, the pattern evolved continuously. This is illustrated by the images in Fig. 3, which are from a single experimental run with constant external conditions. They were taken at the times indicated in each image, in units of $t_v = 136\ s$, which had elapsed since an arbitrary origin at which the pattern already had been equilibrated for some time. Even in runs of much longer duration (up to two weeks or $9000t_v$) no steady state was reached. The nature of the pattern did not change noticeably over the field range $5 < h < 16$ covered by the experiments, although no quantitative studies as a function of h have been carried out. It appears that the patterns are disordered both in space and in time, providing an example of spatio-temporal chaos.

The bottom row of Fig. 3 gives the modulus of the Fourier transform. The transforms were base on the central parts of the images, by using the filter function $W(r) = cos^2[(\pi/2)(r/r_0)]$ for $r < r_0$ and $W(r) = 0$ for $r > r_0$. Here r_0 was set equal to 85% of the sample radius. The transforms for $t = 449$ and 1033 show that the nature of the pattern changed dramatically with time. The rightmost image in the bottom row of Fig. 3 (labeled "Avg") shows the square root of the time average of the square of the modulus of the Fourier transform [*i.e.* of the structure factor $S(k)$]. The average involved 250 images taken over a total time period of $1123t_v$ (nearly two days). It is seen to contain

contributions at all angles, consistent with the idea of a statistically stationary process of non-periodic pattern evolution and with the expected rotational symmetry of the system.

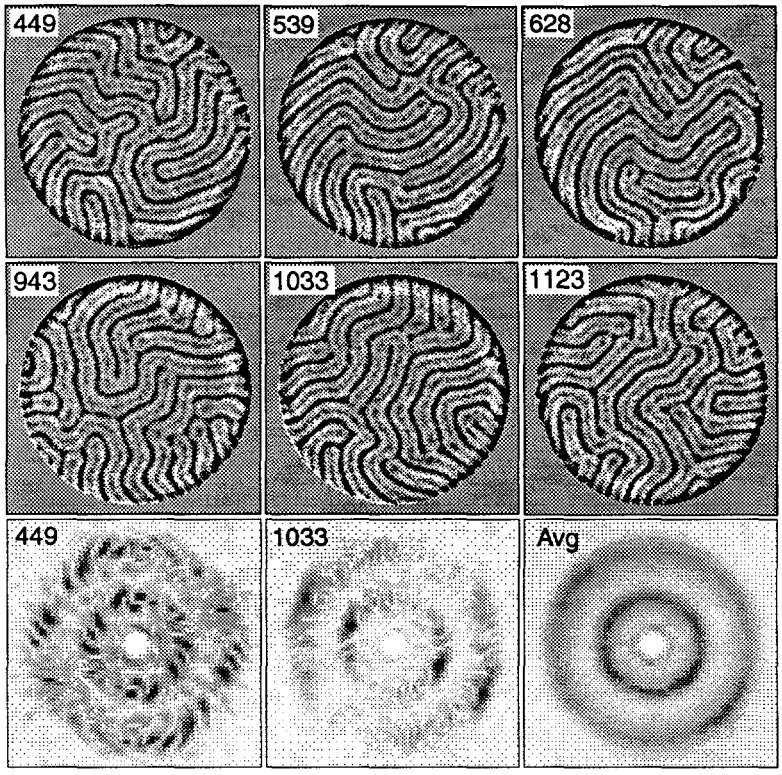

Figure 3. Top two rows: a sequence of images from the same run at 200 *Gauss* ($h = 9.4$), taken with constant external conditions. The time elapsed since the start of the run (in units of $t_v = 136\ s$) is given in the top left corner of each image. Bottom row: Square root of the structure factor of the central portions of two of the images shown above, and the average of the structure factor of the central portions of 250 images spanning a time interval of $1123 t_v$.

Figure 4a shows the azimuthal average $S(k)$ of the temporal average of the structure factor for the run described above, *i.e.* of the lower right image in Fig. 3. Both the fundamental and the second harmonic (corresponding to a roll width of half a wavelength) are well developed, but the higher harmonics are so weak as to be unobservable on the scale of the figure. The characteristic wavenumber of the pattern is about 3.4. This is fairly close to the theoretically predicted wavenumber for the mode which first acquires a positive growth rate; but since the observed state is one of finite amplitude, this agreement is not particularly significant. Figure 4b shows the average over k of $S(\mathbf{k})$ as a function of the azimuthal angle Θ [the average over k was computed only in the vicinity of the fundamental peak of $S(k)$]. Although there is a discernable maximum near $\Theta \approx 0.75$, the angular distribution is really quite uniform. Any remaining structure might well disappear if data were averaged over longer time periods. On the other hand, it could also be indicative of a slight asymmetry in the experimental cell.

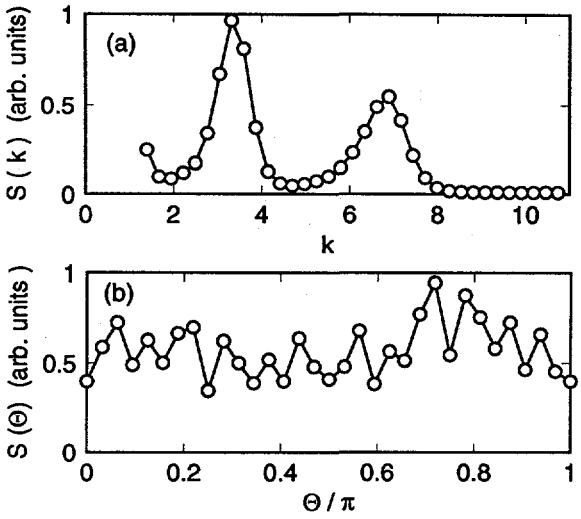

Figure 4. a): The azimuthally averaged structure factor $S(k)$ as a function of the modulus k of the wavevector. b): the radially averaged structure factor $S(\Theta)$ as a function of the azimuthal angle Θ.

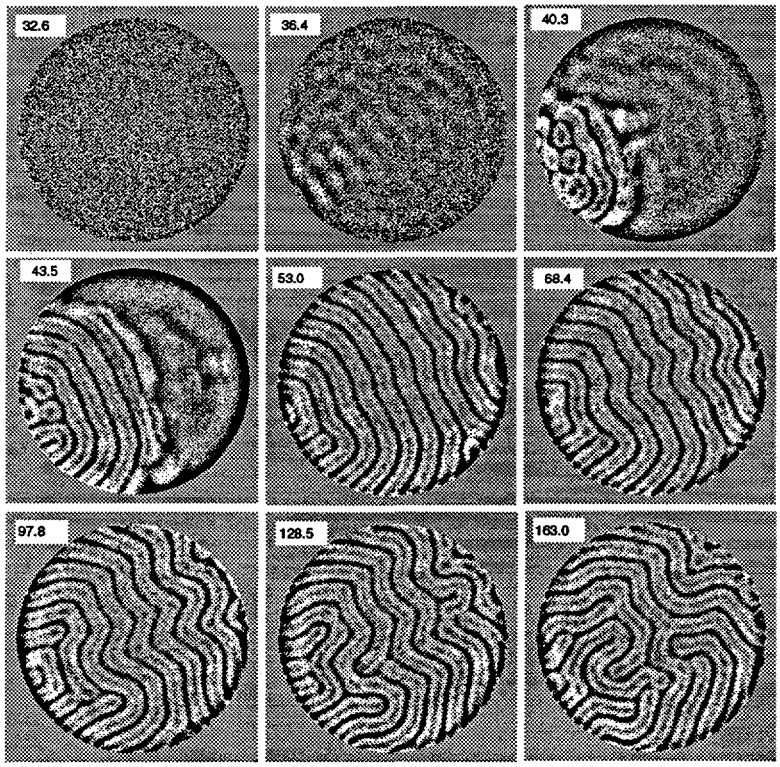

Figure 5. A temporal succession of images during the transient leading from conduction to convection when ΔT was raised slightly above ΔT_c. The field was $h = 9.4$. The numbers are the elapsed time, in units of t_v, since the threshold was exceeded.

It is instructive to examine the transients which lead from the conduction to the convecting state. This is done in Fig. 5. Here the number in each image gives the time, in units of t_v, which has elapsed since ΔT was raised slightly (1%) above ΔT_c. At $t = 32.6$,

there is still no evidence of convection; but at $t = 36.4$, there are noticeable fluctuations in the image which correspond to hydrodynamic flow. At $t = 40.3$, some of these fluctuations have grown to macroscopic amplitudes, and a front of convection is invading the quiescent fluid (t = 43.5). This creates a state of nearly-straight parallel convection rolls ($t = 53$). However, these straight rolls turn out to be unstable to a zig-zag instability. The zig-zag disturbance can be seen to grow at $t = 68.4$ and 97.4. In the end, this instability leads to the spatially and temporally disordered pattern shown for $t = 163$ and in Fig. 3.3. Thus, we see that a secondary instability led to a chaotic state rather than to a new time-independent pattern. This phenomenon most likely is analogous to the one encountered in very early experiments on spatio-temporal chaos using liquid helium[24,25], where ordinary RB convection became chaotically time dependent, probably because the skewed-varicose instability[26] was crossed (one cannot be absolutely sure about this because in the early work there was no flow visualization).

REFERENCES

1. H. BÉNARD, *Rev. Gen. Sci. Pure Appl.* **11**, 1261, 1309 (1900); and *Ann. Chim. Phys.* **23**, 62 (1901).
2. A large literature pertaining to this field has evolved. Particularly useful as introductions to early work are the reviews by E.L. KOSCHMIEDER, *Adv. Chem. Phys.* **26**, 177 (1974); and in *Order and Fluctuations in Equilibrium and Nonequilibrium Statistical Mechanics,* XVIIth International Solvay Conference, ed. by G. Nicolis, G. Dewel, and J.W. Turner (Wiley, NY, 1981), p. 168; and by F. BUSSE, in *Hydrodynamic Instabilities and the Transition to Turbulence,* edited by H.L. Swinney and J.P. Gollub (Springer, Berlin, 1981), p. 97; and in *Rep. Prog. Phys.* **41**, 1929 (1978).
3. H. LEKKERKERKER, *J. Phys. France Lett.* **38**, 277 (1977).
4. H. LEKKERKERKER, *J. Phys. Colloq. France* **40**, C3 (1979).
5. E. GUYON, P. PIERANSKI, and J. SALAN, *J. Fluid. Mech.* **93** 65, (1979).
6. For a summary of bifurcation types, see for instance Appendix A of P. BERGÉ, Y. POMEAU, and C. VIDAL, *Order within Chaos* (Wiley, NY, 1986).
7. D.T.J. HURLE and E. JAKEMAN, *J. Fluid Mech.* **47**, 667 (1971).
8. For a recent review, see for instance, M. C. CROSS and P.C. HOHENBERG, *Rev. Mod. Phys.* **65**, 851 (1993).
9. G. AHLERS, unpublished.
10. P.G. DE GENNES, *The Physics of Liquid Crystals* (Clarendon Press, Oxford, 1973).
11. M.J. STEPHEN and J.P. STRALEY, *Rev. Mod. Phys.* **46**, 617 (1974).
12. Q. FENG, W. PESCH, and L. KRAMER, *Phys. Rev. A* **45**, 7242 (1992).
13. Q. FENG, W. DECKER, W. PESCH, and L. KRAMER, *J. Phys. France* **II 2**, 1303 (1992).
14. L. KRAMER and W. PESCH, *Annu. Rev. Fluid Mech.* **27**, in print.

15. M.C. CROSS and P.C. HOHENBERG, *Rev. Mod. Phys.* **65**, 851 (1993).

16. G. AHLERS, in Proceedings of the XIIIth Sitges Conference, edited by M. Rubio (Springer), in print.

17. We obtained our 5CB from EM Industries, 5 Skyline Drive, Hawthorne, NY 10532.

18. For a discussion of the properties of 5CB, see G. AHLERS, in *Pattern Formation in Liquid Crystals*, edited by L. Kramer and A. Buka (Springer, 1995).

19. M. VELARDE and I. ZÚÑIGA, *J. Phys. France* **40**, 725 (1979).

20. P. BARRATT and D. SLOAN, *J. Fluid Mech.* **102**, 389 (1981).

21. P. BARRATT and J. MANLEY, *J. Non-Equilib. Thermodyn.* **8**, 143 (1983).

22. J. SALAN, private communication.

23. G. AHLERS, D.S. CANNELL, L.I. BERGE, and S. SAKURAI, *Phys. Rev. E* **49**, 545 (1994).

24. G. AHLERS, in *Fluctuations, Instabilities, and Phase Transitions*, edited by T. Riste (Plenum, NY, 1974), p. 181.

25. G. AHLERS, *Phys. Rev. Lett.* **33**, 1185 (1974).

26. F.H. BUSSE and R.M. CLEVER, *J. Fluid Mech.* **91**, 319 (1979).

MODELING OF MIXING PROCESSES: FLUIDS, PARTICULATES, AND POWDERS

J. M. Ottino and S. Hansen

Laboratory for Fluid Mechanics, Chaos and Mixing
Department of Chemical Engineering, Northwestern University
Evanston, Illinois 60208

ABSTRACT

Work under this grant involves two main areas: (i) *Mixing of Viscous Liquids,* this first area comprising aggregation, fragmentation and dispersion, and (ii) *Mixing of Powders.* In order to produce a coherent self-contained picture, we report primarily on results obtained under (i), and within this area, mostly on computational studies of particle aggregation in regular and chaotic flows.

Numerical simulations show that the average cluster size of compact clusters grows algebraically, while the average cluster size of fractal clusters grows exponentially; companion mathematical arguments are used to describe the initial growth of average cluster size and polydispersity. It is found that when the system is well mixed and the capture radius independent of mass, the polydispersity is constant for long-times and the cluster size distribution is self-similar. Furthermore, our simulations indicate that the fractal nature of the clusters is dependent upon the mixing.

INTRODUCTION

The overall objective of our work under this grant is to produce fundamental knowledge of viscous mixing processes involving multiphase fluids and particulate systems. Our goal is to generate broad-based understanding relevant to a variety of industrial applications. The motivation for such an approach is the belief that there is a broad common denominator underlying many of the mixing problems shared by industry.

Current problems of interest in mixing can be found in polymer processing, chemical reaction engineering and composites, food processing/consumer products, and the pharmaceutical industry. Work in these areas is being carried out by both industry and universities. However, mixing-related research in all these disciplines has developed in nearly independent fashion. Often one sees "practical" work that

is hard to generalize and "basic" results that are hard to apply. We believe that there is a need to generate a more fundamental understanding of mixing since, at a fundamental level, there are strong similarities in the basic science underlying all these applications.

As a step towards reaching the above goals we concentrate on two main areas: (i) *Mixing of Viscous Liquids*, this area involving work in aggregation, fragmentation and dispersion, and (ii) *Mixing of Powders*. Work carried out under (ii), initially perceived as an extension of on our work in suspensions, is rapidly becoming a distinct area involving a rather different approach, and future extensions may be carried out outside the bounds of this grant.

MIXING OF VISCOUS LIQUIDS: AGGREGATION, FRAGMENTATION AND DISPERSION

DISPERSION

The basic goal of work in this area is to obtain basic understanding of mixing of immiscible fluids leading to the determination of flow conditions which result in efficient breakup and dispersion of one mass of fluid in the bulk of another. Related issues are the prediction of the morphological structures and drop size distribution in complex flows. This area is relatively well developed. We are currently investigating dispersion and coalescence processes in non-homogeneous flows.

AGGREGATION AND FRAGMENTATION

Work in this area focuses on fundamental issues in flow-driven particle aggregation and fragmentation and dispersion of agglomerates in complex flows. An understanding of aggregation, the reverse of breakup, complements and enhances our studies of breakup of immiscible fluids.

On-going research investigates flow-driven aggregation in nonhomogeneous flows. We study, by dynamic modeling, aggregation of compact and fractal structures in model flows typifying regular and chaotic regimes. Emphasis is placed on two-dimensional flows but three-dimensional systems are considered as well. The goal is to put into evidence flow effects - kinetics of aggregation, cluster size distribution and structure of aggregates - with the long range goal of manipulating flows to tailor the structure of clusters.

Two aggregation scenarios are considered: in (i) the clusters retain a compact geometry - forming disks and spheres - whereas in (ii) fractal structures are formed. The primary focus of (i) is *kinetics and self-similarity* of size distributions, while the main focus of (ii) is the *fractal structure* of the clusters and its dependence with the flow.

Classically, irreversible aggregation is described by Smoluchowski's coagulation equation which can be written for a continuous distribution of cluster sizes as

$$\frac{\partial n(x,t)}{\partial t} = \frac{1}{2}\int_0^x K(x-y,y)n(x-y,t)n(y,t)dy - n(x,t)\int_0^\infty K(x,y)n(y,t)dy, \quad (1)$$

where n(x,t) is the concentration of clusters of mass x at time t and K(x,y) is the rate of aggregation of clusters of masses x and y. The first term, on the right-hand side, accounts for the formation of a cluster of size x due to aggregation of two clusters of size x-y and y, whereas the second term represents the loss of clusters of mass x. Typically, the analysis of aggregation can be simplified by use of the scaling ansatz [1]

$$n(x,t) = [s(t)]^{-2}\Phi\left(\frac{x}{s(t)}\right), \quad (2)$$

which reduces the number of variables from two (x and t) to one (x/s(t)). The function Φ is commonly referred to as the scaling distribution.

The scaling ansatz allows predictions of the long-time behavior of Smoluchowski's equation. However, the scaling does not address the initial evolution of the cluster size distribution. We have shown however, that it is possible to develop analytical estimates of this growth.

The primary goal of our work however, is to assess the effects of flow. A preliminary study [2], which does not explicitly address the fractal nature of the clusters, shows that islands of regularity may cause spatial variations in the rate of aggregation, and that aggregation in "well-mixed" chaotic systems is similar mathematically to Brownian aggregation and can be described by Smoluchowski's equation. The effect of chaotic mixing on the fractal nature of clusters is considered explicitly by Danielson, Muzzio and Ottino [3]. They determined the fractal dimension of the cluster is affected by mixing [for background on mixing and chaos, see 4]. This differs from a study by Torres et al. [5] which predicts that the flow field does not affect the fractal nature of the resulting clusters. The variation of fractal dimension with mixing is due to the nature of interactions of monomers and larger clusters in different mixing schemes. If the system is not well mixed, the large clusters do not interact with each other, the process resembles the particle-cluster aggregation [5]. However, if the system is well mixed, then larger clusters interact with each other and aggregation resembles cluster-cluster [5] aggregation. Thus, the fractal dimension of a cluster is expected to decrease with better mixing.

Computational studies were carried out in the so-called journal bearing flow. A particularly important aspect of this flow is that it can be realized experimentally and manipulated to produce both regular and chaotic flows [6]. Also, analytic streamfunctions, which allow for tractable computations, can be found in Wannier [7].

Our simulations mimic fast coagulation; particles seeded in the flow are convected passively and aggregate upon contact. Brownian motion is not considered and hydrodynamic interactions are neglected; passive particles move as fluid elements. The flows considered are regular, chaotic, and a combination of both. The clusters are compact (or spherical) and fractal (a typical fractal structure from our simulations can be seen below).

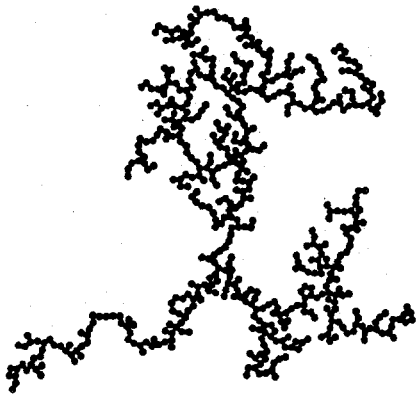

Figure 1: Typical fractal cluster from our simulations. The fractal dimension of this cluster is 1.54±0.001, and the radius of gyration is 40 times the particle radius.

An outline of the results obtained to date is shown in the following table:

	Growth of Average Cluster Size, s(t)				
Flow	Compact Structure				Fractal Structure
	constant capture radius, α		total area or volume constant		
	2 dimensions	3 dimensions	2 dimensions	3 dimensions	
Regular	for α=0.0025 $(1+0.22t)^{0.77}$ R=0.999	for α=0.0067 $(1+0.21t)^{0.7}$ R=0.997	for ρ=0.1 $(1+0.0065t)^{14}$ R=0.997	for ϕ=0.1 $(1+2.7t)^{0.85}$ R=0.998	for ρ=0.1 $(1+0.22t)^{0.7}$ R=0.999
"Poorly" mixed	for α=0.0025 $(1+0.29t)^{0.62}$ R=0.999 for α=0.00067 $(1+0.025t)^{0.55}$ R=0.999	for α=0.0067 $(1+0.44t)^{0.55}$ R=0.998	for ρ=0.02 $(1+0.018t)^{0.81}$ R=0.999 for ρ=0.1 $(1+0.0098t)^{25}$ R=0.988	for ϕ=0.1 $(1+25t)^{0.66}$ R=0.997	for ρ=0.02 exp(0.085t) R=0.999 for ρ=0.1 exp(0.79t) R=0.999
Chaotic	for α=0.0025 $(1+0.22t)^{1}$ R=0.995	for α=0.0067 $(1+0.21t)^{0.93}$ R=0.997	for ρ=0.02 $(1+0.012t)^{5.2}$ R=0.999 for ρ=0.1 $(1+0.06t)^{6.5}$ R=0.999	for ϕ=0.1 $(1+7.5t)^{1}$ R=0.998	for ρ=0.02 exp(0.21t) R=0.986 for ρ=0.1 exp(1.38t) R=0.976

Table 1: the growth rate of the average cluster size in the various studies. Here, α, ρ and ϕ are the capture radius, area fraction and volume fraction of clusters, respectively.

In general, the average cluster size and variance of the size distribution grow faster for fractal structures than compact structures, and the variance of the size distribution grows faster in poorly-mixed systems. Let us now consider a breakdown of the results: When the capture radius is constant, the average cluster size grows as $s(t) = s_0(1+t/t)^z$. The cluster size distributions are self-similar for the well mixed case and are given by

$$n(x,t) \approx M_1 s(t)^{-2} e^{-x/s(t)}. \tag{3}$$

However, the scaling ansatz does not hold for the poorly-mixed system. These results suggest that the size distribution may to some degree be controlled by the mixing. When the clusters are area conserving, formation of a large cluster dominates aggregation.

Significantly different kinetics are observed if fractal structure is considered; the average cluster size grows exponentially, as opposed to algebraically as in the case of compact structures.

Furthermore, due to the wide range of flow in the journal bearing flow, a distribution of fractal clusters is produced. When the area fraction of clusters is 0.02, the median fractal dimension of the clusters is dependent on the flow, similar to the study by Danielson et al. [3]. The median fractal dimension of clusters formed in the well-mixed system is 1.47 while the median fractal dimension of clusters formed in the poorly-mixed case is 1.55. Furthermore, the range of fractal dimension is higher in the well-mixed case.

The results are different when the area fraction of clusters increases. The median fractal dimension of the clusters is independent of the flow and is approximately 1.47. Since the fractal dimension of the clusters is closer to the dimension of the clusters in the well mixed system with a lower area fraction of clusters, this suggests that as the area fraction of clusters increases, the island of regularity gets broken up by the increasing capture radius of the clusters. Thus, aggregation in the poorly-mixed system behaves similarly to that in the well mixed system when aggregation occurs between the two disjoint regions of the flow. A more complete summary of these results appear in a paper under preparation [8].

MIXING OF SOLIDS

Let us consider now a few results pertaining to mixing of solids (dry powders). Our current understanding of solids mixing can scarcely be described as more than primitive: we can neither qualitatively nor quantitatively analyze the effectiveness of any given mixing mechanism in advance; we do not have a widely accepted set of equations - as in the companion case of liquid mixing - that govern solids mixing, and we cannot even establish whether a given set of solids will mix or de-mix under a given stirring regimen.

Recent work [9] has demonstrated that significant inroads can be made in this area using rather modest resources. We have shown that slow mixing processes can be imagined as a succession of avalanches and that processes can be divided into geometrical and dynamical parts. The geometrical aspects of the problems can be

cast in the language of maps. In depth aspects of dynamical aspects - leading for example to segregation effects - can be incorporated by means of molecular dynamic simulations. Simpler ad hoc methods capture gross aspects as well. Below we show a comparison between a experiment (left) and a computer simulation (right).

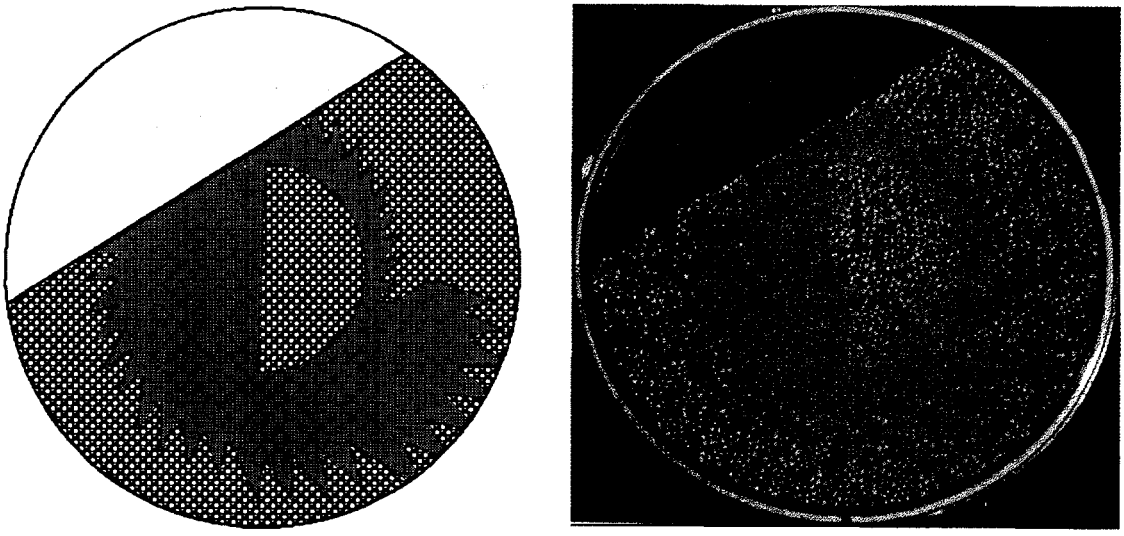

ACKNOWLEDGMENT

This work was supported by the U.S. Department of Energy, Division of Basic Energy Sciences.

REFERENCES

1. Meakin P., "Aggregation kinetics," *Physica Scripta* **46**, 295-331 (1992).

2. Muzzio, F. J. and Ottino, J. M., "Coagulation in chaotic flows," *Phys. Rev. A* **38**, 2516-2524 (1988).

3. Danielson, T. J., Muzzio, F. J. and Ottino, J. M., "Aggregation and structure formation in chaotic and regular flows," *Phys. Rev. Lett.* **66**, 3128-3131 (1991).

4. Ottino, J. M., *The kinematics of mixing: stretching, chaos, and transport*, Cambridge University Press: Cambridge, reprinted (1990).

5. Torres, F. E., Russel, W. B. and Schowalter, W. R., "Simulations of coagulation in viscous flows," *J. Colloid Interface Sci.* **145**, 51-73 (1991).

6. Swanson, P. D., and Ottino, J. M., "A comparative computational and experimental study of chaotic mixing of viscous fluids," *J. Fluid Mech.* **213**, 227-249 (1990).

7. Wannier, G. H., "A contribution to the hydrodynamics of lubrication," *Q. Appl. Maths.*, **8**, 1-32 (1950).

8. Hansen, S. and Ottino, J. M., "Aggregation and cluster size evolution in non-homogeneous flows," submitted to *J. Colloid Interface Sci.* (1995).

9. Metcalfe, G., Shinbrot, T., McCarthy, J. J., and Ottino, J. M., "Avalanche mixing of granular solids," *Nature* **374**, 38-41 (1995).